AN ABSTRACT OF THE DISSERTATION OF

Lauren E. Crandon for the degree of Doctor of Philosophy in Environmental Engineering presented on June 11, 2018.

Title: Addressing Persistent Challenges in Nanotoxicology exposures: Techniques for *in situ* Characterization

Abstract approved: _____

Stacey L. Harper

Nanoparticles (NPs), defined by their size (1-100 nm), are increasingly incorporated into commercial and industrial products due to their high surface area and unique properties. They can be designed for specific applications by manipulating composition, size, shape, and surface functionalization. As NP production and complexity increases, there is a need to rapidly assess relevant parameters to prioritize hazard testing and ultimately predict behavior upon release into the environment. Robust and reproducible characterization of toxicity and physicochemical properties of NPs in solution are needed for reliable model development. In this dissertation, I address significant challenges regarding NP dispersion consistency and characterization of NP properties.

Current practices of NP dispersion preparation that utilize sonication to break apart agglomerates were evaluated for consistently across nanotoxicology studies, and it was determined that they vary greatly in the type of ultrasonicator used, total energy input, and reporting of associated metadata. To facilitate comparison across studies, I demonstrate a method to deliver equivalent energy to NP dispersions using three different ultrasonicator systems with various power settings and dispersion media. This can improve uniformity of NP exposures for

better reproducibility of toxicity and characterization data.

The hydrophobicity of NPs, a key property determining environmental fate and bioavailability, was evaluated with two potential methods optimized for use with NPs, hydrophobic interaction chromatography (HIC) and dye adsorption, and compared results to those obtained using the octanol water partitioning method commonly used for organic and dissolved chemicals. Measures of hydrophobicity were determined for both agglomerated and surface functionalized NPs.

Finally I address the need for a quantitative measure of redox behavior of NPs to inform the design of catalytic nanomaterials as well as to model potential toxic interactions. The use of methylene blue (MB) as a colorimetric probe to quantify the catalytic redox behavior of NPs is proposed in Chapter 4. The redox assay was compared to modified abiotic methods to evaluate reactive oxygen species (ROS) production (dichlorofluorescein diacetate, DCFH-DA) and antioxidant capacity (Trolox Equivalent Antioxidant Capacity, TEAC) of NPs to determine relationships and trends based on methodology used and NP properties.

The studies presented in this dissertation provides the basis for improved reproducibility of NP exposures for toxicity data and addresses clear data gaps for determining fate and toxicity descriptors of NPs. This work will contribute to comprehensive NP characterization that is ultimately needed for predictive fate and toxicity models for sustainable nanotechnology development.

# Addressing Persistent Challenges in Nanotoxicology Exposures: Techniques for *in situ* Characterization

by
Lauren E. Crandon

A DISSERTATION

submitted to

Oregon State University

in partial fulfillment of
the requirements for the
degree of

Doctor of Philosophy

Presented June 11, 2018
Commencement June 2019

Doctor of Philosophy dissertation of Lauren E. Crandon presented on June 11, 2018

APPROVED:

---

Major Professor, representing Environmental Engineering

---

Head of the School of Chemical, Biological, and Environmental Engineering

---

Dean of the Graduate School

I understand that my dissertation will become part of the permanent collection of Oregon State University libraries. My signature below authorizes release of my dissertation to any reader upon request.

---

Lauren E. Crandon, Author

# ACKNOWLEDGEMENTS

I am sincerely grateful for Dr. Stacey Harper for her guidance, encouragement, and faith in me. Her mentorship over the last few years has made me a better scientist and person. I would also like to thank Bryan Harper, who was instrumental in experimental design and analysis, and whose feedback and encouragement made this dissertation possible. Thank you so much to my committee members Dr. Jeffrey Nason, Dr. Tyler Radniecki, Dr. Liney Arnadottir and Dr. Ingrid Arocho for your advice and support. A special thanks to Dr. Skip Rochefort who has been a wonderful mentor to me over the past few years. I am so thankful for my fellow Harper Lab group graduate students, Fan Wu and Lindsay Denluck, who have been incredible mentors and friends. I especially want to thank Matt Mueller for his unwavering love and support during this journey.

## CONTRIBUTION OF AUTHORS

The research presented in this dissertation is a product of the work of many researchers and could not have been completed without their help. In Chapter 2, Vince N. Cataldi and Sabrina R. Luker assisted with data collection and analysis. In Chapter 3, Macklin Turnquist assisted with method development and data collection and Padmaja Chavan collected and analyzed isotherm data for CuO. In Chapter 4 Kala M. Kopecek assisted with method development, data collection and analysis, and made intellectual contributions to the manuscript. Zheng Zhou collected all data and interpreted results for the Antioxidant Capacity assay in Chapter 4. Stacey L. Harper and Bryan J. Harper provided technical, analytical, and editorial support for all research in this dissertation.

TABLE OF CONTENTS

TABLE OF CONTENTS (Continued)

TABLE OF CONTENTS (Continued)

LIST OF FIGURES

LIST OF FIGURES (Continued)

LIST OF TABLES

# Addressing Persistent Challenges in Nanotoxicology Exposures: Techniques for *in situ* Characterization

## 1 Introduction

Nanotechnology, defined as the use of matter at the nanoscale (1-100 nm), has become a platform for innovative technology spanning fields of medicine, chemistry, engineering, and manufacturing [23]. The small size of nanoparticles (NPs) results in a large surface area to volume ratio and a high proportion of atoms at the surface, which leads to higher reactivity and rates of dissolution [122, 172]. Some materials in the nano size range exhibit unique physical and chemical properties that differ from "bulk" sized or dissolved forms, such as altered optical properties and increased tensile strength [52, 54].

The unique properties of NPs have been utilized for a diversity of applications, and are increasingly used in commercial and industrials products. Examples include cosmetics, heterogeneous catalysts, antimicrobials, pigments, and nanomedicine [190]. The implementation of nanotechnology also has promising environmental benefits, including environmental remediation and promoting efficient use of resources, since less material is required to produce a given surface area [149]. The application of nano-enabled technology has rapidly grown and is expected to continue to increase. Global consumption of nanomaterials is expected to approximately double by 2021 [20]. Among the most widely used and produced NPs are metal and metal oxides, especially $TiO_2$, $SiO_2$, ZnO, Ag, and $CeO_2$ [209, 216]. The increased production of engineered NPs is accompanied by increased environmental exposure. NPs are released into air, waters, soils,

and sediments as they move through their life cycle [72].

The rapid development of nanotechnology is outpacing our understanding of the environmental implications associated with increased exposure. Risk assessment is complicated by the fact that unlike chemicals, which are defined by molecular structure, nanomaterials involve core composition, surface coating, size and shape [78]. Nanomaterials can theoretically be composed of any material, including composites and alloys, be functionalized with surface coatings, and have a variety of morphology and sizes, resulting in a seemingly unlimited number of unique materials. Adding to the complexity, when NPs enter the environment, they undergo transformations due to changes in ionic strength, pH, temperature, and presence of organic matter, including biomolecules that effectively alter the NP surface and available surface area [119]. This enormous testing matrix has led researchers to move toward *in silico* approaches for risk assessment and responsible development of nanomaterials [197].

A number of statistical frameworks have been proposed to relate structural and compositional properties of nanomaterials to toxic effects [63, 122, 137]. For example, Puzyn *et al.* modeled the toxicity of metal oxide NPs to *Escherichia coli* using enthalpy of formation of a gaseous metal cation [164]. Zhang *et al.* demonstrated that the cytotoxicity of metal oxide NPs strongly correlated with band gap energies in the range of cellular redox processes (-4.12 to -4.84 eV) [225]. However, a more recent study found that dissolution and not band gap energy correlated with *in vivo* toxicity of ZnO and $Mn_2O$ NPs to oyster embryos [144]. Despite these studies and others which demonstrate descriptive correlations between select NP properties and toxicity, there is not yet sufficient data to develop more powerful predictive models.

Before models can be widely implemented, reliable and reproducible toxicity data and robust physicochemical characterization of nanomaterials are

needed. The toxicity of various NPs have been demonstrated using a number of *in vitro* and *in vivo* testing models [68, 183, 184]. However, the results of nanotoxicology studies are difficult to reproduce and studies often report contradictory data [103]. Recent attention has been given to the role of NP dispersion techniques and agglomeration on the inconsistencies among studies [173, 185]. Guidelines have been proposed to harmonize NP dispersion preparation [70, 146] and reporting of agglomeration size and stability [103, 120]. However, it is unclear how widespread the recommended guidelines are among studies and how significantly they affect NP exposure and toxicity results.

To address the physicochemical characterization of nanomaterials, the Organization for Economic Cooperation and Development (OECD) formed the Working Party of Manufactured Nanomaterials (WPMN) in 2006 to systematically evaluate testing guidelines [167, 166]. A series of interlaboratory studies were performed using Au, Ag, $TiO_2$, $SiO_2$, $CeO_2$, ZnO, fullerenes ($C_{60}$), single and multi-wall carbon nanotubes, nanoclays and dendrimers to validate guidelines for measuring properties of nanomaterials in solution such as agglomeration, zeta potential, porosity, hydrophobicity, photocatalytic activity and redox potential [148]. Many characterization protocols that are commonly applied to evaluate chemicals were deemed unsuitable for NPs. Among the properties evaluated, protocols for evaluating hydrophobicity and redox potential were determined to be meaningless when applied to insoluble particulate nanomaterials and no exceptions or alternative methods were provided [167]. One promising approach is the use of rapid functional assays, which characterize NPs in relevant exposure conditions to encompass complex interactions at the NP surface [71]. The results obtained using functional assays are therefore system dependent and must be accompanied by complete reporting of system properties and conditions. A functional assay based approach is used in the studies presented

here to rapidly collect robust and reproducible data. Standard media (i.e. PBS buffer) are used as a reference and future studies can be performed in more complex media to quantify surface transformations.

This dissertation addresses key challenges identified in characterizing physicochemical properties of nanomaterials. Chapter 2 reviews current practices in nanomaterial dispersion preparation among nanotoxicology studies and focuses in particular on methods of sonication used to break apart agglomerates in suspension. Approaches to calibrate different types of ultrasonication systems and power inputs are presented to facilitate more uniform NP exposure across studies, allowing for reproducible data regardless of the equipment being utilized in any given laboratory. Chapter 3 presents a comparative analysis of potential methods to evaluate the hydrophobicity of NPs, which is a key parameter that determines transport, distribution, and bioavailability. Chapter 4 proposes a colorimetric assay to determine the relative redox potential of NPs, and compares it with methods to determine reactive oxygen species generation and antioxidant capacity. The three assays described in Chapter 4 are applied to a series of lanthanide oxide NPs, and periodic trends are analyzed to determine intrinsic properties of lanthanide oxides that correlate with redox. Methods presented in this dissertation are developed with the aim of widespread implementation, across classes of nanomaterials and research groups. Each chapter considers factors such as cost, accessibility of instrumentation, and interpretation of results.

# 2 Calibration of energy input during the preparation of aqueous nanoparticle dispersions

Lauren E. Crandon, Vince N. Cataldi, Sabrina R. Luker, Bryan J. Harper, & Stacey L. Harper

## 2.1 Abstract

The size of nanoparticle (NP) agglomerates significantly affects the dose to organisms and observed effects when evaluating the fate and toxicity of NPs. Stable NP dispersions are made by using ultrasonic waves to break apart large agglomerates, and several standard sonication protocols have been proposed to improve data reproducibility and dispersion consistency. A review of 56 recent nanotoxicology studies revealed that sonication practices vary greatly in the type of ultrasonicator used, total energy input, and reporting of associated metadata. To facilitate comparison across studies, we demonstrate a method to deliver equivalent energy to NP dispersions using three different ultrasonicator systems: probe, cup horn, and bath. Calorimetric calibration was performed to determine the energy delivered by each system, which took into account effects of energy dissipation through media and the geometry of each type of sonicator. The power input was varied while maintaining an equivalent energy input of 8400 J. Our sonication protocol was applied to $CeO_2$ and $TiO_2$ NPs of similar primary particle size dispersed in ultrapure water, 0.1 mM KCl, and simulated fresh water. The hydrodynamic diameter (HDD) was measured using dynamic light scattering to assess agglomeration. We found that when energy was held constant, HDD was not significantly different between ultrasonication systems or power inputs for a given material and dispersion medium. To determine the effects of energy input, we varied the delivered sonication energy (840-84000 J) for NP dispersions in ultrapure water. The HDD of $CeO_2$ NPs decreased with increasing energy, but $TiO_2$ NPs did not have energy dependent agglomeration behavior, demonstrating that optimal energy input for stable NP dispersions is material specific. Our work here provides a standardized method to deliver equivalent sonication energy, even when employing different ultrasonication systems and power settings. We recommend that future studies implement these

calibration methods and routinely report sonication energy, dispersion medium, NP composition details, and HDD to better contextualize NP exposure for comparative and regulatory purposes.

## 2.2 Introduction

Studies which evaluate the aquatic fate and toxicity of NPs are often difficult to reproduce and this may be due, in part, to lack of standardized methods for preparing NP dispersions [200]. To evaluate the behavior and toxicity of nanoparticles (NPs) in biological systems, NPs are first dispersed in relevant media. Once placed in liquid, nanomaterials often form large agglomerates due to attractive van der Waals forces, which can affect environmental interactions and cause NPs to rapidly settle [47, 132]. Many studies utilize ultrasonication (commonly referred to as "sonication"), which applies acoustic energy (>20kHz) to break apart large agglomerates and form suspensions of particles in the nanometer size range [200]. For many NPs without a surface stabilizer, no amount of sonication energy can completely break apart agglomerates and form dispersions of primary particles [126, 227]. The goal of sonication is therefore to minimize NP agglomerate size and form relatively stable and monodisperse suspensions [37, 46].

The manner in which suspensions are sonicated greatly affects the agglomeration state and resulting NP surface area, and can potentially alter the surface chemistry of NPs [42, 159]. An interlaboratory study which compared the size and surface charge of prepared gold, polystyrene, silica, and ceria NPs pointed to ultrasonication practices as a major culprit for variability in dispersion stability, particularly for dispersions prepared from dry nanopowder [173]. The effects of sonication have also been shown to result in differences in toxicity. Kang *et al.*

and Sager *et al.* compared the uptake and toxicity of NPs with and without sonication and found that well dispersed exposures resulted in higher rates of lung deposition and toxicity in mammals [87, 177]. A recent meta-analysis of *Daphnia magna* nanotoxicity experiments found that inconsistencies among studies were primarily explained by differences in dispersion techniques, including sonication methods [185].

Reproducible methods of sonication are particularly important for surface reactive materials and NPs that dissolve and release toxic metal ions. During sonication, the formation and collapse of cavitation bubbles produces local areas of extremely high temperature and pressure (approximately 5000 K and 50000 kPa), which can lead to the formation of reactive oxygen species (ROS) [55, 131, 194]. ROS can alter the NP surface by oxidation, and has been shown to modify or degrade commonly used organic surface coatings [91, 200]. The same effect could potentially lead to the disintegration of carbon based nanomaterials, such as fullerenes or carbon nanotubes [21]. The interaction of ROS with media components may also have implications for toxicity. Sonication with a common surfactant was found to cause the production of toxic degradation byproducts, and cell viability decreased with increasing sonication time [218].

Energy input during sonication can enhance the dissolution rate of soluble species. Sonication has been shown to increase the rate of ion release from Cu and Mn NPs, which can potentially increase the observed toxicity [42, 130, 159]. A comparison of different sonication methods revealed a direct effect on the acute toxicity of Ag and CuO NPs to *Daphnia magna*, and this was found to be the result of increased dissolution associated with longer sonication times [84]. The ability of sonication to alter not only the agglomeration state of NPs, but also NP surface and dispersion medium highlights the need for uniform sonication practices for dispersion, particularly for toxicity evaluation.

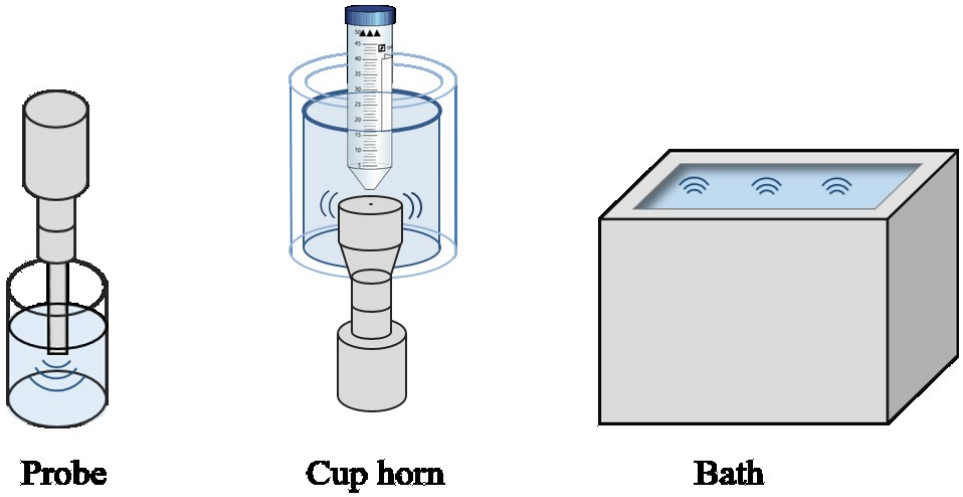


FIGURE 2.1: Schematic of a probe ultrasonicator (direct), cup horn ultrasonicator (indirect), and bath ultrasonicator (indirect).

### 2.2.1 Ultrasonication systems

Ultrasonication systems function to disperse nanoparticle suspensions by propagating acoustic waves through the medium which results in high energy cavitation that acts to break apart agglomerates. Several types of sonication systems are available for NP dispersion preparation and are classified by manner of energy delivery as either direct or indirect methods (Fig. 2.1). Direct ultrasonication involves immersing a probe directly into the suspension, which allows for high intensity energy delivery. This method, also defined as probe sonication, is generally recommended for the disruption of agglomerated NP dispersions [70, 82, 146, 163, 199]. Indirect methods include cup horn and bath ultrasonication, where energy must travel through water (or some other liquid) to the sample. A cup horn sonicator is considered a high intensity ultrasonic bath and is typically used for cell disruption, protein extraction, and releasing DNA and RNA from cells. The high energy delivered during sonication can lead to a temperature increase of the sample, and to minimize this, probe and cup horn sonicators can be operated in pulse mode as opposed to continuous soni-

cation. In addition, probe sonication is often performed in an ice bath and cup horn sonicators are commonly operated in a thermostat configuration designed to maintain a constant bath temperature. A bath sonicator delivers lower power and does not circulate water, but can accommodate larger sample volumes than a cup horn. Indirect methods are not recommended in standard protocols for dispersing NPs, but are often chosen to avoid sample contamination by the probe or to avoid the release of titanium from the probe surface into NP suspensions [22, 62].

### 2.2.2 Amplitude

For the probe and cup horn configurations, the programmed amplitude, often reflected as percent (%) of the maximum, refers to the displacement of the probe tip as it vibrates. For example, the maximum amplitude for a 13 mm probe using a 750 W Sonics system (Fig. 2.1) is 114 $\mu$m, and the % amplitude is the fraction of that length traveled. This energy at the tip of the probe is dissipated through the liquid and causes alternating high and low pressure waves. A higher amplitude is accompanied by greater power and higher intensity of cavitation [168]. During sonication, the programmed amplitude is held constant and the power is varied in response to resistance to movement of the probe, which can be affected by the viscosity of the medium, temperature, and NP concentration.

### 2.2.3 Standard protocols

Several protocols have been published to standardize the preparation of NP dispersions [70, 82, 146, 163, 201]. Recently, the Organization for Economic Cooperation and Development (OECD) updated guidelines which are consistent with most other protocols and is among the most detailed [147]. In brief, this guideline recommends preparing a NP stock concentration of 0.5 to $5.0 \times 10^{12}$ particles/L in ultrapure water at a final volume of 125 mL. Concentrations

based on particle count are difficult to determine when preparing stocks from nanopowder, and a volume of 125 mL may cause excessive NP waste when only smaller quantities are needed for experimentation. The standard recommended sonication system is a probe sonicator and protocols call for sonicating at a power of 40 W for 10 minutes. Although probe sonicators are known to deliver the highest intensity, submerging the probe directly in suspensions can cause contamination and leaching of titanium from the probe surface. Additionally, specific reporting requirements are outlined, which include detailing information about the volume of sample and solvent, sonication time or energy input, and characteristics of the dispersion media such as pH, ionic strength, and organic matter content [146].

### 2.2.4 Calibration of sonicators

To account for differences in sonication systems, standard protocols require calibrating the probe sonicator at all power settings to determine delivered energy. The sonication energy reported in studies often refers to the electrical output from the instrument; however, this energy is transformed to mechanical energy and does not accurately represent the acoustic energy actually delivered to the sample [96]. Efficiency depends on the specific instrument, the characteristics of the NP dispersion (medium, volume, and particle concentration), temperature, and time. Calibration provides a measurement of how much energy is absorbed by the system and can account for aging of the piezoelectric crystals inside the converter which, over time, can affect the amplitude of vibrations and therefore the power delivered. Calorimetry and chemical dosimetry, including the Frick reaction and KI oxidation have been used to calibrate individual sonication systems [96, 97]. Although chemical methodologies can be useful, calorimetry is the most widely used because it is simple, requires few materials, and is not sensitive to the initial temperature of the NP suspension. Utilizing

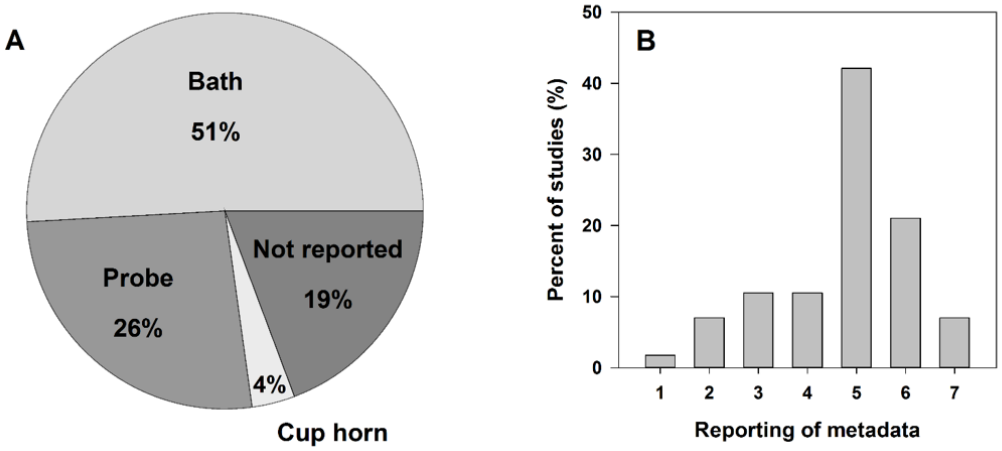


FIGURE 2.2: A) Types of sonicators used B) histogram of studies rated by quality and completeness of reported metadata based on a review of 56 nanotoxicology studies.

the calorimetric approach, the delivered power is determined by measuring the change in temperature of the medium during sonication with the assumption that mechanical energy is converted to heat.

### 2.2.5 Review of sonication practices in nanotoxicology

Despite standardized sonication guidelines, methods used in practice vary greatly among published nanotoxicology studies. We performed a literature review of 56 recent nanotoxicology studies (2007-2018) which sonicated NP stocks prior to exposure (Table A1). Most studies (51%) reported using an ultrasonic bath, but others used a probe, cup horn sonicator, or did not report the type of sonicator used (Fig. 2.2A). As we previously described, the type of sonicator greatly impacts the intensity and power delivered to the sample.

The sonication energies reported ranged across orders of magnitude (approximately $5 \times 10^{-1} - 2 \times 10^{3}$ J) for those studies that either explicitly reported energy or provided sufficient information about power and time. More than half of studies did not report energy. Energy should be reported in context of the

sample volume, because volume can affect the disruption effect for a given energy input. Portions of the sample in closer proximity to the probe/horn are likely to experience a greater disruptive effect, so sonicating large volumes provides a lower energy density; whereas, in smaller volumes the entire sample might be in close contact with the probe. The majority of studies (79%) fail to report sample volume used during sonication. The size of the probe also affects the intensity of energy delivered, and although many studies specify the sonication instrument used, only four of the studies surveyed here explicitly reported the probe diameter.

The concentration of NP stocks were generally reported on a mass basis and varied among studies across many orders of magnitude, ranging from 10 $\mu$g/mL to $40 \times 10^3 \mu$g/mL (Table A1). NP concentration affects the rate of particle collisions during sonication, which can act to either break apart agglomerates or in some cases induce further agglomeration [199]. Although existing protocols specify a narrow range of NP concentrations for sonication in an effort to limit variability in particle collisions across studies, these are provided as number concentrations. Most studies continue to report NP concentrations on a mass basis, and this may be due to limited availability of instrumentation required to measure accurate particle counts at the nanoscale across a range of particle concentrations. This could make compliance with standard protocols difficult, and may be responsible for the large discrepancies in concentrations used.

The dispersion medium was generally reported to be ultrapure water, a buffer solution, or exposure medium, such as cell culture or simulated natural waters (Table A1). Ions in dispersion media are known to directly affect suspension stability and particle agglomeration by compressing the electric double layer and increasing agglomeration. Organic matter can coat the NP surface and provide a stabilizing affect that prevents agglomeration [227]. Components of the

medium can also influence agglomeration behavior by affecting how sonication energy is delivered. Changes in viscosity can alter the resistance to movement of the probe and affect the power input. Ionic strength and density can affect how the medium dissipates the delivered energy [200]. For environmentally relevant media, the impact is likely to be small; however, media properties can act to augment the potential effect of sonication energy on NP surface reactivity. Proteins in biological media, for example, have been shown to promote dissolution of metal and metal oxide NPs during sonication [42, 159].

We ranked the reviewed studies based on quality and completeness of the reported metadata described above (Fig. 2.2B). Studies which reported all relevant details that would be required for replication (sonicator type, energy, time, NP composition, volume, medium, concentration) were given a rating of "7." For every missing piece of information, one point was subtracted. Studies who received a "1" rating typically only reported the NP material and stated that sonication was performed. Metadata should be sufficiently detailed to establish meaningful trends among studies, and such numerical frameworks have been proposed to improve data quality for nanomaterial regulation [128].

In this study, our objective was to update standard NP dispersion protocols to allow for reproducible data regardless of the equipment being utilized in any given laboratory, and to highlight the discrepancies in current practices reported in the literature. We hypothesize that agglomerate size is dependent on the total energy input by the ultrasonicator, regardless of what sonicator type or power setting is used. We aimed to produce similar $CeO_2$ and $TiO_2$ NP dispersions using three different sonicator systems: probe, cup horn, and bath. $CeO_2$ and $TiO_2$ were selected due to their widespread use, limited dissolution, and known propensity to agglomerate in suspension. We applied our calibration procedure across different programmed amplitudes and validated this method

in three relevant dispersion media.

## 2.3 Methods

### 2.3.1 Sonicator calibration

Calorimetric calibration was performed for a probe and cup horn ultrasonicator (Vibra Cell 750, 20 kHz, Sonics & Materials, Inc., Newtown, CT) and an ultrasonic bath (Fisher Scientific, 1.9 L, 70 W, 40 kHz). A thermocouple was used to measure the temperature of water as a function of time for programmed amplitudes of 20%, 30%, and 40% on the probe and cup horn sonicators. 40% was selected because it is the highest allowable amplitude for the cup horn configuration. The ultrasonic bath does not have an option to program different powers, so calibration was only performed at one power. The sonicators were insulated for calibration to better support the assumption that all mechanical energy was converted to thermal energy. The delivered acoustic power was calibrated by performing a linear regression of temperature as a function of time and solving for power Eq. 2.1:

$$P = mC_p\frac{dT}{dt} \tag{2.1}$$

where $P$ is the delivered acoustic power (W), $C_p$ is the specific heat of water (4.2 J/g°C) and $m$ is the mass of water (g). The delivered power was used to calculate sonication time for a given energy Eq.2.2

$$t = \frac{E}{P} \tag{2.2}$$

TABLE 2.1: Sonication reported power, calibrated power and estimated times to deliver 8400 J total energy to dispersions.

| **Programmed Amplitude** | **Instrument Reported Power (W)** | **Calibrated Power (W)** | **Sonication Time (s)** |
|---|---|---|---|
| **Probe** | | | |
| 20% | 33.8 | 10.0 | 35 |
| 30% | 48.8 | 15.4 | 23 |
| 40% | 78.8 | 19.6 | 18 |
| **Cup horn** | | | |
| 20% | 27.5 | 22.2 | 379 |
| 30% | 52.0 | 27.9 | 301 |
| 40% | 77.3 | 40.1 | 209 |
| **Bath** | | | |
| | 70.0 | 15.0 | 564 |

where $t$ is sonication time (s), $E$ is energy (J), and $P$ is delivered acoustic power (W). The energy was held constant at 8400 J and the time was varied to evaluate the impacts of different delivered power.

### 2.3.2 Nanoparticle stock preparation

$CeO_2$ and $TiO_2$ (anatase) were purchased from Sigma Aldrich (St. Louis, MO) and had a similar average primary particle size of 25 nm. Stock suspensions (1000 mg/L) were prepared by dispersing dry nanopowder in ultrapure water (Milli-Q 18.2 Ω resistivity), 0.1 mM KCl, or simulated fresh water (FW) comprised of 15 mM NaCl, 0.5 mM KCl, 1 mM $CaCl_2$:2 $H_2O$, 0.15 mM $KH_2PO_4$, 0.05 mM $Na_2HPO_4$ and 1 mM $MgSO_4$:7 $H_2O$ and adjusted to a pH of 7.0 [221]. Suspensions were vortexed, then diluted to a concentration of 50 mg/L in a volume of 10 mL, except for the probe sonication group which was prepared in a volume of 40 mL to accommodate the probe tip.

### 2.3.3 Sonication

Sonication was performed with a 750 W, 20 kHz Vibra-Cell ultrasonic processor (Sonics & Materials, Inc., Newtown, CT) equipped with a 13 mm diameter probe (probe sonication) and a 51 mm diameter probe equipped with a cup horn attachment with continuously flowing cooling water (cup horn). The programmed amplitude was set for 20%, 30%, and 40% for the probe and cup horn sonicators and the time needed to achieve equivalent energy was determined by calibration (Table 2.1). The ultrasonic bath (1.9 L, 70 W, 40 kHz, Fisher Scientific, Pittsburgh, PA) does not allow the user to adjust the amplitude and was used at the single power setting. Samples prepared using the cup horn and ultrasonic bath configuration were 10 mL NP stock in a 15 mL plastic conical tube. Samples prepared with the probe sonicator were 40 mL NP stock in a 50 mL tube to accommodate volume displacement by the probe and avoid contact of the probe with the wall of the tube. To prevent a significant increase in temperature for all sonicator types, the probe samples were placed in an ice bath, cooling water was continuously circulated through the cup horn, and the water in the ultrasonic bath was refreshed before each trial. For all powers and sonicators, the energy was held constant at 8400 J by altering the times (Table 2.1). For dispersions in ultrapure water, the energy was further varied from 840-84000 J to evaluate the effect of total energy on agglomeration.

### 2.3.4 Dynamic Light Scattering

Hydrodynamic diameter (HDD) was measured using dynamic light scattering (DLS) using a Malvern Zetasizer Nano ZS (Malvern Instruments, Westborough, MA) immediately following sonication. Sonicated dispersions (1.5 mL) were placed in a disposable cuvette prior to measurement. The temperature was held constant at 25°C. Control dispersions were prepared in all three media in

which samples were vortexed but not sonicated prior to measurement. The z-average was used as a measure of agglomerate size.

### 2.3.5 Statistics

SigmaPlot version 13.0 (Systat Software, San Jose, CA, USA) was used to perform all statistical analyses. All experiments were performed in triplicate. Differences among sonication type and power inputs for each NP and each dispersion media were compared using analysis of variance (ANOVA) with Holm-Sidak post-hoc analysis. Differences were considered statistically significant when $p \leq 0.05$. Error bars represent standard error of the mean. Linear regression was performed for sonication calibration curves to determine the increase in temperature per unit time. The decrease in HDD as a function of sonication energy was fit to a first order exponential decay.

## 2.4 Results

### 2.4.1 Calibration of sonicators

Delivered acoustic power was calibrated for the ultrasonic bath and for the probe and cup horn ultrasonicators at different programmed amplitudes (20-40%) (Fig. 2.3). A linear relationship between temperature and time was observed for all systems ($R^2 \geq 0.94$). The calibration curve for the probe sonicator had a steeper slope than the indirect systems at all amplitudes and temperatures reached 70°C within five minutes.

The total energy delivered was held constant at 8400 J, which can be achieved by all three systems in less than 10 minutes. The ultrasonic bath delivered an average power of 15.0 W. The power delivered by the cup horn sonicator was calibrated to be 22.2, 27.9, and 40.2 W for programmed amplitudes of 20%, 30%, and 40%, respectively. The power delivered to the probe sonicator

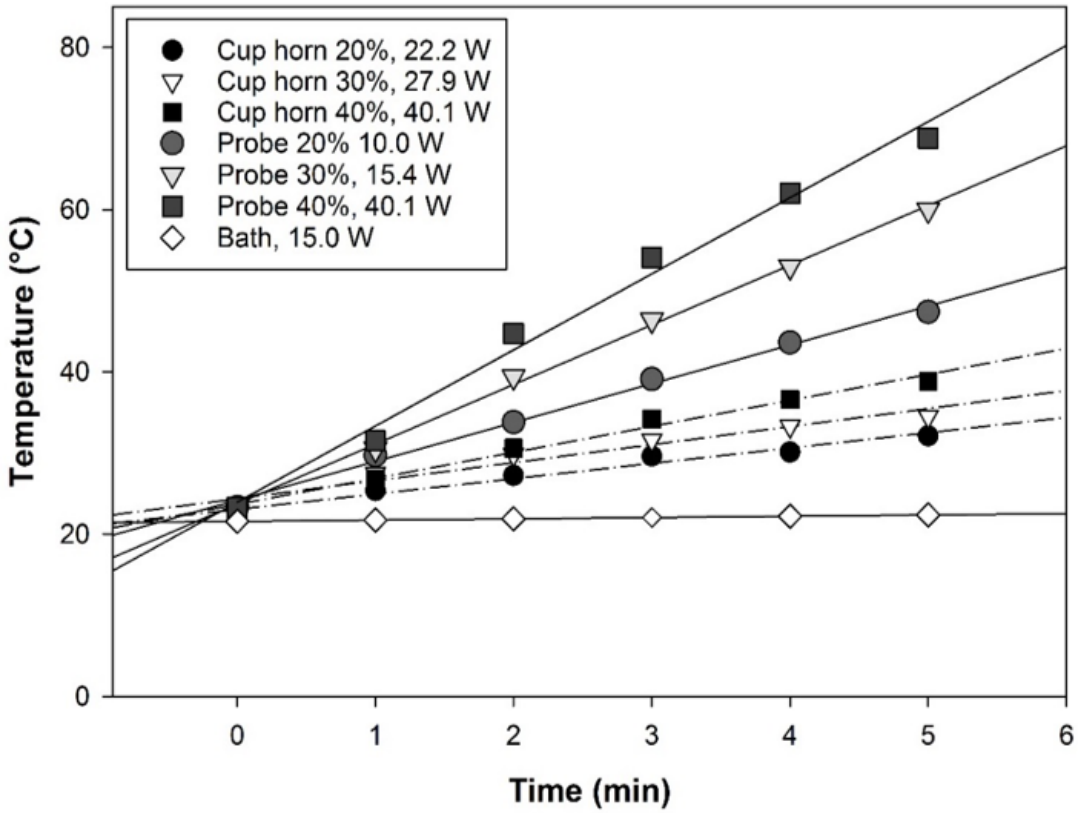


FIGURE 2.3: Calibration curve of probe, cup horn, and probe sonicators. A linear regression was performed for each to determine delivered acoustic power.

was lower (10.0, 15.4, and 19.6 W, respectively) due to the small diameter of the probe. The equivalent energy was therefore normalized by probe surface area.

### 2.4.2 Agglomerate size

The HDD was measured immediately after sonication to evaluate the efficacy of sonication on NP dispersion. For both $CeO_2$ and $TiO_2$, the HDD was significantly lower after sonication relative to the unsonicated control in all three dispersion media (Fig. 2.4). Agglomerate size did not vary significantly among sonicator types or amplitudes when an equivalent energy was input. $TiO_2$ agglomerates were generally larger than $CeO_2$ in ultrapure water and 0.1 mM

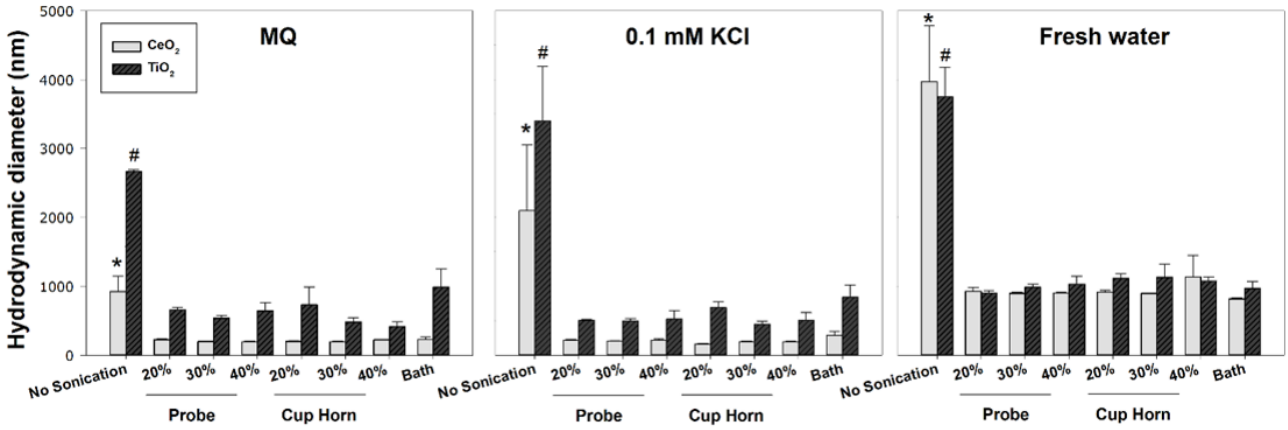


FIGURE 2.4: Hydrodynamic diameter of $CeO_2$ and $TiO_2$ NPs after probe and cup horn ultrasonication (20%, 30%, and 40%) and bath sonication in ultrapure water, 0.1 mM KCl, and FW. There was no significant difference in HDD among sonication conditions. The HDD of all sonicated groups was statically different from the no sonication control ($p < 0.05$).

KCl. $TiO_2$ also had higher polydispersity and higher variance among technical replicates.

### 2.4.3 Energy dependence

Energy input was varied from approximately 2000-16800 J (0.1x —10x energy/unit surface area) by altering the sonication time for NP suspensions in ultrapure water to evaluate the effect of energy delivered on HDD. For programmed power amplitudes of 30%, the HDD of $CeO_2$ decreased with increasing energy and HDD reached a minimum of approximately 120 nm (Fig. 2.5). The HDD of $TiO_2$ NPs decreased and reached a minimum of approximately 600 nm at 8400 J while higher sonication inputs resulted in increased variance and a slightly higher average HDD.

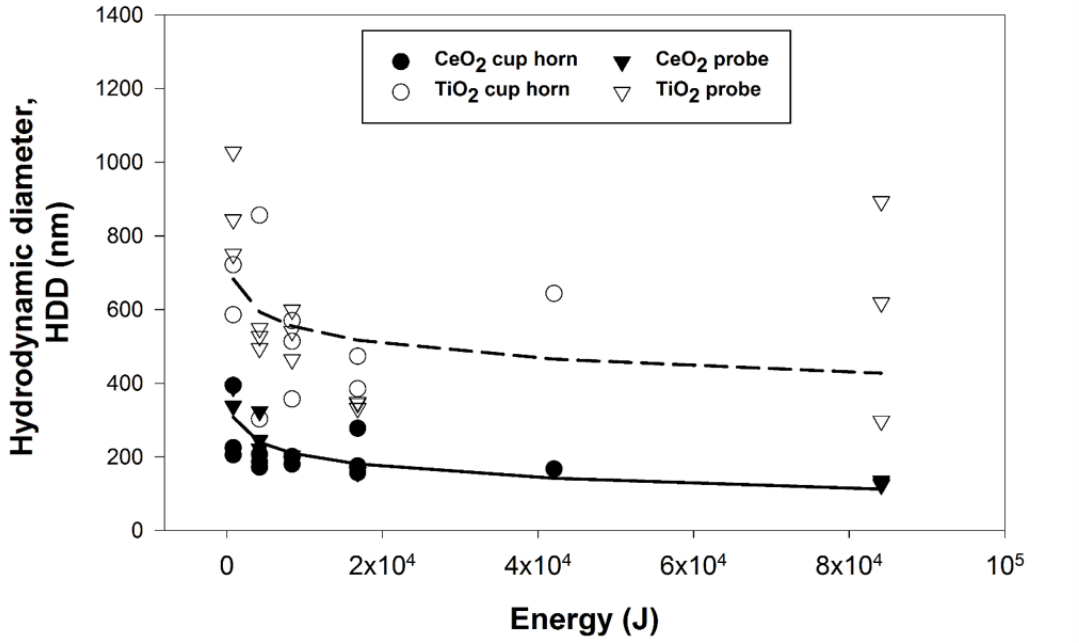


FIGURE 2.5: HDD of $CeO_2$ and $TiO_2$ NPs in ultrapure water after probe and cup horn ultrasonication at 30% amplitude with delivered energy of 8400 J, 1/10x energy (840 J), 1/2x energy (4200 J), 2x energy (16800 J), and 10x energy (84000 J). HDD as a function of energy was fit to a first order exponential decay.

## 2.5 Discussion

This study assessed current practices of ultrasonicating nanoparticle dispersions for toxicity testing. A review of published studies found that significant discrepancies exist among studies and protocols vary greatly in instrumentation and energy input. Additionally, most studies do not provide sufficient detail and do not report pertinent information about energy, medium, sample volume, or concentration, all of which are necessary for reproducibility. These metadata significantly contribute to the impact of acoustic energy on NP dispersion. The lack of standardized practices results in exposure variance that can impact our understanding of NP-biological interactions and influence the results of toxicity

testing.

We successfully calibrated three major types of sonicators to deliver equivalent acoustic energy. Importantly, this provides a means for labs with different equipment to adapt existing protocols and increase uniformity in NP dispersions across studies. The times and powers used in this study produced NP dispersions of similar hydrodynamic diameters for all three sonicator types and power inputs. This suggests that consistent dispersions can be prepared with equipment available to each lab if sufficiently characterized and calibrated.

Although calorimetric calibration of individual sonicators is recommended by standard guidelines and used in a limited number of studies, it is clearly not widely implemented in preparation of NP dispersions for toxicity testing. The present study extends current calibration methods to include cup horn and bath sonication for direct comparison independent of instrumentation. We also demonstrate that smaller volumes and concentrations can be used for sonication, which reduces NP waste.

Current standard protocols exclusively recommend high intensity probe sonication for NP disruption, but many studies use bath or cup horn sonication in practice to avoid contamination of the sample. This may also be due to the availability of instrumentation, as bath ultrasonicators are common and less expensive than other options. Some studies working with controlled biological conditions intentionally opt for indirect methods to prevent contamination of the NP exposure by the sonication probe [62].

Among the nanotoxicology studies we reviewed, ultrasonic bath was the most commonly used type of sonicator for NP dispersion. Protocols only outline specific user guidelines for a probe sonicator, so dispersion techniques with a bath system were not consistent, and sonication times ranged from 10 minutes to 6 hours. Standard dispersion protocols should be modified to include guidelines

on bath sonication in order to standardize practices across research groups. We calibrated the ultrasonic bath using calorimetry and insulated the top to the best of our ability to minimize heat loss. A power of 15 W was delivered to the system, which is significantly lower than the reported instrument output power of 70 W. The manufacturer reported power does not account for energy loss as electrical energy is converted to mechanical energy, thus it does not accurately represent the delivered acoustic power.

Probe and cup horn sonication was performed using the same ultrasonic power supply equipped with different probe attachments. The NP sample volume was 10 mL for indirect methods but for was increased to 40 ml in a 50 mL conical tube for direct sonication to submerge the probe without allowing direct contact with the sides of the tube. Volume determines the energy density, so at a given concentration, sonication system, and NP material, lower volumes can cause a greater disruptive effect [70]. However, the proximity of NP sample to the probe also determines the disruptive effect and despite the higher volume used for probe sonication, the majority of the NP sample is in close proximity to or in direct contact with the probe. Standard protocols recommend a volume of 125 ml in a glass beaker but we demonstrated that smaller volumes can be used, which reduces the amount of NP needed, as well as the amount of NP waste generated.

For the calibration of power delivered by the cup horn, the mass term in Eq.2.1 was determined using density of water (1 g/mL) and the volume of both the NP sample and the water bath through which the energy travels. Much of the delivered sonication energy is dissipated through the water in the cup horn, and this was observed during calibration by a lower temperature change despite a higher power output from the instrument. The delivered power is used to heat a larger total volume. The cup horn was more difficult to insulate so the

delivered power may be an underestimate. The lower power delivered by the probe also indicates that less overall power was required to vibrate the probe at a certain amplitude. The lower surface area of the probe (1.3 $cm^2$ vs. 31.7 $cm^2$) causes the power to be concentrated at the tip and produce a higher intensity energy, thus we normalized sonication energy by probe surface area instead of overall energy.

Manufacturer recommendations suggest that for a given amplitude, the cup horn sonication time should be 4 times that of the probe time to achieve a similar NP dispersion. However, our calculations called for times of approximately 12 times longer for cup horn than the probe, depending on the amplitude, and we conclude that this rule should not be generally applied. Our results emphasize that surface area of the probe should be reported and taken into account when selecting a sonication protocol. Many sizes are available, ranging in diameter from 2 mm to 25 mm, which result in a wide range of delivered intensities.

The power determined by calibration was lower than the instrument reported power for all three sonication systems (Table 2.1). This could be due, in part, to difficulties in insulating the system during calorimetric calibration. The difference was greater for the probe sonication system than the cup horn, with the calibrated power approximately 70% lower on average than the instrument reported power. For the cup horn, the difference was less significant at a programmed amplitude of 20%. This may indicate that higher amplitudes have more energy loss and the instrument readout is less accurate. The larger temperature changes during calibration for higher powers may result in more uncertainty due to heat loss from the system, a trend which could potentially be minimized by performing calibration curves over shorter periods of time. The amplitudes selected here were chosen because 20% is the minimum allowable on the instrument and 40% is the maximum for cup horn and microtip attachments.

The calibrated energy produced comparable dispersions using different sonicators and power settings, but differences were still observed between $CeO_2$ and $TiO_2$ NPs, despite having a similar primary particle size. The HDD of $TiO_2$ was larger than $CeO_2$ in ultrapure water and 0.1 mM KCl, which is consistent with what other studies have observed [93, 36]. The variance of measured HDD was generally higher for $TiO_2$ NPs, which may be attributed to the higher polydispersity index (PDI) values. PDI values (Table A2) were higher for $TiO_2$, indicating that $TiO_2$ suspensions had a broader size distribution than $CeO_2$. Normalizing for sonication energy and parameters allows for interpretation of material specific agglomeration behavior attributed to the NP surface and properties of the exposure media.

The effect of sonication type and programmed amplitude was evaluated in three different dispersion media: ultrapure water, 0.1 mM KCl, and freshwater. Ultrapure water is recommended in OECD guidelines for stock preparation. KCl was selected here as a model weak salt solution consisting of monovalent cations, and simulated freshwater (FW) was used here to represent testing conditions for freshwater toxicity tests. FW has a higher ionic strength and contains divalent cations, which have been shown to form ionic bridges between adjacent particles and increase agglomeration [152]. Higher ionic strength affects the particle surface charge and can compress the electrical double layer, causing a weaker electrostatic repulsive force [6, 204]. Agglomeration is most significant at the isoelectric point (IEP), the pH at which the repulsive surface charge of NPs is neutralized and the suspension becomes unstable. The IEP of $TiO_2$ (anatase) has been shown to be a function of primary particle size, and is approximately pH 5.2 for 26 nm [195]. The IEP of $CeO_2$ NPs has been reported to range from pH 6 to pH 8 [17, 171]. The isoelectric point can shift in high ionic strengths and in the case of $TiO_2$ (anatase) shifts up to possibly become less stable at

neutral pH [98]. As expected, both NPs had significantly larger HDD in FW than in MQ or KCl.

The total energy was varied for the probe and cup horn sonicators by changing sonication time. For $CeO_2$ in ultrapure water prepared with both types of sonicators, an increase in energy led to a decrease in HDD. The HDD reached a minimum of approximately 120 nm (Fig. 2.5). The HDD of $TiO_2$ NPs decreased with increasing energy until 8400 J, when the variance increased and the average HDD appeared to increase. This is consistent with previous studies which have observed that increasing sonication can actually lead to the re-agglomeration of NPs due to increased particle collisions [210]. One value for sonication energy is therefore not suitable to minimize HDD for all nanomaterials meaning that energy needs to be independently optimized for each material. Studies have proposed the use of a critical delivered sonication energy to systematically determine the energy required to minimize HDD for each specific NP suspension [36, 46]. The work shown here is a necessary prerequisite for the wide implementation of such approaches.

## 2.6 Conclusion

This study illustrates that sonication energy is most important when considering reproducibility of NP dispersion protocols, especially when evaluating toxicity. We found that despite many published protocols to standardize dispersion preparation, significant discrepancies exist in sonication procedures and reporting in nanotoxicology studies. Calorimetric calibration is a simple method that can be used to report equivalent energy across sonicator types and power input. We modified existing calibration techniques to account for differences in probe surface area, and conclude that this simple approach should be applied

in future studies improve compliance in standard methods and significantly improve reproducibility. The results shown here suggest that delivered energy, not sonicator type, is the determining factor for the agglomeration state of NPs in a given dispersion medium. For standardization across nanotoxicology studies, we recommend reporting appropriate metadata (concentration, volume, dispersion medium) in addition to energy and agglomerate size to best characterize NP exposure in relevant media.

# 3 Adaptive methodology to determine hydrophobicity of nanomaterials *in situ*

Lauren E. Crandon, Padmaja Chavan, Bryan J. Harper and Stacey L. Harper

## 3.1 Abstract

The hydrophobicity of nanoparticles (NPs) is a key property determining environmental fate and toxicity. Attempts have been made to apply existing methods for evaluating the hydrophobicity of bulk solids, chemicals, and proteins to NPs, but all have significant limitations. There is currently no consensus on the best method to quantify the surface hydrophobicity of nanomaterials, which impedes the development of predictive fate models. In this study, we modified and evaluated two potential methods to determine the hydrophobicity of NPs, hydrophobic interaction chromatography (HIC) and dye adsorption, and compared them to the octanol-water partitioning method commonly used for organic chemicals. Gold, copper (II) oxide, silica, and amine-functionalized silica (Ami-$SiO_2$) NPs were used to evaluate methods based on their ability to be applied to particles with agglomeration and surface coatings. HIC quantified the interaction between Au NPs and hydrophobic octyl ligands, and hydrophobicity was measured as the proportion of NPs retained in the column after elution with an aqueous phase. Dye adsorption evaluated the relative adsorption of a hydrophobic dye (Rose Bengal) and a hydrophilic dye (Nile Blue) to the NP surface. Au NPs were consistently deemed hydrophilic using the octanol water partitioning and HIC methods, but despite having a small size and stable suspension, particles could not be fully recovered from the HIC column. For the dye adsorption method, experimental adsorption of Rose Bengal and Nile Blue was fit to the linear isotherm model and the fitted $k_{lin}$ parameter of each dye and NP adsorbent was used as a metric for hydrophobicity. CuO was determined to be slightly hydrophilic, while $SiO_2$ was hydrophilic and Ami-$SiO_2$ was hydrophobic. The advantages and limitations of each method are discussed, and the dye adsorption method was determined to be most suitable for application across broad classes of nanomaterials.

## 3.2 Introduction

Despite increasing commercial and industrial use of nanoparticles (NPs) in areas such as sunscreens, cosmetics, catalysts, pigments, and antimicrobials, little is known of their environmental impact [190]. Estimates predict a rise in global consumption of nanomaterials from approximately 308,322 metric tons in 2016 to 733,220 metric tons in 2021 [20]. Once released, NPs encounter dynamic and complex environments and their surfaces are transformed. Currently there is not sufficient information to establish predictive structure-activity relationships, mostly due to lack of physicochemical characterization of nanomaterials in exposure conditions [9]. Attempts made to draw parallels between descriptors of chemicals and nanomaterials have not been widely implemented [121].

One of the most powerful and useful descriptors of chemicals is relative hydrophobicity. Hydrophobicity is an important parameter in risk assessment that can be used to predict movement through soil, transport in aqueous environments, bioavailability to organisms, and partitioning in physiological systems [60]. Hydrophilic chemicals will remain in the water column, which could increase exposure to aquatic species or downstream organisms, but could have reduced bioavailability and consequently lower toxicity. Hydrophobic compounds, on the other hand, may partition to the sediment, have increased bioaccumulation and have been shown to have increased risk of biomagnification [43, 61].

Hydrophobicity is also thought to be a key parameter for the prediction of environmental behavior and biological interactions of nanomaterials [222, 234]. Just as with chemicals, hydrophilic NPs are more likely to remain in the water column and potentially have increased mobility, whereas hydrophobic particles are more likely to bind to sediment organic matter. In addition, surface adsorption, which expected to be dictated in part by hydrophobic interactions, is a primary factor determining NP interactions in the environment [222]. When

NPs enter the environment, they encounter environmental constituents such as natural organic matter (NOM), ions and polysaccharides, which adsorb to the NP surface and form a dynamic corona , altering the NP surface properties and influences the fate, transformations, and uptake of the NPs [236]. The composition of the corona is likely to be influenced by the hydrophobicity of the NP and affinity for the surrounding environmental surfaces [138].

This concept is further applied to describe the interaction of NPs with organisms. Hydrophobic NPs have shown to interact with the lipid bilayer of organisms, and evidence suggests increased uptake relative to hydrophilic NPs [109]. Once taken up by an organism, NP surface hydrophobicity has been shown to directly affect toxicity, circulation time, and bioaccumulation [95, 136]. Additionally, hydrophobicity dictates interaction of the NP surface with biological components such as proteins and biomolecules which adsorb to the surface, further altering biological interaction [2].

Nanoparticle-specific considerations add to the complexity of measurement and interpretation of hydrophobicity metrics. NPs can be comprised of various sizes and surface functionalization, both of which affect partitioning behavior and interactions. Hou et al. found that the size of Au NPs affected how quickly NPs distributed to solid-supported lipid membrane, while surface functionality and solution chemistry determined the "apparent" steady state concentrations [74]. Agglomeration can also affect fate and complicate measurements by causing settling of NPs over time and preventing true partitioning behavior [204]. NPs are often functionalized with various surface coatings and alter surface hydrophobicity. Previous studies have found that changes in hydrophobicity of the particle surface can alter cell interaction and consequent uptake [139]. It was found that attachment of Ag NPs to hydrophobic collector surfaces was directly proportional to hydrophobicity of coatings (citrate, PVP, and GA) [188].

Therefore a useful measure of hydrophobicity is needed that accurately represents complex and dynamic NP behavior.

Traditional methods to quantify the hydrophobicity of chemicals and solid surfaces rely on partitioning or other equilibrium dependent measurements. However, NPs do not reach thermodynamic equilibrium, so kinetically controlled parameters are more relevant and appropriate [162]. Progress has been made to obtain values for attachment efficiency ($\alpha$) of NPs which can be directly applied to model the deposition of NPs to a collector surface as using the Smoluchowski equation. This method is well established to modeling the coagulation of particles and have been shown to successfully quantify the attachment of NPs to surfaces in complex environments [19, 65, 160, 161, 202]. However, $\alpha$ must be experimentally determined for each pair of surfaces and is dependent on media properties such as ionic strength, pH, and concentration of organic matter. There is a need to quantify the inherent surface hydrophobicity of NPs to predict attachment of NPs to surfaces using computational fate models in a manner parallel to forecasting the partitioning of chemicals into environmental compartments.

Existing methods for characterizing the hydrophobicity of substances have been applied to NPs and met with varying degrees of success. Examples of these methods include contact angle, which is typically used to evaluate the hydrophobicity of solid surfaces, octanol-water partitioning, which is commonly used for chemicals, and hydrophobic interaction chromatography, which provides a relative measure of the hydrophobicity of proteins. In some cases, these methods have been modified for NP specific behavior.

Contact angle measures the wettability of a solid surface by a probe liquid, typically using the sessile drop technique, and measuring the angle at the solid-liquid-vapor interface. When using water as a probe, an angle ($\theta$) of $< 90°$

indicates a hydrophilic surface and $\theta > 90°$ hydrophobic surface (90° is considered amphiphilic). To apply this technique to nanomaterials, a NP suspension is first pressed into a flat disk, often by filtration, before applying the probe liquid. This method was performed across a series of rare earth oxide NPs and all were found to be hydrophobic, with water contact angles between 100° and 115° [16]. A similar method was applied to fullerenes, fullerols and coated Ag NPs at the liquid, liquid, solid interface and all were found to be hydrophilic, which was inconsistent with other measurements [223]. Arnaudov *et al.* used a gel trapping technique to eliminate the need to press NPs into a flat disk, but this method requires advanced techniques such as atomic force microscopy and does not consider effects of agglomeration or functionalization [12]. A major limitation of using contact angle for hydrophobicity is that is does not allow for experimental in situ measurements [16, 45, 223]. Additionally, it does not take into account NP size, shape, surface roughness, or heterogeneity [124].

If NP suspensions are modeled as homogeneous, the partitioning behavior between two immiscible liquid phases has been used to evaluate hydrophobicity. The octanol-water partitioning coefficient ($K_{OW}$) is commonly used for chemicals and is a powerful descriptor to model environmental fate and bioavailability for risk assessment [129]. Octanol is used as a surrogate for organic rich material, such as the sediment or a lipid membrane. This measurement, when applied to dissolved chemicals, assumes that solutes move freely between two phases, and the equilibrium concentrations represent the "affinity" for each phase.

NP suspensions violate the basic assumptions of solubility and equilibrium associated with $K_{OW}$, but many studies still apply this measure to evaluate the hydrophobicity of NPs [162]. The shake flask method has been most commonly applied to fullerenes, and although they are generally characterized as very hydrophobic, exact values are not consistent among studies and span

orders of magnitude [80, 223]. This method has also been applied to carbon nanotubes, in which the obtained $K_{OW}$ values were found to not be predictive of bioaccumulation in earthworms or oligochaetes. The $K_{OW}$ of nanomaterials has been reported to be inconsistent with organic compounds of a similar chemical structure, with aggregation, size and surface coatings all being cited as possible explanations [156].

Some studies have attempted to obtain a $K_{OW}$ value for NPs while acknowledging the shortcomings or making efforts to adapt the results for particle-based systems. When applying the shake-flask method to measure $K_{OW}$, a fraction of some nanomaterials have been observed to partition at the interface between the aqueous and octanol phases. A two parameter distribution coefficient has been proposed to analyze measurements in this scenario, where the mass ratio of NPs in the aqueous, organic, and interface are all taken into account [75]. The resulting measurements are system-dependent and a function of area of the interface, particle count, and time. Another proposed adaptation is to evaluate the $K_{OW}$ of the surface functional groups alone, and assume that the core has a negligible effect on surface hydrophobicity [107]. This is likely most suitable for NPs with small cores and large, branched organic coatings. $K_{OW}$ measurements of this nature may be useful to compare within a class of nanomaterials but have not been widely implemented.

An alternative method to evaluate hydrophobicity of NPs is hydrophobic interaction chromatography (HIC). HIC is typically used to separate proteins based on their relative hydrophobicity [165]. Proteins are eluted through a column by a stepwise decrease in salt concentration, where the most hydrophobic proteins are eluted at the lowest salt concentration. The stationary matrix of the column is typically comprised of agarose beads functionalized with alkyl chains of various lengths. While this method is potentially suitable for application

with NPs due to the similar size range of proteins, it has only been applied to measure hydrophobicity of NPs in a limited number of studies. Polystyrene NPs were evaluated at a constant salt concentration and the elution volume required to completely remove particles from an alkyl-agarose column was used as a measure of hydrophobicity [29]. Another adaptation was to use multiple columns with varying alkyl chain lengths to compare hydrophobicity of various polymeric NPs [85]. HIC can potentially be used for particles with a wide range of hydrophobicity because the stationary phase can be selected by the user.

The adsorption of hydrophobic dyes to the particle surface is another method that is potentially well suited to NPs. This method has been applied to fluorescently labeled polystyrene NPs, latex particles with various functional groups, and solid lipid NPs using Rose Bengal, an organic dye, as a hydrophobic probe [50, 139, 170]. Some difficulties identified were interference from surfactants, time intensive range-finding for suitable NP concentrations, and difficulty separating NPs from suspension for absorbance analysis. Rose Bengal provides robust measurements for hydrophobic NPs but provides limited information about hydrophilic surfaces. A hydrophilic dye, Nile Blue, has been proposed as a means to provide resolution to measurements of hydrophilic particles [223]. The use of both a hydrophobic and hydrophilic dyes is promising to provide measurements with good resolution to compare NPs with a wide range of compositions.

In this study, we evaluated HIC and dye adsorption to evaluate the hydrophobicity of NPs, and compared them to traditional partitioning methods. The results were evaluated based on the ability of each method to overcome major challenges associate with NPs: agglomeration and surface functionalization. Uncoated gold (Au) NPs were selected for their small size and ability to be easily quantified by absorption spectroscopy. Uncoated copper oxide (CuO)

NPs were used for their known propensity to agglomerate in solution, and silica ($SiO_2$) with and without amine surface functionalization were chosen to evaluate the ability of the methods to observe changes in hydrophobicity due to surface coatings. We adapted protocols to improve use for widespread applicability to NPs, with the ultimate goal of obtaining useful measurements for future fate models.

## 3.3 Experimental

### 3.3.1 Nanoparticle preparation

Stock suspensions (1000 mg/L) of 14 nm Au (U.S. Research Nanomaterials, Inc. Houston, TX), CuO (<50 nm, Sigma Aldrich), 80 nm $SiO_2$ and aminated $SiO_2$ (NanoComposix, San Diego, CA) NPs were prepared in 20 mL ultrapure water (Milli-Q 18.2 Ω resistivity, Merck Millipore, Burlington, MA) and sonicated with a cup horn style sonicator equipped with a circulating water bath to maintain temperature (Vibracell VCX 750, Sonics & Materials, Inc., Newtown, CT) at 40% amplitude for 2 minutes (40.1 W, 4812 J). Stocks were further diluted in ultrapure water.

### 3.3.2 Nanoparticle characterization

The hydrodynamic diameters (HDD) of CuO, Au, $SiO_2$, and Ami-$SiO_2$ NPs were evaluated in ultrapure water immediately following dispersion and sonication. A volume of 1.5 ml was placed in a disposable cuvette for measurement. Zeta potential measurements were performed in 0.5x phosphate buffered saline (PBS) to provide sufficient ionic strength to carry an electrical charge. The detailed parameters for HDD and ZP measurements are described in Table B1.

### 3.3.3 Octanol-water partitioning

The OECD shake flask method [145] was applied to obtain a $K_{OW}$ value for Au NPs. A volume of 4 mL each of ultrapure water and 1-octanol were equilibrated for 24 hours with 0.2 mg Au NPs. The liquid phases were allowed to separate for 4 hours, after which samples were collected from each phase and Au NPs were quantified using a SpectraMax M2 spectrophotometer (Molecular Devices,Sunnyvale, CA, USA) at $\lambda$= 530 nm. Absorbance was converted to concentration using a standard curve prepared in ultrapure water or 1-octanol. The same method was used to evaluate CuO NPs except the absorbance was evaluated at 640 nm.

### 3.3.4 Hydrophobic Interaction Chromatography

HiTrap Octyl FF prepacked HIC columns were purchased from GE Life Sciences (Piscataway, NJ). The bed volume was 1 mL and the stationary phase consisted of a sepharose support matrix of 90 $\mu$ m beads functionalized with hydrophobic octyl ligands, which were selected to parallel the octanol reference phase of the $K_{OW}$ method. The column was loaded with 2 mL of a 10 mg/L Au NP suspension at a flow rate of 1 mL/min. A lower concentration was used (10mg/L) relative to the $K_{OW}$ method to limit agglomeration, which would block flow through the pore space. After loading the column, a syringe pump (Model No. NE-1010, New Era Pump Systems, Inc. Farmingdale, NY, USA) was used to flow 20 mL of 0.5x PBS through the column at 1 mL/min and the eluent was collected in 1 mL fractions. To remove Au NPs retained in the column during PBS elution, a surfactant (0.1% Triton X-100, laboratory grade, Sigma-Aldrich, St. Louis, MO), was pumped through the column at 1 mL/min for another 20 minutes, and the eluent was again collected in 1 mL fractions every minute. The collected samples from both elution phases were placed in a 96-well plate and

the absorbance at 530 nm was evaluated using UV-vis spectroscopy to determine Au concentration.

### 3.3.5 Dye Adsorption

The relative adsorption of a hydrophobic probe (Rose Bengal, 85% ACROS Organics, New Jersey, USA) and a hydrophilic probe (Nile Blue A, ACROS Organics, New Jersey, USA) to the NP surface was used as a measure of hydrophobicity (Fig 1). Dye concentrations (0.5-30 $\mu$M) were prepared in ultrapure water. Equal volumes of dye and NP stock were combined in 1.5 mL microcentrifuge tubes for each concentration and incubated in a tube rotator for 90 minutes. Controls were prepared by adding dye to ultrapure water to account for any observed loss of dye due to adsorption to the vials. To evaluate potential degradation of dye by reactive oxygen species (ROS) from the NP surface, controls were prepared with various concentrations of $H_2O_2$. Each sample was prepared in triplicate. Following incubation, NPs were removed from solution by centrifugation for 30 minutes at 14000 rpm. The remaining concentration of dye in the supernatant was analyzed using UV-Vis spectroscopy at $\lambda$= 543 nm for Rose Bengal and $\lambda$= 620 nm for Nile Blue. This method was performed with final concentrations of 500 mg/L $SiO_2$ and Ami–$SiO_2$ and 250 mg/L CuO. A lower CuO concentration was selected to optimize results with the dye concentrations while minimizing agglomeration effects.

The amount of dye adsorbed to the NP surface ($q_e$) was calculated using Eq.3.1:

$$q_e = (C_0 - C_e)\frac{V}{m} \tag{3.1}$$

where $C_0$ is the initial dye concentration, $C_e$ is the concentration of dye re-

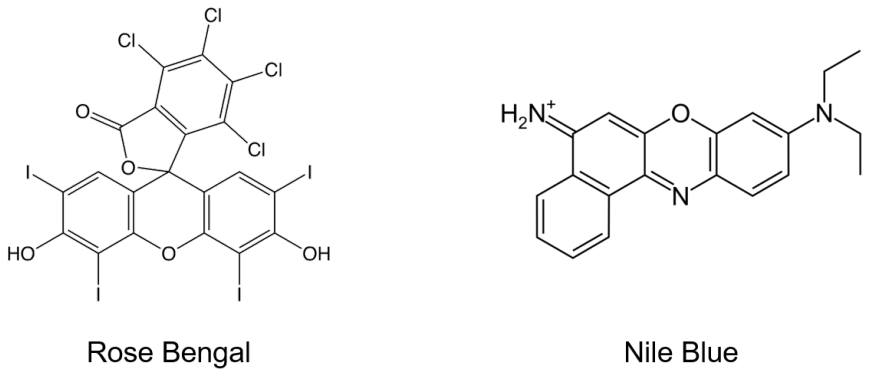


FIGURE 3.1: Structures of the hydrophobic (Rose Bengal) and hydrophilic (Nile Blue) probes.

maining in the supernatant after centrifugation, V is the volume (L) and m is the mass of NPs (g). The adsorption of dyes was fit to Linear (Eq. 3.2), Langmuir (Eq. 3.3) and Freundlich (Eq. 3.4) type isotherm models. Each model was fit by minimizing the sum of squared errors in SigmaPlot (Systat Software, San Jose, CA, USA) to determine the linear adsorption constant, $k_{lin}$ (L/g), the adsorption capacity, $q_{max}$ ($\mu$mol dye/$g_{NP}$), the Langmuir adsorption constant , $K_L$ (L/$\mu$mol) for the Langmuir model, and the adsorption capacity, $K_f$ (L/$\mu$mol) and adsorption intensity, 1/n for the Freundlich model.

$$q_e = k_{lin} C_e \tag{3.2}$$

$$q_e = \frac{q_{max} K_L C_e}{(1 + K_L C_e)} \tag{3.3}$$

$$q_e = K_f \, C_e^{\frac{1}{n}} \tag{3.4}$$

#### 3.3.5.1 Environmental transformations

To simulate the environmental release of NPs and evaluate the effect on dye adsorption, natural water samples were collected from Mill Creek Park in Sheridan, Oregon. The pH and conductivity were measured at the time of collection. The samples were later filtered using a 0.44 $\mu$m Whatman GF/F glass fiber filter to remove particulate matter prior to alkalinity and hardness tests. Concentrations (0-250 mg/L) of $TiO_2$ NPs were prepared in the water samples and allowed to incubate for 24 hours. NPs were then removed by centrifugation and resuspended in ultrapure water, after which the previously described method for dye adsorption was performed. Instead of a range of dye concentrations, methods were adapted from Xiao *et al.* using 10 mg/L of each dye and a range of $TiO_2$ NP concentrations, which were later converted to surface area using the measured hydrodynamic diameter [223].

### 3.3.6 Statistical analysis

SigmaPlot version 13.0 (Systat Software, San Jose, CA, USA) was used to perform all statistical analyses. All experiments were performed in triplicate. Area under the curve (AUC) measurements for HIC analysis were performed in SigmaPlot using the built in graphical integration function.

## 3.4 Results and Discussion

### 3.4.1 Nanoparticle characterization

Au, $SiO_2$, and Ami-$SiO_2$ NPs were all stable in suspension and had an average HDD of 76.8 ± 1.5 nm, 100.3 ± 0.3 nm, and 113.5 ± 0.5 nm in ultrapure water, respectively, which is similar to their primary particle size (Fig 3.2A). CuO NPs showed a high degree of agglomeration, with an average HDD of 556

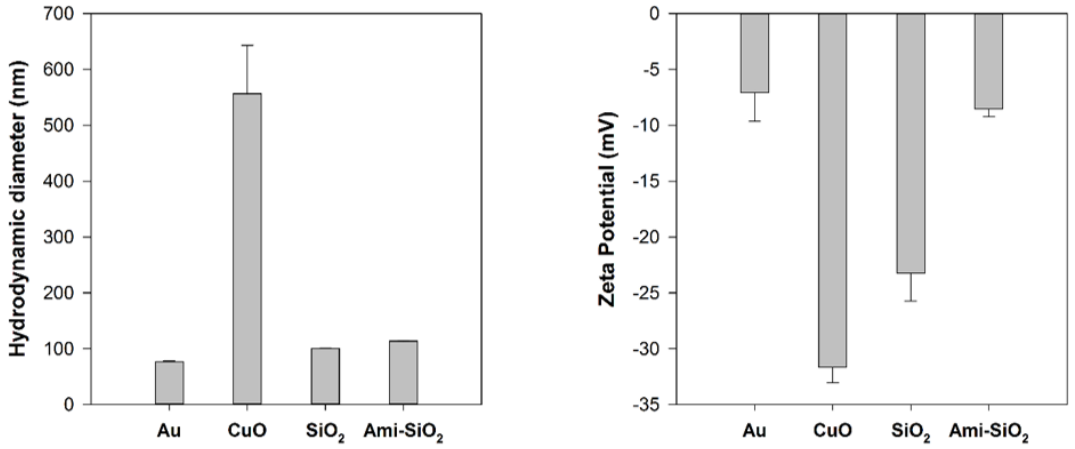


FIGURE 3.2: Hydrodynamic diameter of Au, CuO, $SiO_2$, and Ami-$SiO_2$ evaluated in ultrapure water and zeta potential evaluated in 0.5x PBS.

± 87 nm in ultrapure water compared to a primary particle size of $<$ 50 nm. Agglomeration is expected to be more significant in complex media such as the 0.5x PBS buffer used for zeta potential measurements [93]. The ZP of the CuO NPs was -31.7 mV, indicating that despite high agglomeration, the suspension was stable. The zeta potential shows that all particles had a negative surface charge in 0.5x PBS (Fig 3.2B). The surface charge of Ami-$SiO_2$ was neutralized relative to $SiO_2$. The isoelectric point of Ami-$SiO_2$ is pH 7.5 compared to 2.5 for $SiO_2$, so below this pH the surface would be expected to be positively charged. The pH of the PBS solution was approximately 7.8.

### 3.4.2 Octanol water partitioning ($K_{OW}$)

Au and CuO NPs were selected to evaluate octanol-water partitioning because the particles can be easily quantified using UV-Vis spectroscopy. Au particles partitioned to the aqueous phase and remained suspended (Fig. B.1). No visible Au NPs were observed at the octanol-water interface. A log $K_{OW}$ of approximately -2.1± 0.6 was calculated, suggesting Au NPs are hydrophilic.

The log $K_{OW}$ of Au NPs measured in this study was compared to published

values for Au, and it was found that the reported hydrophobicity of elemental gold is not consistent among studies. Native gold flakes were found to be hydrophobic and floated in water [7]. However, Smith *et al.* performed a comprehensive review of studies that characterized the contact angle of Au, and found opposing conclusions about its hydrophobic or hydrophilic nature. Performing Auger electron spectroscopy before and after each measurement revealed that organic impurities were causing hydrophobic measurements, and clean gold surfaces were determined to be inherently hydrophilic [186]. The modeled value of log $K_{OW}$ for elemental Au was found to be slightly hydrophobic (log $K_{OW}$ Au = 0.03), while ionic forms were hydrophobic (log $K_{OW}$ $AuCl_3$ = 0.16) or hydrophilic (log $K_{OW}$ AuCl = -0.46) depending on the valency [32].

CuO NPs were visually observed to aggregate at the liquid-liquid interface and settled to the bottom of the vial over time (Fig B.2). Additionally, CuO in the octanol phase could not be accurately quantified because they did not disperse in octanol (Fig B.3). The measured log $K_{OW}$ was -0.34 ± 0.39. Modeled log $K_{OW}$ values of the bulk and dissolved phases were estimated to be -1.10 for CuO, 0.52 for $CuCl_2$, and 0.16 for elemental copper [32]. This is consistent with experimentally determined contact angle measurements of Cu films, which showed a change from slightly hydrophobic to slightly hydrophilic as the surface oxidized to CuO [115]. CuO is known to exhibit some dissolution of $Cu^{2+}$ in aqueous systems which may also affect the hydrophobicity at the surface [212].

Despite some limited success in this study and others, the octanol-water partitioning method cannot be widely applied across classes of NPs or systems and should be limited to comparisons among classes of NPs. The overall conclusion of hydrophobic or hydrophilic was in agreement with other measures of hydrophobicity in the literature, so this method may be useful as a preliminary qualitative observation, but measured values do not provide sufficient resolution

or consistency for use in fate models. NP suspensions do not reach a thermodynamic equilibrium between liquid phases, and values for $K_{OW}$ are dependent on NP concentration, time, and size of the vial which affects the area of the liquid-liquid interface. This was particularly evident for CuO NPs, which exhibit significant agglomeration and settling.

### 3.4.3 Hydrophobic Interaction Chromatography

The HIC method was adapted to measure hydrophobicity of NPs by interaction with hydrophobic octyl ligands. Salt concentration was not varied, and instead the mass of particles retained in the column was compared to the mass of particles eluted by an aqueous phase (0.5x PBS). Concentration of Au plotted as a function of cumulative eluent volume (Fig 3.3) shows that a high concentration of Au NPs was initially flushed out in the first column volume, which was likely residual from the loading step. Small concentrations of Au NPs were measured in the eluent throughout the PBS phase. Some Au NPs were initially eluted with the surfactant and represent a small portion of Au retained in the column. The concentration of Au retained in the column was difficult to determine by UV-vis analysis because of interference from the surfactant bubbles, so higher variance was therefore observed in this elution phase relative to the PBS phase (Fig 3.3). Degassing the mobile phase under vacuum may minimize this problem for future studies.

For analysis, the area under the curve (AUC) of concentration vs. volume was evaluated to determine total Au mass in the PBS and surfactant eluents. The ratio was used as a measure of hydrophobicity according to Eq 3.5:

$$K_{OW,HIC} = \frac{AUC_{surfactant}}{AUC_{PBS}} \tag{3.5}$$

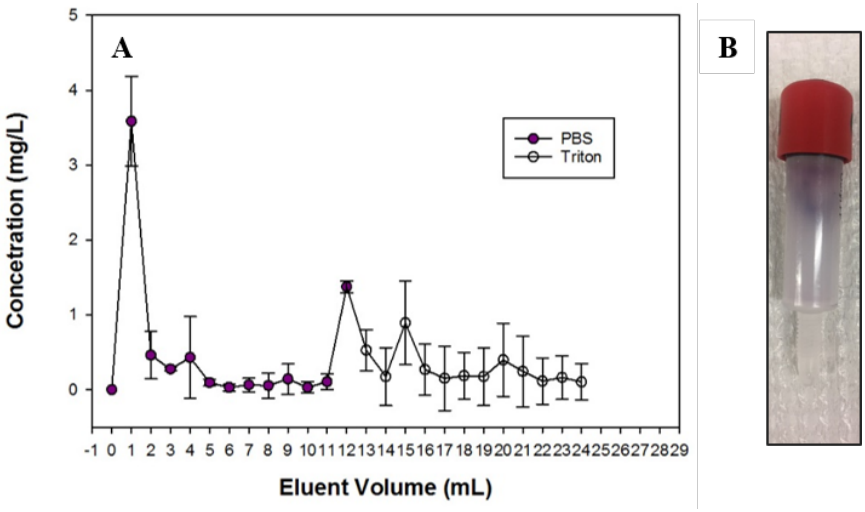


FIGURE 3.3: A) Concentration of Au in the eluent with PBS and Triton mobile phases as a function of total eluent volume. B) Gold NPs visibly retained in column after flushing with 20 mL surfactant and 20 mL 20% ethanol.

Log $K_{OW}$, HIC for Au NPs was calculated to be -0.447 ± 0.006, indicating they are hydrophilic.

Although the HIC method is rapid, directly comparable to log $K_{OW}$, and potentially more appropriate for nanomaterial behavior, several factors limit its widespread use. Au NPs were not fully recovered from the column, and their size likely restricted travel through the pore space. Particles were visually observed to be retained at the top the column, even after flushing with 20 ml surfactant and further attempts to regenerate the column with 20 mL 20% ethanol (Fig 3.3B). Previous studies have also observed higher rates of NP column retention than predicted by classical filtration theory, which models interaction of a single particle with a collector surface, with deposition governed by DLVO forces (electrostatic and Van der Waals) [207]. Chowdhury *et al.* observed an increase in retention of $TiO_2$ NPs in sand columns with increased agglomeration, despite unfavorable electrostatic interactions [34]. This was attributed to straining, which refers to physical retention in the pore structure, and has been

reported to occur when the ratio of NP diameter to bead diameter is greater than approximately 0.002 [108]. In this study, the ratio of the primary particle size (14 nm) to bead diameter (90 $\mu$m) is 0.00016, but using the aggregate size the ratio is 0.0009. Straining likely plays a role in the observed column retention, and would certainly be more severe for particles with more significant agglomeration, such as metal oxides, but may not be the only explanation. Alternative reasons for high retention include charge heterogeneity of the stationary phase and the presence of organic impurities [207].

Theoretically, the columns can ideally be regenerated, but we were unable to completely remove particles after loading. In addition, it was difficult to accurately quantify NPs in the eluent. UV-vis spectroscopy is generally widely available, but many NPs may have absorbance interference with plates or cuvettes, and concentrations in this case were too low for sensitive quantification. Absorbance was not a reliable measure in the surfactant eluent due to interference from bubbles forming in solution. Other methods may be more suitable, such as inductively coupled plasma mass spectrometry (ICP) for metal particles, nanoparticle tracking analysis (NTA) for stable and spherical particles, or other analytical methods for carbonaceous NPs but these are more costly and less accessible.

We were unable to perform HIC due to difficulties in recovering and quantifying NPs concentration in the eluent. Columns with larger pores may improve the usefulness of this method. Salt concentrations can be increased or decreased to alter hydrophobic interactions within the stationary phase. The column stationary phase can be selected to be functionalized with alkyl ligands of various chain lengths, and a lower degree of ligand substitution could also decrease the retention of particles in the column. However, this would be less comparable to $K_{OW}$ and these parameters would need to be optimized for specific nanomate-

rials.

### 3.4.4 Dye adsorption

The dye adsorption method was successfully performed for agglomerated and functionalized particles. Adsorption isotherms were fit to linear, Langmuir and Freundlich models (Table 3.1). The Langmuir model assumes monolayer adsorption on a relatively regular surface [30]. The Freuendlich model describes adsorption on a heterogeneous surface. In general, the data were best represented by the linear and Freundlich models (Table 3.1). The linear adsorption constant, $k_{lin}$, was used as a measure of affinity for each probe to the NP surface. The relative affinity of RB and NB to the surface was evaluated and then Eq. 3.6 was used as a unitless measure of hydrophobicity, shown here as a hydrophobicity ratio (HR).

$$LogHR_{RB/NB} = \frac{k_{lin,RB}}{k_{lin,NB}} \tag{3.6}$$

Previous studies that used RB adsorption to measure hydrophobicity of NPs varied the NP concentration and held the dye concentration constant, plotting fraction of dye adsorbed (known as the partition quotient) as a function of surface area [223]. We adapted these methods and instead plotted adsorption isotherms by varying the dye concentration and using a constant NP concentration. This eliminates the need to calculate NP surface area, which is difficult to measure *in situ* and can contribute to uncertainty in measurements. Additionally, this reduces NP waste and simplifies preliminary range finding for optimizing NP concentration. Adsorption isotherms are well established for suspended particles, and do not require assumptions of spherical geometry or monodispersity to estimate surface area.

TABLE 3.1: Summary of isotherm parameters

| **Linear** | **CuO** | **$SiO_2$** | **Ami-$SiO_2$** |
|---|---|---|---|
| $k_{lin,RB}$ | 0.090 ± 0.127 | 0.254 ± 0.044 | 1.99 ± 0.49 |
| $R^2$ | 0.02 | 0.65 | 0.67 |
| $k_{lin,NB}$ | 2.90 ± 0.07 | 13.23 ± 39.70 | 0.05 ± 0.02 |
| $R^2$ | 0.99 | 0.86 | 0.40 |
| **Langmuir** | | | |
| $q_{max,RB}$ | 3.57 ± 1.13 | — | 44.13 ± 53.01 |
| $K_{L,RB}$ | 1.23 ± 1.96 | — | 0.067 ± 0.10 |
| $R^2$ | 0.11 | — | 0.68 |
| $q_{max,NB}$ | 876.86 ± 4944.49 | 44.81 ± 5.86 | 2.18 ± 5.77 |
| $K_{L,NB}$ | 0.004 ± 0.024 | 0.77 ± 0.20 | 0.03 ± 0.10 |
| $R^2$ | 0.89 | 0.93 | 0.41 |
| **Freundlich** | | | |
| $1/n_{,RB}$ | 0.20 ± 0.21 | 1.23 ± 0.27 | 0.82 ± 0.24 |
| $K_{F,RB}$ | 2.03 ± 0.84 | -0.14 ± 0.10 | 2.94 ± 1.04 |
| $R^2$ | 0.06 | 0.66 | 0.68 |
| $1/n_{,NB}$ | 0.74 ± 0.04 | 0.65 ± 0.063 | 0.88 ± 0.50 |
| $K_{F,NB}$ | 5.94 ± 0.43 | 18.29 ± 0.70 | 0.07 ± 0.07 |
| $R^2$ | 0.98 | 0.90 | 0.40 |
| **Log HR** | **-1.51** | **-1.72** | **1.60** |

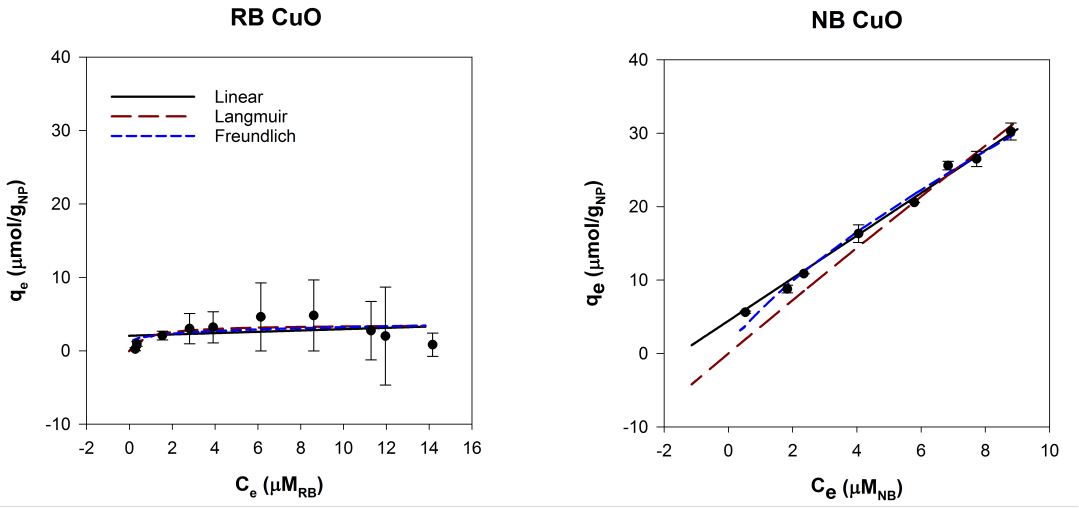


FIGURE 3.4: Adsorption isotherms for 250 mg/L CuO with Rose Bengal and Nile Blue modeled with linear, Langmuir and Freundlich adsorption models.

For CuO NPs, both dyes adsorbed to the surface, but NB had higher adsorption than RB (Fig 3.4). CuO NPs had a high degree of agglomeration (Fig 3.2), which can affect the available surface for adsorption. However, this effect is likely similar for both dyes, and is essentially normalized when Eq. 3.6 applied. This suggests that the dye adsorption method can be used for particles that agglomerate in solution.

$SiO_2$ particles with and without amine functionalized groups were compared using the dye adsorption method (Fig 3.5). Both have low solubility at pH 2-8 and remain stable in suspension. Bare silica was predicted to be hydrophilic (log $K_{OW}$ is -0.66), which is consistent with our results [32]. More NB adsorbed to the $SiO_2$ surface and negligible RB was adsorbed.

Amine groups at the surface drastically altered the hydrophobic interactions of the $SiO_2$ core. Ami-$SiO_2$ showed the opposite trend of $SiO_2$ NPs and had high adsorption of RB and minimal NB adsorption (Fig 3.6). The $k_{lin}$ for RB was 1.99 ± 0.49 and log ($\frac{k_{lin,RB}}{k_{lin,NB}}$) was 1.60. The observed hydrophobic nature

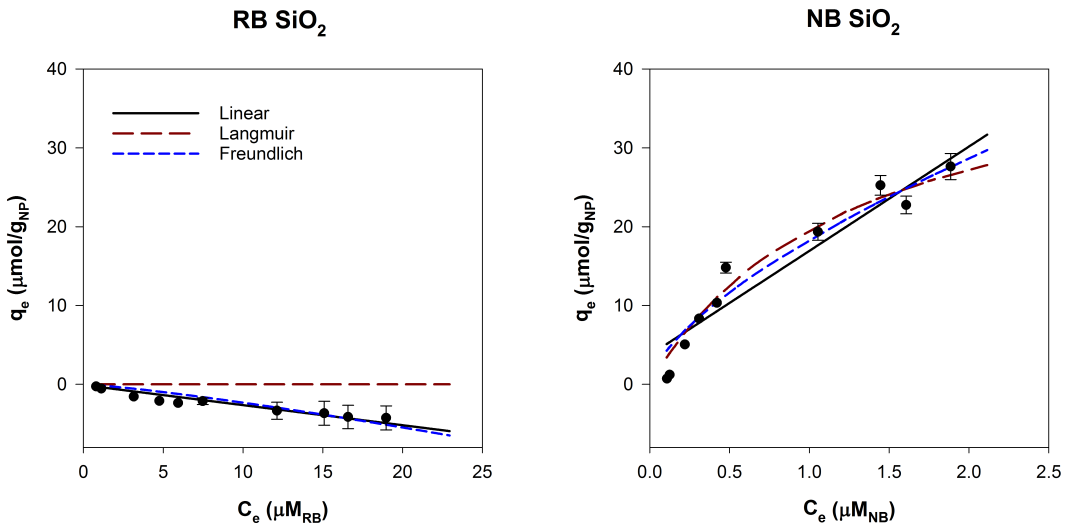


FIGURE 3.5: Adsorption isotherms for 500 mg/L $SiO_2$ NPs with Rose Bengal and Nile Blue, modeled with Langmuir adsorption model.

is consistent with the log $K_{OW}$ for amine groups, which become more hydrophobic with increasing alkyl chain lengths [32]. The results indicate that the dye adsorption method is well suited to evaluate NPs with covalently bound functional groups. This method can measure the change in surface hydrophobicity of NPs due to functionalization and potentially incorporate factors such as size and surface coverage.

When this assay was applied to $TiO_2$ NPs suspended in natural fresh water, there was there was high adsorption of NB (Fig. B.5). This was a shift from the hydrophobic nature of $TiO_2$ NPs observed by high adsorption of RB in ultrapure water. This change is likely due to ions and organic matter which interacted with the NP surface to alter its properties. Prior to measuring dye adsorption, NPs suspended in natural waters were removed and resuspended in ultrapure water because preliminary studies revealed that high salt concentrations caused NB dye to precipitate out of solution. Environmental transformations could still be observed even when the assay was performed in ultrapure water. This

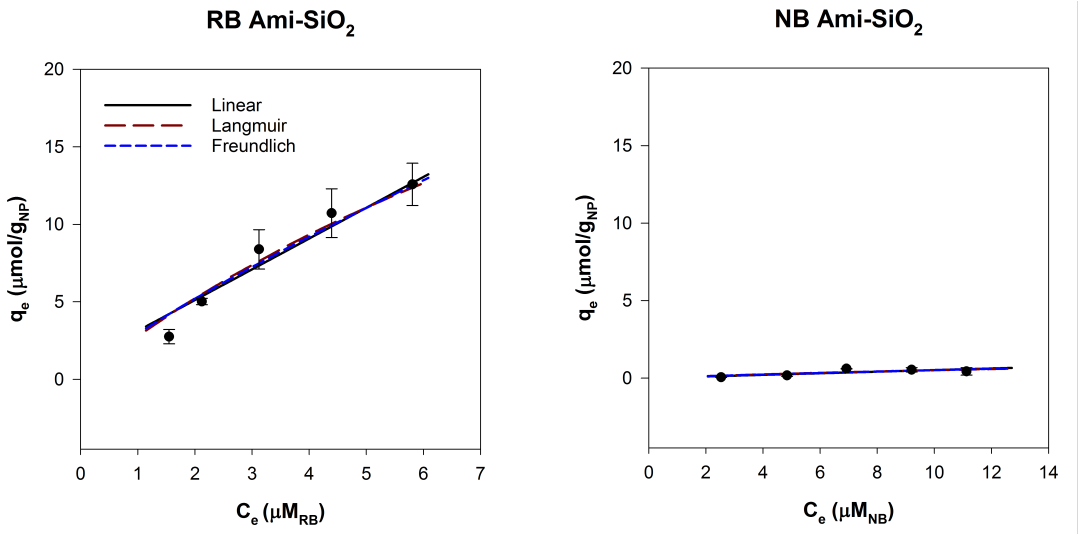


FIGURE 3.6: Adsorption isotherms for 500 mg/L Ami-$SiO_2$ NPs with Rose Bengal and Nile Blue, modeled with Langmuir and Freundlich adsorption model.

method is promising to provide a quantitative measure of changes at the NP surface.

A potential shortcoming of the dye adsorption method is that it is difficult to distinguish between adsorption due to hydrophobic interaction or due to electrostatic interaction. The probes used here are oppositely charged: RB is anionic and NB is cationic. The Ami-$SiO_2$ NPs had a positively charged surface and therefore likely experienced electrostatic interaction with RB. Amine functionalized mesoporous hollow shells were previously found to completely remove another anionic dye, Congo Red, from solution and this was attributed to the oppositely charged surface [211]. However, Congo Red is also hydrophobic (log $K_{OW}$ = 3.57) which could have contributed to the high rate of adsorption. In the current study, CuO suspensions were negatively charged but adsorbed some anionic Rose Bengal, indicating that despite repulsive electrostatic charges, hydrophobic interactions led to adsorption.

The major advantages and limitations of the three methods shown here

are summarized in Table 3.2. Most notably, the dye adsorption assay does not require direct quantification of NPs. This is a major advantage because various methods are used to quantify nanomaterials depending on material composition and availability of instruments, and this can lead to inconsistent values among studies. For metal and metal oxide NPs that dissolve in solution, metal ions could interfere with measurements to quantify NPs, particularly in the octanol-water partitioning method. If dissolution is sufficient to alter the local ionic strength, adsorption processes occurring in both the HIC and dye adsorption methods could be affected [77]. For the dye adsorption method, an ionic control could be used to account for potential complexes that form between the probe dyes and metal ions.

The dye adsorption method, unlike the other methods, produced meaningful results despite high agglomeration of CuO NPs. This method allows for *in situ* measurements without the need for stabilizing agents and potentially can be applied to evaluate the surface hydrophobicity of NPs in more complex environments. Although the probes selected here may produce measurement artifacts due to opposite surface charges, relative differences between NPs can be observed and alternative probes may be explored in the future. We conclude that dye adsorption is most suitable for broad application with NPs.

## 3.5 Conclusions

Adsorption isotherms using RB and NB were successfully used to compare the surface hydrophobicity of NPs. When compared to alternative methods currently being employed, we conclude that the dye adsorption assay is the best in terms of ability to overcome difficulties associated with agglomeration, functionalization, and quantification of nanomaterials, and can likely be widely applied

TABLE 3.2: Comparison of methods to evaluate NP hydrophobicity

| **Method** | **Advantages** | **Limitations** |
|---|---|---|
| $K_{OW}$ | Simple | Violates equilibrium assumptions |
| | Directly comparable to existing measurements and fate models | Must directly quantify NPs |
| | | Settling of NPs affects measurements |
| | | Measurement depends on particle count, area of interface, etc. |
| HIC | Rapid | Movement limited through pore space |
| | Minimal NP waste | Must directly quantify NPs |
| Dye Adsorption | Do not have to directly quantify NPs | Difficult to interpret if no adsorption |
| | Suitable for NPs that agglomerate | Charged probes contribute to adsorption |
| | Does not require extensive range finding | Octanol is not reference phase |
| | Can be applied in natural systems | |

to across NP materials and potentially to suspensions in complex environments. The octanol water partitioning method is only suitable for select particles that are small, stable and easily quantified and strongly suggest against future applications with NPs. HIC is theoretically suitable for future use with NPs, but would require thorough optimization of a reference column for wide application, and it is unlikely a single column could evaluate wide classes of NPs. The dye adsorption method is rapid and can be readily implemented to assess the hydrophobicity of broad classes of NPs, with the ultimate objective of application in future predictive fate models.

## 3.6 Conflict of Interest

There are no conflicts of interest to declare.

## 3.7 Acknowledgements

The authors thank Macklin Turnquist, Kristen Lum, Zia Klocke, and Shannon Quinn for assistance with data collection.

# 4 Abiotic assays to evaluate the reactivity of nanoparticles: comparisons, trends and applicability

Lauren E. Crandon, Kala M. Kopecek, Zheng Zhou and Stacey L. Harper

## 4.1 Abstract

As nanomaterial production and complexity increases, there is a need to rapidly assess relevant parameters to prioritize hazard testing and ultimately predict behavior upon release into the environment. A quantitative measure of redox behavior is needed to inform the design of catalytic nanomaterials and to model potential toxic interactions. Experimentally determined values for redox potential are typically carried out with an electrode, but studies have shown this method cannot be used for nanomaterials. In this study, we propose the use of methylene blue (MB) as a colorimetric probe to quantify the catalytic redox behavior of NPs. The reduction of MB by sodium borohydride was catalyzed by NPs, and the reaction was fit to a first order kinetic model and used as a metric of redox potential. We compared this method with existing abiotic methods to evaluate reactive oxygen species (ROS) production (dichlorofluorescein diacetate, DCFH-DA) and antioxidant capacity (Trolox Equivalent Antioxidant Capacity, TEAC) of NPs to determine relationships and trends based on methodology used and NP properties. We applied the three methods across a series of lanthanide oxide NPs (Ce, Nd, Er, Sm, Gd, Ho, Eu). We found that the three assays generally had similar elemental periodic trends across the LnOx series when normalized by NP surface area. The assays were further compared in terms of wide applicability, ease of use and interpretation of results. The MB method is suitable to determine relative redox behavior of NPs within a given range of reduction potentials. However, studies which aim to directly predict toxicity by a known mechanism may also choose to perform DCFH or TEAC, which report results in terms of a biologically relevant equivalent.

## 4.2 Introduction

Nanoparticles (NPs) are widely used in a variety of industrial and consumer products for cosmetic, agriculture, medical and energy applications [92]. NP use in consumer and industrial markets has a projected yearly global increase of approximately 20% [20]. Nano-enabled technology for a diversity of applications has led to the development of novel NPs, which can be composed of a wide variety of materials, including composites and alloys, with various sizes, morphology, and surface functionalization [28, 44, 67, 125, 157]. Despite the growth of nanotechnology, information is limited regarding the potential risk of NPs throughout their life cycle.

A number of *in vitro* and *in vivo* testing models have demonstrated the toxicity of some NPs [68, 183, 184]. Comprehensive screening of all NPs using conventional toxicity testing is cost prohibitive, and as NP production and complexity increases, there is a need to rapidly assess relevant parameters to move toward predictive models of NP behavior upon release into the environment. Several paradigms have been proposed as predictive measures of toxicity with the most widely assessed being band gap and dissolution. However, these descriptors are specific to certain NP compositions (metal/metal oxides) and may not be relevant in complex biological systems [144].

The redox behavior of NPs is a more general and useful measure to describe surface reactivity, and has implications for risk assessment and NP applications. Redox potential is important for comprehensive physicochemical characterization of broad classes of NPs as it has been shown to influence toxicity and potentially disrupt normal biological redox processes [14, 15, 148]. As particle size decreases to the nanometer range, the physical and chemical properties, including redox, of some materials differ from those associated with their bulk form [51]. The redox properties of some NPs combined with a high sur-

face area to volume ratio makes them ideal for applications in heterogeneous catalysis [28, 44, 67, 125, 157] and promising in therapeutics as antioxidants [56, 64, 141]. However, nano-specific behavior presents additional challenges in obtaining useful measurements needed to understand the influence of nanomaterials on natural redox processes should they be released into the environment [196].

Currently there is no standard method to determine the redox potential of NPs. Approaches that are commonly used to measure the redox of dissolved species are not suitable for NPs [162, 184]. The Organization for Economic Cooperation and Development (OECD) evaluated the testing guidelines for two standard methods, potentiometry and OxoDish $O_2$-detection, using $CeO_2$, $SiO_2$, and ZnO NPs and deemed both methods unsuitable for application with NPs [148, 196]. Potentiometry, the most widely used method which uses an oxidation-reduction probe (ORP) to measure electrochemical potential, produced results that were dominated by solution conditions as opposed to the NPs themselves, and a stable equilibrium between NPs and the probe surface could not be achieved. Evaluation of $O_2$-detection determined that dissolved oxygen does not conclusively correlate with redox potential for all NPs.

Due to high surface reactivity of some NPs, reactive oxygen species (ROS) or reactive nitrogen species (RNS) can be generated at or near the surface of cells, or once taken up into the cell [214]. Although ROS is used in normal cell signaling processes, an excess of ROS/RNS can overwhelm antioxidant capacities of cells and induce damage to proteins, lipids and DNA [180, 205]. This phenomenon, known as oxidative stress, has been recognized as the general mechanism of toxicity of many NPs [140].

Various probes are used to detect specific species of ROS in abiotic or biotic conditions (Table 4.1). Abiotic assays quantify ROS generation by NPs in

a given medium, typically a buffer solution. Based on the selection of the probe, interaction with a certain species of ROS can be detected by absorbance or fluorescence, making these methods inexpensive, rapid, simple, and easily standardized across labs for initial screening. Due to the complex nature of ROS mediated cellular redox signaling, abiotic assays may not be easily extrapolated to in vivo conditions [118]. For use of these methods in biotic conditions, a relevant cell line is selected, and the probe must first interact with and penetrate the cell membrane. Oxidation of the probe by intracellular ROS is observed and quantified by absorption, fluorescence spectroscopy, or flow cytometry. Assays performed in biotic conditions are generally more common, but results are difficult to directly compare across studies. Results can vary greatly, depending on specific cells used, cell culture conditions, affinity of a probe or NP for the membrane surface, NP concentrations, and cytotoxicity of NPs [73]. In addition, it is difficult to determine if ROS measured is directly generated from the NP surface, generated from disruption of cellular redox balance, or produced as a cellular response.

Abiotic versions of these assays have been applied to NPs to detect generation of ROS. For example, dithiothreitol (DTT), which detects superoxide, hydrogen peroxide, and hydroxyl radicals, was applied to a group of carbonaceous NPs and used as a metric of structural surface reactivity for groups of metal, metal oxide, and carbonaceous nanomaterials [179, 220]. 2,3-Bis-(2-Methoxy-4-Nitro-5-Sulfophenyl)-2H-Tetrazolium-5-Carboxanilide (XTT) has been used with metal oxide NPs to evaluate their ability to generate superoxide [73, 110].

2'7-dichlorodihydrofluorescein (DCFH) is among the most widely used probe, in part because it nonspecifically detects ROS generation and the assay is simple and inexpensive to perform [228]. However, when applied to nanomaterials, results vary widely across studies [151, 228]. This is likely due to the

lack of a standard methodology. Studies differ in buffering media used, reaction time, DCFH concentration, and use of the enzyme horseradish peroxidase (HRP) [151, 228]. HRP is thought to be necessary to catalyze the oxidation of DCFH and enhance fluorescence for detection, but interaction with HRP can either increase or decrease the catalytic ability of nanomaterials, depending on the species. HRP can also directly oxidize DCFH and has been shown to increase fluorescence of the DCFH control by 4-5 orders of magnitude, depending on the media used and sonication time [151]. In addition, autoxidation of DCFH controls can lead to apparent negative values of ROS generation by NPs.

The redox behavior of some NPs results in the ability to scavenge and reduce concentrations of free radicals, thereby preventing oxidative damage. Several assays have been employed to quantify antioxidant capacity (AOC) of NPs using either fluorescence or absorbance detection methods. The oxygen radical absorbance capacity (ORAC) assay has been applied to evaluate antioxidant capacities of nanomaterials such as selenium nanoparticles (nano$Se^0$)-ascorbic acid (Vc) sol and nano$Se^0$/Vc/selenocystine (SeCys) sol-gel compounds [18]. Terephthalic acid (TPA) was applied to evaluate the antioxidant capacity of palladium oxide nanoparticle modified electrodes and to evaluate the quantum yield of hydroxyl radical production during $TiO_2$ photocatalysis [79, 113]. The Trolox Equivalent Antioxidant Capacity Assay (TEAC) is a colorimetric method in which $OH^{\cdot}$ generated from the reaction between $H_2O_2$ and HRP oxidizes colorless $ABTS^{2-}$ to a long-lived green-blue radical anion $ABTS^{\cdot -}$. Following the addition of NP antioxidants, the decrease in absorbance is used to measure the antioxidant capacity. Results are converted to Trolox equivalent, a biologically relevant water-soluble Vitamin E analog. Because this assay has been widely used and applied in food science it is amenable to the assessment of complex matrixes, such as nanoparticle dispersions [11, 101]. Although antioxidant capacity

assays have been applied in some cases to NP, they have several limitations regarding broad applicability and sensitivity to variations in testing conditions (Table 1). In general, free radicals are short lived, so ROS and AOC assays are highly dependent on reaction time and protocol used.

Methylene blue has been used as a redox indicator in electrochemical DNA assays to detect hybridization events [58]. Its reduction potential lies in the range of many biomacromolecules so it has been used as an electron transfer mediator [217]. For application with NPs, MB is used as an indicator of photocatalytic ability [206]. In the presence of a reducing agent, MB has been applied in some studies to evaluate the effect of size and substrate loading the on catalytic ability of silver NPs [155, 213], assess the effect of a surfactant on the catalytic ability of palladium NPs [81], and to detect the presence of NPs in complex media [41]. The reduction of the colorimetric probe, methylene blue (MB), by sodium borohydride ($NaBH_4$) is thermodynamically but not kinetically favorable at ambient conditions and will therefore only occur in the presence of a catalyst. A successful catalyst has a redox potential intermediate of the reagents (-1.33 eV for $NaBH_4$ and -0.21 eV for MB) [81]. When NPs are used to catalyze this reaction, we propose that the rate of MB reduction is indicative of the reduction potential of the NP catalyst. Like the DCFH and TEAC methods, the MB probe can be easily and rapidly detected using spectrophotometry and will change from blue to colorless as the redox reaction proceeds.

In this study, the reduction of MB as a colorimetric indicator of NP redox behavior was modified and adapted for use as a high throughput functional assay. This method was applied to evaluate a series of lanthanide oxide (LnOx) NPs. Lanthanide metal oxides (LnOx) are widely used as the catalyst, support or substrate for catalysts [40, 153, 193, 227, 230], solar cells [39, 90, 106, 114], electromagnetism, electrochemistry [35, 227], fuel cells [49, 123, 233], phos-

TABLE 4.1: Summary of assays used to measure reactive oxygen species generation and antioxidant capacity of nanomaterials

| **ROS Generation** | | | |
|---|---|---|---|
| **Assay** | **Probe** | **ROS detected** | **Limitations** |
| ESR | Various spin trap agents | $OH^{\cdot}$ | Limited detection of ROS species, low availability of instrumentation, low temperature |
| DTT | DTT (absorbance) | $H_2O_2$, ${O_2}^{-2}$, $OH^{\cdot}$ | Time consuming; adsorption to NP surface, surfactant, concentration greatly influence results |
| XTT | XTT (absorbance) | ${O_2}^{-2}$, cell viability | Long incubation time, detects ${O_2}^{-2}$ only, NPs interfere with product absorbance readings |
| DCF | DCF (fluorescence) | $OH^{\cdot}$, $RO^{2\cdot}$, more radicals (total ROS) | Some NPs directly oxidize DCFH (instead of radicals), autoxidation |
| **Antioxidant capacity** | | | |
| **Assay** | **Probe** | **ROS quenched** | **Limitation** |
| ORAC | B-phycoerythrin or fluorescein (fluorescence) | peroxyl radical | Temperature sensitive , time consuming, difficult to calculate AOC |
| TPA | TPA (yields fluorescent 2-hydroxyterephthalic acid (HTPA)) | $OH^{\cdot}$ | Poor solubility in water |
| DPPH (absorbance) | $DPPH^{\cdot}$ (stable organic nitrogen radical) | $DPPH^{\cdot}$ (absorbance) | Hydrophobic, time consuming, steric hindrance to large antioxidant<br>Absorbance interference by NPs, DPPH probe not similar to biological, short lived radicals |
| DMPO | DMPO (spin trap agent) | $OH^{\cdot}$ | Side reactions , requires advanced (expensive) instrumentation (to measure EPR) |
| TEAC | $ABTS^{\cdot+}$ (absorbance) | $ABTS^{\cdot+}$ | $ABTS^{\cdot+}$ is a nonphysiological radical source, reaction time may vary |

phor/luminescence and laser materials [178], gas sensors [134, 143], metallurgical and glass/ceramic applications [57, 169, 182]. In addition to the diversity of applications of for this class of nanoparticles, LnOx NPs are of interest because studies have revealed evidence of toxicity. For instance, cerium dioxide NP ($CeO_2$NP) has been demonstrated to reduce cell viability in human bronchoalveolar carcinoma-derived cells [111]. Blaise and colleagues showed that samarium (III) oxide NP ($Sm_2O_3$ NP), erbium (III) oxide NP ($Er_2O_3$ NP), and holmium (III) oxide NP ($Ho_2O_3$ NP) exhibited toxicity across serveral taxonomic levels for aquatic and sediment species [24]. Harper *et al.* demonstrated toxicity of $Ho_2O_3$, $Er_2O_3$, and $Sm_2O_3$ NPs in zebrafish embryos [69].

In this study, we propose a methylene blue assay as a rapid, robust and systematic method to determine the relative redox potential of NPs. Unlike previous approaches to characterize NP reactivity by ability to produce or quench various species of ROS, we suggest that this assay directly characterizes redox behavior and can potentially be used across classes of nanomaterials (not just metal oxides). This method was compared with a modified DCFH assay to evaluate reactive oxygen species (ROS) production, and the TEAC $ABTS^{2-}/H_2O_2$/HRP decoloration assay as a measure of antioxidant capacity. DCFH and TEAC were selected based on their widespread use, simplicity, sensitivity of the probes and potential to be applied to a wide variety of NP compositions. All three assays were performed in abiotic conditions and applied across a series of lanthanide oxide (LnOx) NPs. The crystal structure, d orbital electron configuration, stoichiometry, primary particle size, and limited solubility of metal ions are mostly the same across the series, so comparing reactivity allows for systematic comparison of gradual periodic trends. It was hypothesized that the redox activity of the lanthanide oxide nanoparticles will be related to their intrinsic properties and be a function of elemental periodicity.

## 4.3 Experimental

### 4.3.1 Nanoparticle preparation and characterization

Seven lanthanide oxide nanoparticles (LnOx NPs) were purchased from Sigma Aldrich (St. Louis, MO): cerium oxide ($CeO_2$), neodymium oxide ($Nd_2O_3$), samarium oxide ($Sm_2O_3$), europium oxide ($Eu_2O_3$), gadolinium oxide ($Gd_2O_3$), holmium oxide ($Ho_2O_3$), and erbium oxide ($Er_2O_3$). All metal oxides were purchased as a nanopowder with a primary particle size $< 100$ nm. A 1000 mg/L aqueous stock solution was prepared for each LnOx NP and ultrasonicated for 2 minutes at 40% amplitude using a 750 watt Vibra Cell ultrasonicator (40.1 W) with a cup horn configuration and a circulating bath to minimize temperature increase (Sonics & Materials Inc., Newtown, CT). Dynamic light scattering was performed on a 100 mg/L suspension of each LnOx NP diluted in the respective buffer solution (HEPES for methylene blue, 0.1x PBS for DCF and TEAC). A Zetasizer (ZEN3600, Malvern Instruments, Westborough, MA) was used to measure hydrodynamic diameter (HDD) and zeta potential (ZP) at 25°C. Assuming spherical geometry for the LnOx NPs and that the suspensions were monodisperse, HDD was converted to surface area using the density of each material.

### 4.3.2 Methylene blue catalytic reactivity assay

The methylene blue assay was adapted from Corredor *et al.* and modified to be performed in a 96-well plate for high throughput data collection, as described below [41]. MB was selected because its oxidized form is blue and as it is reduced to leucomethylene blue (LMB) the solution becomes colorless and the rate of reduction can be measured spectrophotometrically (Fig 4.1).

Reagent stock solutions were prepared in Milli-Q ultrapure water (MQ) and placed in a 96-well plate (final working volume in each well = 200$\mu$L) with

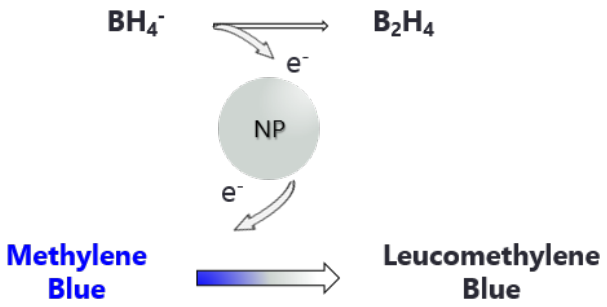


FIGURE 4.1: Reaction scheme of methylene blue reactivity assay.

final concentrations of 0.04 mM MB, 10 mM N-(2-hydroxy- ethyl) piperazine-N'-(2-ethanesulfonic acid) (HEPES) buffer solution, 1.5 mM sodium hydroxide (NaOH), and 10 mM $NaBH_4$. The $NaBH_4$ stock solution was prepared in ice water to slow down and therefore limit reaction with water. MB, HEPES, NaOH, and $NaBH_4$ were first mixed in each well of the 96 well plate. LnOx NP suspensions were added last with a final concentration of 250 mg/L. This concentration was selected for limited absorption interference, rapid kinetics, minimal mass transfer limitations between reactants, and to limit settling of NPs during the reaction time. Following the addition of the LnOx NP catalyst the absorbance of each well was measured in a SpectraMax spectrophotometer at a wavelength of 665 nm every 30 seconds for 90 minutes. The plate was agitated between readings for 3 seconds to reduce the interference of bubbles produced by $NaBH_4$. Control wells without LnOx NPs were prepared to account for any uncatalyzed reduction of MB by $NaBH_4$. The absorbance interference of the LnOx NPs was also measured over time and subtracted. The reduction of MB to LMB over time was fit to a 3 parameter first order exponential decay:

$$A(t) = A_0\, e^{-kt} + \beta \tag{4.1}$$

where $A(t)$ is the absorbance at time $t$, $k$ is the first order reaction rate constant ($min^{-1}$), $\beta$ is the final asymptotic absorbance value, and $A_0$ is the difference between the initial absorbance and $\beta$. Adsorption of MB to the LnOx NP surface was evaluated by allowing 250 mg/L LnOx NP incubate at room temperature with 0.04 mM MB (no $NaBH_4$) for 90 minutes. The NPs were removed by centrifugation (14000 rpm, 30 minutes) and the concentration of MB in the supernatant was evaluated by UV-Vis ($\lambda$ = 665 nm).

### 4.3.3 Abiotic dichlorofluorescein assay

Dichlorofluorescein diacetate (DCFH-DA) was purchased from Millipore (Burlington, MA) and a 1 mM stock solution was prepared in 95% ethanol. DCFH-DA was chemically hydrolyzed to DCFH with 0.01 N NaOH in the dark at room temperature for 30 minutes (Fig 4.2). A volume of 55 $\mu$L of this mixture was added to each well of a black 96-well plate. LnOx NPs (145 $\mu$L) suspended in 0.1x PBS were added to each well for final concentrations of 50, 100, and 250 mg/L. The assay was performed at 25°C instead of the standard 37°C to allow for direct comparison with the MB assay. A temperature of 37°C is standard for biotic assays involving cell lines but is not required in the absence of cells. Fluorescence was measured every 5 minutes for 90 minutes at an excitation wavelength of 485 and emission wavelength of 530 nm. The fluorescence was converted to $H_2O_2$ equivalent for biological relevance using a standard curve of DCFH and $H_2O_2$ (0-125 $\mu$M). Control wells of DCFH and 0.1x PBS were prepared to account for autoxidation of DCFH to DCF. Horseradish peroxidase (HRP) was not added to the reaction because it has been shown to be

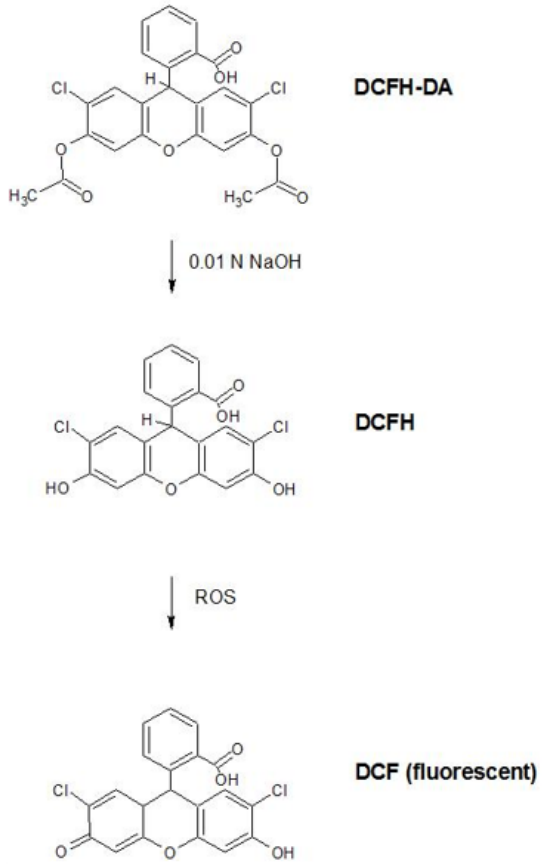


FIGURE 4.2: Schematic of the abiotic DCF assay. 2',7'-Dichlorofluorescein diaceteate (non-fluorescent) is chemically hydrolyzed with 0.01 N NaOH. DCFH (non-fluorescent) is oxidized by ROS and forms the fluorescent product, DCF.

unnecessary to catalyze the oxidation of DCFH and could interfere with results by directly oxidizing DCFH or become deactivated by certain metals [151]. The reaction was evaluated over 90 minutes to allow for direct comparison to the MB assay.

The DCFH assay was performed at 50, 100, and 250 mg/L for each LnOx NP. A linear regression was performed to determine if there was concentration dependent ROS generation.

### 4.3.4 Trolox equivalent antioxidant capacity assay

A 1 mL ABTS radical ($ABTS^{\bullet-}$) working solution was comprised of 1 mM $ABTS^{2-}$, 51 $\mu$M $H_2O_2$, 4 U/ml HRP, and 50 mM PBS (pH = 7.45). Temperature was held constant at 26 °C. The working solution was combined with LnOx NPs for a final concentration of 40 mg/L in each well of a 96 well plate. The decrease in absorption at 8 minutes was evaluated using UV-Visible spectroscopy (SpectraMax) at a wavelength of 734 nm. A calibration curve of a series of Trolox concentrations (0 - 25 $\mu$M) vs. $ABTS^{\bullet-}$ working solution was made to determine the relationship between absorption and an equivalent concentration of Trolox, a water soluble Vitamin E analog. The antioxidant activity of LnOx NPs is presented as AOC per unit surface area. All experiments were performed in triplicate.

### 4.3.5 Principle component and correlation analyses

Compositional and structural properties of lanthanide oxide and elemental lanthanide metals were collected from literature sources (Table C1). Values were scaled between 0 and 1 by mean centering and normalizing by the maximum and minimum. Principle component analysis was performed on the properties to identify how LnOx NPs cluster. The contribution of properties was determined for the first two principle components.

### 4.3.6 Statistics

SigmaPlot version 13.0 (Systat Software, San Jose, CA, USA) was used to perform all statistical analyses. All experiments were performed in triplicate. Differences in reactivity among LnOx NPs in each assay were compared using analysis of variance (ANOVA) with Tukey post-hoc analysis. Differences were considered statistically significant when $p \leq 0.05$. Error bars represent standard

error of the mean. Linear regression was performed to create a standard curve of $H_2O_2$ equivalent (DCFH assay) or Trolox equivalent (TEAC). The decrease in absorbance of MB as a function of time was fit to a first order exponential decay model for the MB assay using the curve fitting function in SigmaPlot.

## 4.4 Results

LnOx NPs had large agglomerates in both media, and the average HDD in 0.1x PBS was higher than in HEPES (Fig 4.3). $CeO_2$ had a much smaller HDD than the rest of the LnOx series when suspended in 0.1x PBS but not in HEPES. The polydisperisity index (PDI) values ranged from 0.36 ($Nd_2O_3$) to 0.62 ($Er_2O_3$).

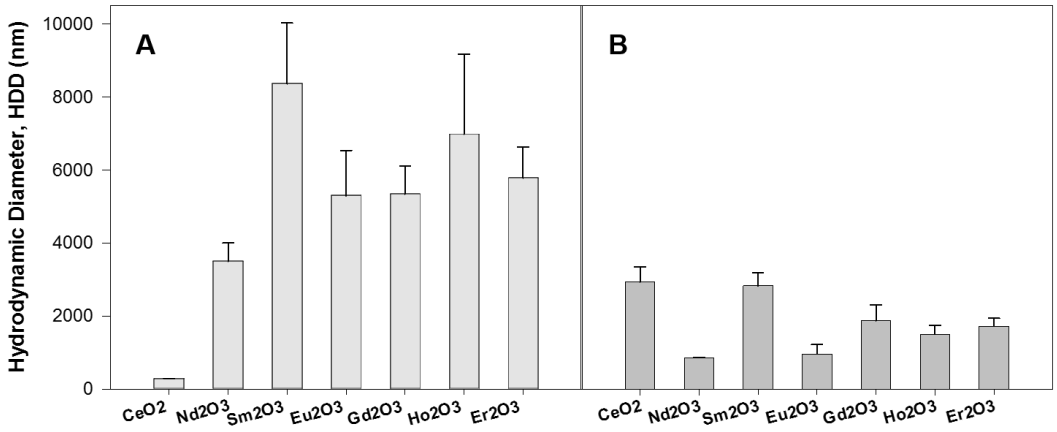


FIGURE 4.3: Hydrodynamic diameter (nm) of 100 mg/L LnOx NPs in A) 0.1x PBS and B) HEPES buffer. LnOx NPs are shown in order of increasing periodicity.

All seven LnOx NPs used in this study catalyzed the reduction of MB by $NaBH_4$, resulting in a decrease in absorbance over time (Fig 4.4). The variance in absorbance readings increased over time due to an increased production in hydrogen bubbles by reaction of $NaBH_4$ with water. The rate constants from Eq. 4.1 are plotted for each LnOx NP in Fig 4.5 and shown in order of increasing atomic number, which shows that catalytic reactivity did not correlate with periodicity. $Sm_2O_3$ did not have a good fit with the model and therefore has a high variance.

The slope of fluorescence over time was converted to ROS production in

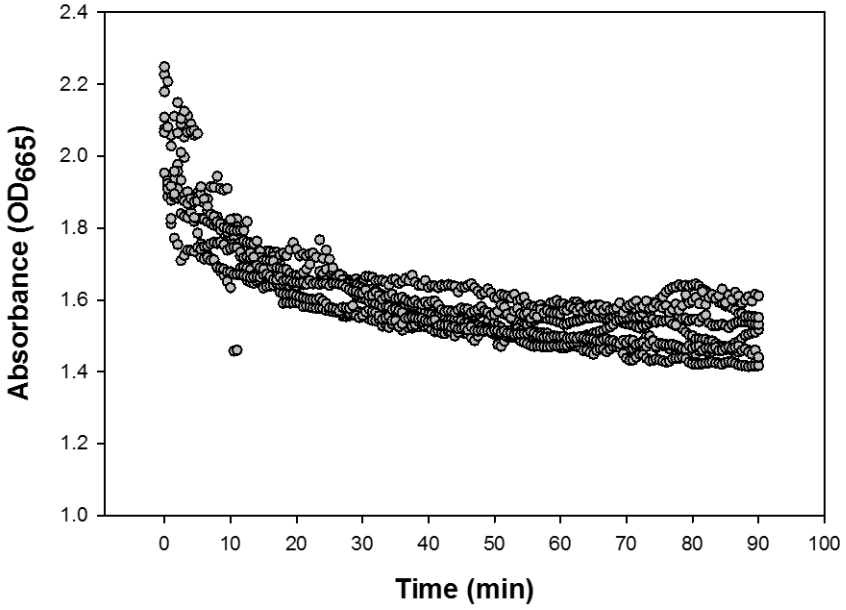


FIGURE 4.4: Decrease in absorbance at $\lambda = 665$ nm over time from the reduction of MB by $NaBH_4$ catalyzed by 250 mg/L $Nd_2O_3$.

units of $\mu$M $H_2O_2$ equivalent. A linear standard curve of $H_2O_2$ concentration (0-125 $\mu$M) vs. fluorescence (RFU/min) was generated for each experiment ($R^2 = 0.98$). Although horseradish peroxidase was not used, DCFH was able to detect ROS generated by $H_2O_2$ upon interaction with PBS. The ROS produced by 250 mg/L LnOx NPs is shown in Fig 4.5 and normalized by surface area. $Er_2O_3$ had the highest production of ROS per surface area and $CeO_2$ had the lowest. The DCFH assay also showed a concentration dependent increase in ROS generation for all LnOx NPs testing (Fig S2).

The antioxidant capacity of LnOx NPs was measured by detecting the decrease in absorption relative to control (no NPs), which detects the reduction of $ABTS^{\bullet-}$ to $ABTS^{2-}$. After 8 minutes of reaction time, $Sm_2O_3$ had the highest AOC (101 $\mu$m Trolox/$cm^2$) and $CeO_2$ had the lowest AOC (22 $\mu$m Trolox/$cm^2$)

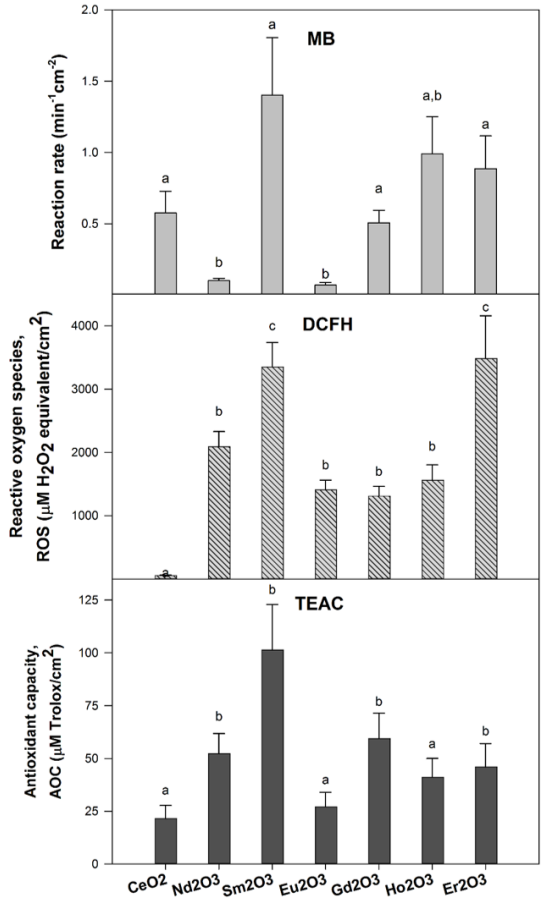


FIGURE 4.5: Reduction rate of MB catalyzed by 250 mg/L LnOx NPs, concentration of ROS ($\mu$M $H_2O_2$ equivalent) generated by 250 mg/L LnOx NPs measured using DCFH, and AOC determined by TEAC (40 mg /L LnOx) shown in order of increasing periodicity. a, b and c represent significance differences among LnOx NPs ($p < 0.05$, one-way ANOVA, Tukey post-hoc). All measurements were normalized by NP surface area.

(Fig 4.4). Absorbance by the LnOx NPs in PBS at 734 nm was subtracted from the results.

The results for all three abiotic assays were normalized by surface area. The three assays reflect similar trends when plotted by elemental periodicity of the Ln metal (Fig 4.6). A Pearson correlation ($p < 0.05$) revealed a correlation between the normalized results of MB and TEAC. When $Er_2O_3$ is excluded from

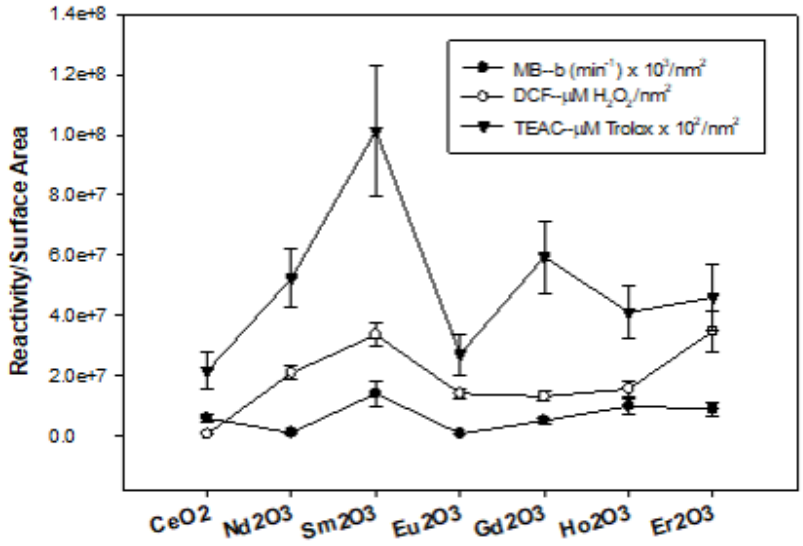


FIGURE 4.6: Reaction rate constant for the reduction of MB, ROS generation, and antioxidant capacity normalized by surface area in order of elemental periodicity.

analysis, all three assays have a positive correlation.

Principle component analysis performed on scaled structural and compositional properties of Ln and LnOx was performed and PC1 and PC2 captured approximately 82% of the variation (Fig 4.7). $CeO_2$ and $Gd_2O_3$ clustered separately from the other Ln/LnOx materials. A component loading analysis of PC1 and PC2 revealed that band bap had a high contribution.

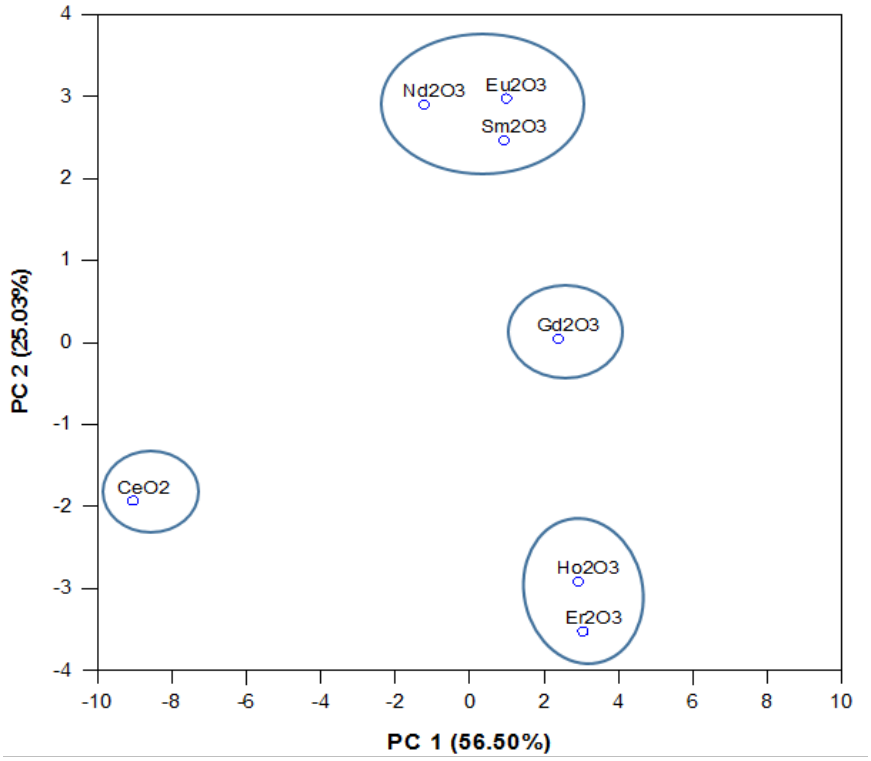


FIGURE 4.7: Plot of first and second component from principle component analysis performed using compositional and structural properties of Ln and LnOx.

## 4.5 Discussion

This study evaluated a potential method to determine the redox potential of NPs and compared it to existing methods to quantify ROS production and antioxidant capacity. We applied three methods: a MB colorimetric assay, the abiotic DCFH fluorescence assay, and the TEAC colorimetric assay across a series of seven lanthanide oxide NPs and observed a correlation between catalytic reactivity, ROS production, and AOC. Our findings suggest that the MB assay is suitable to describe the redox behavior of nanomaterials.

The MB colorimetric assay, which has previously been used to evaluate catalytic behavior of metal NPs, was applied here to characterize the redox

potential of LnOx NPs [155, 213, 231]. The reduction of the methylene blue probe indicates that the redox potential of a NP catalyst lies between the redox potential of the probe and the reducing agent (between -1.33 and -0.21 eV) [81]. In this study, the seven LnOx NPs successfully catalyzed the reaction, suggesting their redox potentials were all in this range. However, this assay would not inform studies of nanomaterials with a redox potential outside this range, which may limit broad applicability.

The MB redox method was rapid and inexpensive to perform. The colorimetric probe allowed for the direct measurement of absorbance by spectrophotometry which is widely available. However, there were some aspects that led to high variance in our data. The production of hydrogen gas bubbles in the wells by the hydrolysis of $NaBH_4$ created interference in absorbance measurements [181]. NP settling likely occurred during the 90-minute reaction time. A surfactant was not used to stabilize the NP suspensions because it has been shown to affect surface reactivity [83]. Similar to previous observations using colorimetric assays, absorbance of NPs showed some interference, although controls revealed that this was minimal for LnOx at the wavelength used [99]. Additionally, the reaction catalyzed by $Sm_2O_3$ did not fit the exponential decay model well and it is possible alternative models may be required for NPs with different compositions, which would make comparison across classes of nanomaterials difficult.

The low adsorbance of MB to the LnOx NP surface indicates that differences in affinity of dye to the NP surface did not contribute to reactivity differences observed (Fig. C.3). This may also explain the relatively slow reaction rate catalyzed by LnOx NPs. The low affinity of reagents to the surface of the catalyst did not provide a surface to maximize interaction between MB and $NaBH_4$.

The abiotic dichlorofluorescein assay was selected here to evaluate ROS

production of LnOx NPs because it nonspecifically detects species of ROS. The method was adapted to overcome limitations observed by previous studies [105, 151]. There was a linear concentration dependent generation of ROS by LnOx NPs in the range evaluated here, but previous studies have found a lack of dose response [151]. This might be attributed to the negligible dissolution of LnOx NPs. The dissolution of metal ions can lead to the generation of ROS and affect DCF results. For other classes of nanomaterials, the assay would have to be optimized across a range of concentrations to understand this relationship.

To evaluate antioxidant capacity of LnOx NPs, the TEAC assay was selected, which has been most commonly applied in food science. Although this method was simple to perform, NPs have the ability to stabilize free radicals and form a metastable complexation of LnOx-$ABTS^{\bullet-}$, leading to an underestimate of AOC [235]. Absorbance interference of the NPs restricted the range of concentrations that could successfully be evaluated, but the reaction time was shorter than the MB assay, so settling of NPs out of suspension was less likely to alter results.

The three abiotic assays tested here across seven LnOx NPs utilized different chemical probes to quantify reactivity in aqueous systems. The elemental periodic trends among the LnOx NPs was similar for the MB, DCFH, and TEAC assays when normalized by NP surface area. The ability of NPs to produce and quench ROS is generally attributed to the catalytic ability of the NP surface, dissolution of metal ions, and adsorption/desorption of biomolecules onto the surface [205]. Since LnOx NPs have negligible dissolution and the assays here were performed in abiotic conditions, the catalytic potency of the NP surface is the predominant mechanism for ROS production and scavenging behavior. This suggests that catalytic electron transfer observed by the MB assay might also lead to the generation of ROS upon interaction with the reaction media. A

previous study also observed a correlation between ROS generation measured with DCFH and catalytic activity of Pd and Ni NPs [142].

In all three assays, $CeO_2$ NPs had low observed reactivity, despite being recognized as a good scavenger for ROS [88]. Unlike the other six LnOx studied here which are present as sesquioxides, $CeO_2$ is found mostly in the +4 oxidation state, and can alternate between +3 and +4 oxidation states. This dynamic change in oxidation state causes oxygen vacancies that are associated with the redox activity of $CeO_2$ [33, 141]. It is possible that $CeO_2$ NPs produce and quench ROS at the surface without being detected by DCFH or ABTS probes. Alternatively, $Ce_2O_3$ makes up a small fraction of the Ce based NPs here and may be the only active component.

The three abiotic assays evaluated in this study showed similar periodic trends across a series of LnOx NPs. However, catalytic activity, ROS production, and AOC were found to not be a function of elemental periodicity. Previous studies which evaluated the rate at which bulk sized LnOx catalyzed the degradation of various hydrocarbons and other reactions also found that despite have the same d-orbital electron configuration and similar crystal structure, periodicity alone did not explain differences in catalytic ability [25, 175]. Depending on the reaction, paramagnetic properties, lattice oxygen mobility, and variable valence of the metal cation have been suggested to play an important role in governing redox behavior [175]. PCA analysis of Ln metal and metal oxide properties in this study revealed $CeO_2$ clustered separately from the other LnOx NPs based on compositional and structural properties (Fig 4.7). This is consistent with the low rate of MB reduction catalyzed by $CeO_2$, ROS production, and AOC. $Gd_2O_3$ also clustered separately from the rest of the LnOx series. $Gd_2O_3$ had a relatively high AOC as observed in the TEAC assay, but did not directly correlate with the other two assays. A component loading analysis of PC1 and

PC2 revealed that band bap had a high contribution. $Gd_2O_3$ had the highest band gap energy (5.4 eV) and $CeO_2$ had the lowest band gap energy (2.4 eV). This suggests that band gap energy is most relevant for comparison with AOC, but other parameters may dominate for MB and DCF assays. Properties compiled for analysis mostly described the bulk materials, with the exception of HDD (Table S1). Most of the properties fall within a narrow range and have structural similarities due to proximity on the periodic table and similar electron configuration and oxidation state. Materials with a larger range of properties should be evaluated before extrapolating trends to other nanomaterials.

Although the three methods showed correlations along the LnOx NP series when applied broadly across nanomaterials there are certain characteristics that might make one method more suitable over the others (Table 4.2). The results of the DCFH and TEAC assays are reported in terms of a biologically relevant equivalent, $H_2O_2$ and Trolox, respectively, which is useful when considering specific mechanisms of toxicity. The MB assay, on the other hand, reports reactivity in terms of reduction rate of the probe and is not converted to a standard equivalent, so the results provide a more relative measure. Another consideration is the ability to perform these assays in complex media to evaluate the effect of environmental or biological transformations on NP reactivity. The MB assay has been performed with NPs in natural waters and biological media [41]. The TEAC assay has been widely used and conducted to assess complex food matrixes [11, 101], so we believe it is amenable to assess NPs in complex media. However, the DCFH has typically been performed in a standard buffer solution, and complex media components could artificially alter results by quenching ROS or contributing to ROS production.

We adapted all three assays here to accommodate a 96-well plate to facilitate rapid data collection and allow for simultaneous comparison across several

TABLE 4.2: Advantages and limitations of three reactivity assays

| | MB | DCF | TEAC |
|---|---|---|---|
| **Advantages** | | | |
| Biologically relevant equivalent | | ✓ | ✓ |
| Can be applied in complex media | ✓ | | ✓ |
| Measures absorbance | ✓ | | ✓ |
| Measures fluorescence | | ✓ | |
| Stable probe | ✓ | | |
| 96-well plate | ✓ | ✓ | ✓ |
| **Limitations** | | | |
| NP settling interference | ✓ | | ✓ |
| Fluorescence interference | | ✓ | |
| Temperature sensitive | | ✓ | |
| Requires HRP | | | ✓ |

materials. Differences in materials and methods of each individual assay still contribute to cost and time considerations. MB is a stable probe that can be stored relatively long term at room temperature whereas DCFH and ABTS must be stored at -4 °C. ABTS radicals must be generated the day of the experiment for the TEAC assay and $NaBH_4$ must be prepared daily for the MB assay. Fluorescence interference of DCF from neighboring wells on a 96-well plate was a concern in this study and specific plates must be used to limit this. However, unlike MB and TEAC assays, settling and absorbance interference of NPs minimally impacts the results. HRP is required to generate ROS in the TEAC assay, but it can directly interact with NPs and the probe itself and alter results.

## 4.6 Conclusion

Understanding the redox potential of nanomaterials is vital to inform the responsible design of nanomaterials as they continue to become integrated into consumer products and industry. This study evaluated a simple and rapid

method to determine the redox potential of NPs using a colorimetric abiotic assay. This approach has the potential to be widely applied across nanomaterials, including those with surface ligands and in complex environments. The MB reactivity assay was applied in this study across a series of LnOx NPs and the correlated with the abiotic DCFH and TEAC assays. This provides a better understanding of how electron transfer at the NP surface can result in the generation and quenching of ROS. Additionally, this correlation suggests that existing data from ROS production and antioxidant capacity assays can be used to inform redox behavior of NPs. Unlike previous methods, however, the MB assay likely encompasses all redox behaviors, such as dissolution and complexing with environmental constituents, which may be more directly applicable to model environmental behavior of NPs.

## 4.7 Acknowledgements

Thanks to Arek Engstrom for his work on the abiotic DCFH ROS assay.

# 5 Conclusion

The findings in this dissertation address challenges associated with NP evaluation. As NP production and complexity continues to grow, reliable frameworks for risk assessment are necessary for the responsible development of nanomaterials. This dissertation presents promising methods that, if widely implemented, will help facilitate reproducible and robust data collection for future predictive fate and toxicity models.

Current practices for NP stock preparation were reviewed in Chapter 2 and found that despite many published protocols to standardize dispersion preparation, significant discrepancies exist in sonication procedures and reporting in nanotoxicology studies. Some of the discrepancy was due to the diversity of available instrumentation. Calorimetric calibration which normalized for the surface area of the sonicator probe was used to deliver equal sonication energy and therefore produce similar NP dispersions using three sonicator configurations and different power inputs. This technique should be routinely applied in addition to reporting associated sonication metadata to improve compliance with existing standard methods and significantly increase reproducibility in toxicity studies.

Chapters 3 and 4 address clear data gaps that have been identified for comprehensive NP characterization. In chapter 3, previous attempts to measure hydrophobicity of nanomaterial were reviewed. When compared to methods designed for solids (contact angle) and chemicals (octanol-water partitioning), we conclude that the dye adsorption assay is the best in terms of ability to overcome difficulties associated with agglomeration, functionalization, and quantification of nanomaterials, and can likely be widely applied to across NP materials and potentially to suspensions in complex environments. However, alternative dyes

should be explored to understand the contribution of electrostatic interaction to observed dye adsorption. HIC had significant shortcomings for broad application, but future studies may perform further optimization for small, stable particles. Hydrophobicity is a critical descriptor to describe environmental fate and bioavailability. Although the dyes used for adsorption studies do not necessarily have environmental significance, they can be used as a reference phase to obtain relative measures across suites of materials in a similar framework to chemicals.

In chapter 4, a method to measure the relative redox potential of NPs was evaluated using LnOx NPs. Results from the MB assay were compared to ROS generation and AOC. It is generally understood that redox behavior at the NP surface is responsible for in situ ROS generation and subsequent oxidative stress. However, the short-lived nature of free radicals and quenching ability of the media and NP themselves makes it difficult to determine inherent redox behavior of NPs by measuring one or more species of ROS. This study confirmed a positive correlation between catalytic redox behavior, ROS generation, and AOC, across the LnOx NP series. However, further studies should be conducted to include NPs with dissolution and functional groups. Additionally, the LnOx NPs behaved similarly and this assay should be validated to include NPs with different oxidation states and reactivity. Ultimately, this method is promising for obtaining a relative quantitative measure of inherent redox potential at the NP surface. Unlike band gap and dissolution paradigms which only apply to select materials, the MB assay can be widely applied to materials with a reduction potential in the range of the reagents.

Overall, the methods shown here were developed with the objective of utilizing common laboratory instrumentation, simple techniques, and inexpensive reagents. Although more advanced instrumentation might provide better reso-

lutions for characterization, the aim here was to provide a basis for widespread data collection. In addition, the functional assays presented here evaluate NP properties in situ. NP behavior has shown to be strongly dependent on the local environment. While environmentally relevant systems were not used in this dissertation, the methods presented can potentially be applied in complex systems and future studies should focus on incorporating the effects of environmental transformations at the NP surface on observed hydrophobicity and redox. The approaches shown here will contribute to robust NP characterization that is ultimately needed for predictive fate and toxicity models for sustainable nanotechnology development.

# 6 Bibliography

## Bibliography


1. N. Adam, A. Vakurov, D. Knapen, and R. Blust. The chronic toxicity of CuO nanoparticles and copper salt to Daphnia magna. *Journal of Hazardous Materials*, 283:416–422, 2015.

2. P. Aggarwal, J. B. Hall, C. B. McLeland, M. A. Dobrovolskaia, and S. E. McNeil. Nanoparticle interaction with plasma proteins as it relates to particle biodistribution, biocompatibility and therapeutic efficacy. *Advanced Drug Delivery Reviews*, 61(6):428–437, 2009.

3. M. Ahamed. Toxic response of nickel nanoparticles in human lung epithelial A549 cells. *Toxicology in Vitro*, 25(4):930–936, 2011.

4. M. Ahamed, M. J. Akhtar, M. A. Siddiqui, J. Ahmad, J. Musarrat, A. A. Al-Khedhairy, M. S. AlSalhi, and S. A. Alrokayan. Oxidative stress mediated apoptosis induced by nickel ferrite nanoparticles in cultured A549 cells. *Toxicology*, 283(2-3):101–108, 2011.

5. J. Ahmad, M. Ahamed, M. J. Akhtar, S. A. Alrokayan, M. A. Siddiqui, J. Musarrat, and A. A. Al-Khedhairy. Apoptosis induction by silica nanoparticles mediated through reactive oxygen species in human liver cell line HepG2. *Toxicology and Applied Pharmacology*, 259(2):160–168, 2012.

6. N. Akaighe, S. W. Depner, S. Banerjee, V. K. Sharma, and M. Sohn. The effects of monovalent and divalent cations on the stability of silver nanoparticles formed from direct reduction of silver ions by Suwannee River humic acid/natural organic matter. *Science of the Total Environment*, 441:277–289, 2012.

7. B. Aksoy and B. Yarar. Natural hydrophobicity of native gold flakes and their flotation under different conditions. In G. Dobby and S. Rao, editors, *Proceedings of the International Symposium on Processing of Complex Ores*, pages 19–27, Halifax, 1989.

8. H. J. Allen, C. A. Impellitteri, D. A. Macke, J. L. Heckman, H. C. Poynton, J. M. Lazorchak, S. Govindaswamy, D. L. Roose, and M. N. Nadagouda. Effects from filtration, capping agents, and presence/absence of food on

the toxicity of silver nanoparticles to Daphnia magna. *Environmental Toxicology and Chemistry*, 29(12):2742–2750, 2010.

9. P. J. J. Alvarez, V. Colvin, J. Lead, and V. Stone. Research priorities to advance eco-responsible nanotechnology. *ACS Nano*, 3(7), 2009.

10. C. P. Andersen, G. King, M. Plocher, M. Storm, L. R. Pokhrel, M. G. Johnson, and P. T. Rygiewicz. Germination and early plant development of ten plant species exposed to titanium dioxide and cerium oxide nanoparticles. *Environmental Toxicology and Chemistry*, 35(9):2223–2229, 2016.

11. C. A. &. A. M. Arnao, M. The hidrophilic and lipophilic contribution to total antioxidant activity. *Food Chemistry*, 73(2):239–244, 2001.

12. L. N. Arnaudov, O. J. Cayre, A. C. Stuart, D. Stoyanov, M. A. C. Stuart, S. D. Stoyanov, and V. N. Paunov. Measuring the three-phase contact angle of nanoparticles at fluid interfaces. *Physical Chemistry Chemical Physics*, 12(2):328–331, 2010.

13. S. Asghari, S. A. Johari, J. H. Lee, Y. S. Kim, Y. B. Jeon, H. J. Choi, M. C. Moon, and I. J. Yu. Toxicity of various silver nanoparticles compared to silver ions in Daphnia magna. *Journal of Nanobiotechnology*, 10(1):14, 2012.

14. M. Auffan, W. Achouak, J. Rose, M.-a. Roncato, C. Chane, D. T. Waite, A. Masion, J. C. Woicik, M. R. Wiesner, J.-y. Bottero, and C. C. E. Relation between the Redox State of Iron-Based Nanoparticles and Their Cytotoxicity toward Escherichia coli Relation between the Redox State of Iron-Based Nanoparticles and Their Cytotoxicity toward Escherichia coli. *Environmental Science & Technology*, 42(17):6730–6735, 2008.

15. M. Auffan, J. Rose, M. R. Wiesner, and J. Y. Bottero. Chemical stability of metallic nanoparticles: A parameter controlling their potential cellular toxicity in vitro. *Environmental Pollution*, 157:1127–1133, 2009.

16. G. Azimi, R. Dhiman, H.-M. Kwon, A. T. Paxson, and K. K. Varanasi. Hydrophobicity of rare-earth oxide ceramics. *Nature materials*, 12(4):315–20, 2013.

17. M. Baalousha, Y. Ju-Nam, P. A. Cole, J. A. Hriljac, I. P. Jones, C. R. Tyler, V. Stone, T. F. Fernandes, M. A. Jepson, and J. R. Lead. Characterization of cerium oxide nanoparticles-Part 2: Nonsize measurements. *Environmental Toxicology and Chemistry*, 31(5):994–1003, 2012.

18. Y. Bai, B. Qin, Y. Zhou, Y. Wang, Z. Wang, and W. Zheng. Preparation and antioxidant capacity of element selenium nanoparticles sol-gel compounds. *Journal of nanoscience and nanotechnology*, 11(6):5012–7, 2011.

19. L. E. Barton, M. Therezien, M. Auffan, J.-Y. Bottero, and M. R. Wiesner. Theory and Methodology for Determining Nanoparticle Affinity for Heteroaggregation in Environmental Matrices Using Batch Measurements. *Environmental Engineering Science*, 31(7):421–427, 2014.

20. BCCResearch. Global Markets for Nanocomposites, Nanoparticles, Nanoclays, and Nanotubes. Technical report, 2017.

21. S. Berber and D. Tománek. Hydrogen-induced disintegration of fullerenes and nanotubes: An ab initio study. *Physical Review B - Condensed Matter and Materials Physics*, 80(7):1–5, 2009.

22. J. N. Betts, M. G. Johnson, P. T. Rygiewicz, G. A. King, and C. P. Andersen. Potential for metal contamination by direct sonication of nanoparticle suspensions. *Environmental Toxicology and Chemistry*, 32(4):889–893, 2013.

23. B. Bhushan. *Springer Handbook of Nanotechnology*. 4th edition, 2017.

24. C. Blaise, F. Gagne, J. Ferard, and P. Eullaffroy. Ecotoxicity of Selected Nano-Materials to Aquatic Organisms. *Environmental Toxicology*, 23:591–598, 2008.

25. O. V. Buyevskaya, D. Wolf, and M. Baerns. Ethylene and propene by oxidative dehydrogenation of ethane and propane 'performance of rare-earth oxide-based catalysts and development of redox-type catalytic materials by combinatorial methods'. *Catalysis Today*, 62(1):91–99, 2000.

26. X. Cai, A. Lee, Z. Ji, C. Huang, C. H. Chang, X. Wang, Y. P. Liao, T. Xia, and R. Li. Reduction of pulmonary toxicity of metal oxide nanoparticles by phosphonate-based surface passivation. *Particle and Fibre Toxicology*, 14(1):1–11, 2017.

27. L. Canesi, R. Fabbri, G. Gallo, D. Vallotto, A. Marcomini, and G. Pojana. Biomarkers in Mytilus galloprovincialis exposed to suspensions of selected nanoparticles (Nano carbon black, C60 fullerene, Nano-TiO2, Nano-SiO2). *Aquatic Toxicology*, 100(2):168–177, 2010.

28. M. Cargnello, V. V. T. Doan-Nguyen, T. R. Gordon, R. E. Diaz, E. A. Stach, R. J. Gorte, P. Fornasiero, and C. B. Murray. Control of Metal Nanocrystal Size Reveals Metal-Support Interface Role for Ceria Catalysts. *Science*, 341(6147):771–773, 2013.

29. H. Carstensen, B. Muller, and R. Muller. Adsorption of ethoxylated surfactants on nanoparticles. I. Characterization by hydrophobic interaction chromatography. *International Journal of Pharmaceutics*, 67(1):29–37, 1991.

30. A. R. Cestari, E. F. S. Vieira, G. S. Vieira, and L. E. Almeida. Aggregation and adsorption of reactive dyes in the presence of an anionic surfactant on mesoporous aminopropyl silica. *Journal of Colloid and Interface Science*, 309(2):402–411, 2007.

31. P. Chairuangkitti, S. Lawanprasert, S. Roytrakul, S. Aueviriyavit, D. Phummiratch, K. Kulthong, P. Chanvorachote, and R. Maniratanachote. Silver nanoparticles induce toxicity in A549 cells via ROS-dependent and ROS-independent pathways. *Toxicology in Vitro*, 27(1):330–338, 2012.

32. ChemAxon. Chemicalize, 2017.

33. J. Chen, S. Patil, S. Seal, and J. F. McGinnis. Rare earth nanoparticles prevent retinal degeneration induced by intracellular peroxides. *Nature Nanotechnology*, 1(2):142–150, 2006.

34. I. Chowdhury, Y. Hong, R. J. Honda, and S. L. Walker. Mechanisms of TiO2 nanoparticle transport in porous media: Role of solution chemistry, nanoparticle concentration, and flowrate. *Journal of Colloid and Interface Science*, 360(2):548–555, 2011.

35. P. P. Chu and M. Jaipal Reddy. Sm2O3 composite PEO solid polymer electrolyte. *Journal of Power Sources*, 115(2):288–294, 2003.

36. J. Cohen, G. DeLoid, G. Pyrgiotakis, and P. Demokritou. Interactions of engineered nanomaterials in physiological media and implications for in vitro dosimetry. *Nanotoxicology*, 7(4):417–431, 2013.

37. J. M. Cohen, J. Beltran-Huarac, G. Pyrgiotakis, and P. Demokritou. Effective delivery of sonication energy to fast settling and agglomerating nanomaterial suspensions for cellular studies: Implications for stability, particle kinetics, dosimetry and toxicity. *NanoImpact*, 10(August 2017):81–86, 2018.

38. C. Contado, J. Mejia, O. Lozano García, J. P. Piret, E. Dumortier, O. Toussaint, and S. Lucas. Physicochemical and toxicological evaluation of silica nanoparticles suitable for food and consumer products collected by following the EC recommendation Field- and Flow-based Separations. *Analytical and Bioanalytical Chemistry*, 408(1):271–286, 2016.

39. A. Corma, P. Atienzar, H. García, and J.-Y. Chane-Ching. Hierarchically mesostructured doped CeO2 with potential for solar-cell use. *Nature Materials*, 3(6):394–397, 2004.

40. A. Corma, J. Y. Chane-Ching, M. Airiau, and C. Martínez. Synthesis and catalytic properties of thermally and hydrothermally stable, high-surface-area SiO2-CeO2 mesostructured composite materials and their application for the removal of sulfur compounds from gasoline. *Journal of Catalysis*, 224(2):441–448, 2004.

41. C. Corredor, M. D. Borysiak, J. Wolfer, P. Westerhoff, and J. D. Posner. Colorimetric Detection of Catalytic Reactivity of Nanoparticles in Complex Matrices. *Environmental Science & Technology*, 2015.

42. P. Cronholm, K. Midander, H. L. Karlsson, K. Elihn, I. O. Wallinder, and L. Möller. Effect of sonication and serum proteins on copper release from copper nanoparticles and the toxicity towards lung epithelial cells. *Nanotoxicology*, 5(2):269–281, 2011.

43. D. Cronin and T. Mark. The Role of Hydrophobicity in Toxicity Prediction. 2006.

44. J. De Waele, V. Galvita, H. Poelman, C. Detavernier, and J. Thybaut. Formation and stability of an active PdZn nanoparticle catalyst on a hydrotalcite-based support for ethanol dehydrogenation. *Catal. Sci. Technol.*, 7(17):3715–3727, 2017.

45. A. Deak, E. Hild, A. L. Kovacs, and Z. Horvolgyi. Contact angle determination of nanoparticles: film balance and scanning angle reflectometry studies. *Physical Chemistry Chemical Physics*, 9(48):6359–6370, 2007.

46. G. M. Deloid, J. M. Cohen, G. Pyrgiotakis, and P. Demokritou. Preparation, characterization, and in vitro dosimetry of dispersed, engineered nanomaterials. *Nature Protocols*, 12(2):355–371, 2017.

47. X. Deng, Z. Huang, W. Wang, and R. N. Davé. Investigation of nanoparticle agglomerates properties using Monte Carlo simulations. *Advanced Powder Technology*, 27(5):1971–1979, 2016.

48. L. Denluck, F. Wu, L. E. Crandon, B. J. Harper, and S. L. Harper. Reactive oxygen species generation is likely a driver of copper based nanomaterial toxicity. *Environmental Science: Nano*, 2018.

49. D. Ding, L. Li, K. Feng, Z. Liu, and C. Xia. High performance Ni-Sm2O3 cermet anodes for intermediate-temperature solid oxide fuel cells. *Journal of Power Sources*, 187(2):400–402, 2009.

50. S. Doktorovova, R. Shegokar, P. Martins-Lopes, A. M. Silva, C. M. Lopes, R. H. Müller, and E. B. Souto. Modified Rose Bengal assay for surface hydrophobicity evaluation of cationic solid lipid nanoparticles (cSLN). *European Journal of Pharmaceutical Sciences*, 45(5):606–612, 2012.

51. P. N. S. T. D. C. DR Baer, DL Gaspar. Application of surface Chemical Analysis tools for characterization of nanoparticles. *Anal Bioanal Chem*, 396(3):983–1002, 2010.

52. E. C. Dreaden, A. M. Alkilany, X. Huang, C. J. Murphy, and M. A. El-Sayed. The golden age: gold nanoparticles for biomedicine. *Chem. Soc. Rev.*, 41(7):2740–2779, 2012.

53. J. Duan, Y. Yu, Y. Li, Y. Yu, Y. Li, X. Zhou, P. Huang, and Z. Sun. Toxic Effect of Silica Nanoparticles on Endothelial Cells through DNA Damage Response via Chk1-Dependent G2/M Checkpoint. *PLoS ONE*, 8(4), 2013.

54. A. Eatemadi, H. Daraee, H. Karimkhanloo, M. Kouhi, and N. Zarghami. Carbon nanotubes : properties , synthesis , purification , and medical applications. pages 1–13, 2014.

55. P. D. Edmonds and K. S. Sancier. Evidence for free radical production by ultrasonic cavitation in biological media. *Ultrasound in Medicine & Biology*, 9(6):635–639, 1983.

56. A. Eguchi, T. Yoshitomi, M. Lazic, C. D. Johnson, L. B. Vong, A. Wree, D. Povero, B. G. Papouchado, Y. Nagasaki, and A. E. Feldstein. Redox nanoparticles as a novel treatment approach for inflammation and fibrosis associated with nonalcoholic steatohepatitis. *Nanomedicine (Lond)*, 10(17):2697–2708, 2015.

57. G. El-Damrawi and K. El-Egili. Characterization of novel CeO2-B2O3 glasses, structure and properties. *Physica B: Condensed Matter*, 299(1-2):180–186, 2001.

58. E. Farjami, L. Clima, K. V. Gothelf, and E. E. Ferapontova. DNA interactions with a Methylene Blue redox indicator depend on the DNA length and are sequence specific. *The Analyst*, 135(6):1443, 2010.

59. G. Federici, B. J. Shaw, and R. D. Handy. Toxicity of titanium dioxide nanoparticles to rainbow trout (Oncorhynchus mykiss): Gill injury, oxidative stress, and other physiological effects. *Aquatic Toxicology*, 84(4):415–430, 2007.

60. A. Finizio, M. Vighi, and D. Sandroni. Determination of n-octanol/water partition coefficient (Kow) of pesticide critical review and comparison of methods. *Chemosphere*, 1997.

61. A. T. Fisk, R. J. Norstrom, C. D. Cymbalisty, and D. G. Muir. Dietary accumulation and depuration of hydrophobic organochlorines: Bioaccumulation parameters and their relationship with the octanol/water partition coefficient. *Environmental Toxicology and Chemistry*, 17(5):951–961, 1998.

62. L. Foucaud, M. R. Wilson, D. M. Brown, and V. Stone. Measurement of reactive species production by nanoparticles prepared in biologically relevant media. *Toxicology Letters*, 174(1-3):1–9, 2007.

63. A. Gajewicz. What if the number of nanotoxicity data is too small for developing predictive Nano-QSAR models? An alternative read-across based approach for filling data gaps. *Nanoscale*, 9(24):8435–8448, 2017.

64. Z. Gao, Y. Horiguchi, K. Nakai, A. Matsumura, M. Suzuki, K. Ono, and Y. Nagasaki. Use of boron cluster-containing redox nanoparticles with ROS scavenging ability in boron neutron capture therapy to achieve high therapeutic efficiency and low adverse effects. *Biomaterials*, 104:201–212, 2016.

65. N. K. Geitner, N. J. O'Brien, A. A. Turner, E. J. Cummins, and M. R. Wiesner. Measuring Nanoparticle Attachment Efficiency in Complex Systems. *Environmental Science and Technology*, 51(22):13288–13294, 2017.

66. V. Gies and S. Zou. Systematic toxicity investigation of graphene oxide: evaluation of assay selection, cell type, exposure period and flake size. *Toxicology Research*, 7(1):93–101, 2018.

67. H. Goesmann and C. Feldmann. Nanoparticulate functional materials. *Angewandte Chemie - International Edition*, 49(8):1362–1395, 2010.

68. B. Harper, D. Thomas, S. Chikkagoudar, N. Baker, K. Tang, A. Heredia-Langner, R. Lins, and S. Harper. Comparative hazard analysis and toxicological modeling of diverse nanomaterials using the embryonic zebrafish (EZ) metric of toxicity. *Journal of Nanoparticle Research*, 17(6):1–12, 2015.

69. S. Harper, C. Usenko, J. Hutchison, B. Maddux, and R. Tanguay. Biodistribution and Toxicity Depends on Nanomaterial Composition, Size, Surface Functionalisation and Route of Exposure. *Journal of Experimental Nanoscience*, 3(March 2015):195–206, 2008.

70. N. B. Hartmann, K. A. Jensen, A. Baun, K. Rasmussen, H. Rauscher, R. Tantra, D. Cupi, D. Gilliland, F. Pianella, and J. M. Riego Sintes. Techniques and Protocols for Dispersing Nanoparticle Powders in Aqueous Media - Is there a Rationale for Harmonization? *Journal of Toxicology and Environmental Health - Part B: Critical Reviews*, 18(6):299–326, 2015.

71. C. O. Hendren, G. V. Lowry, J. M. Unrine, and M. R. Wiesner. A functional assay-based strategy for nanomaterial risk forecasting. *Science of the Total Environment*, 536:1029–1037, 2015.

72. P. A. Holden, J. Gardea-Torresdey, F. Klaessig, R. F. Turco, M. Mortimer, K. Hund-Rinke, E. A. Cohen Hubal, D. Avery, D. Barcelo, R. Behra, Y. Cohen, L. Deydier-Stephan, P. L. Ferguson, T. F. Fernandes, B. Herr Harthorn, W. M. Henderson, R. A. Hoke, D. Hristozov, J. M. Johnston, A. B. Kane, L. Kapustka, A. A. Keller, H. S. Lenihan, W. Lovell, C. J. Murphy, R. M. Nisbet, E. J. Petersen, E. R. Salinas, M. Scheringer, M. Sharma, D. E. Speed, Y. Sultan, P. Westerhoff, J. C. White, M. R. Wiesner, E. M. Wong, B. Xing, M. Steele Horan, H. A. Godwin, and A. E. Nel. Considerations of Environmentally Relevant Test Conditions for Improved Evaluation of Ecological Hazards of Engineered Nanomaterials. *Environmental science & technology*, 2016.

73. A. M. Horst, R. Vukanti, J. H. Priester, and P. A. Holden. An assessment of fluorescence- and absorbance-based assays to study metal-oxide nanoparticle ROS production and effects on bacterial membranes. *Small*, 9(9-10):1753–1764, 2013.

74. W.-C. Hou, B. Y. Moghadam, C. Corredor, P. Westerhoff, and J. D. Posner. Distribution of Functionalized Gold Nanoparticles between Water and Lipid Bilayers as Model Cell Membranes. *Environmental Science & Technology*, 46(3):1869–1876, 2012.

75. K. D. Hristovski, P. K. Westerhoff, and J. D. Posner. Octanol-water distribution of engineered nanomaterials. *Journal of Environmental Science and Health - Part A Toxic/Hazardous Substances and Environmental Engineering*, 46(6):636–647, 2011.

76. I.-L. Hsiao and Y.-J. Huang. Effects of various physicochemical characteristics on the toxicities of ZnO and TiO2 nanoparticles toward human lung epithelial cells. *Science of The Total Environment*, 409(7):1219–1228, 2011.

77. Y. Hu, T. Guo, X. Ye, Q. Li, M. Guo, H. Liu, and Z. Wu. Dye adsorption by resins: Effect of ionic strength on hydrophobic and electrostatic interactions. *Chemical Engineering Journal*, 228:392–397, 2013.

78. J. E. Hutchison. The road to sustainable nanotechnology: Challenges, progress and opportunities. *ACS Sustainable Chemistry & Engineering*, page acssuschemeng.6b02121, 2016.

79. K.-i. Ishibashi, A. Fujishima, T. Watanabe, and K. Hashimoto. Quantum yields of active oxidative species formed on TiO2 photocatalyst. *Journal of Photochemistry and Photobiology A: Chemistry*, 134(1-2):139–142, 2000.

80. C. T. Jafvert and P. P. Kulkarni. Buckminsterfullerene's (C 60 ) Octanol-Water Partition Coefficient (K ow ) and Aqueous Solubility. *Environmental Science & Technology*, 42(765):5945–5950, 2008.

81. N. R. Jana, Z. L. Wang, and T. Pal. Redox Catalytic Properties of Palladium Nanoparticles: Surfactant and Electron Donor-Acceptor Effects. *Langmuir*, 16:2457–2463, 2000.

82. K. A. Jensen, Y. Kembouche, E. Christiansen, N. Jacobsen, and H. Wallin. Towards a method for detecting the potential genotoxicity of nanomaterials Final protocol for producing suitable manufactured nanomaterial exposure media Web-Report The generic NANOGENOTOX dispersion protocol Standard Operation Procedure ( SOP ) October ,. Technical report, Nanogenotox, 2011.

83. Z. J. Jiang, C. Y. Liu, and L. W. Sun. Catalytic properties of silver nanoparticles supported on silica spheres. *The Journal of Physical Chemistry B*, 109:1730–1735, 2005.

84. H. J. Jo, J. W. Choi, S. H. Lee, and S. W. Hong. Acute toxicity of Ag and CuO nanoparticle suspensions against Daphnia magna: The importance

of their dissolved fraction varying with preparation methods. *Journal of Hazardous Materials*, 227-228:301–308, 2012.

85. M. C. Jones, S. A. Jones, Y. Riffo-Vasquez, D. Spina, E. Hoffman, A. Morgan, A. Patel, C. Page, B. Forbes, and L. A. Dailey. Quantitative assessment of nanoparticle surface hydrophobicity and its influence on pulmonary biocompatibility. *Journal of Controlled Release*, 183(1):94–104, 2014.

86. I. Jośko, P. Oleszczuk, and E. Skwarek. Toxicity of combined mixtures of nanoparticles to plants. *Journal of Hazardous Materials*, 331:200–209, 2017.

87. M. Kang, C. H. Lim, and J. H. Han. Comparison of toxicity and deposition of nano-sized carbon black aerosol prepared with or without dispersing sonication. *Toxicological Research*, 29(2):121–127, 2013.

88. A. Karakoti, S. Singh, J. M. Dowding, S. Seal, and W. T. Self. Redox-active radical scavenging nanomaterials. *Chem. Soc. Rev*, 39:4422–4432, 2010.

89. H. L. Karlsson, P. Cronholm, Y. Hedberg, M. Tornberg, L. De Battice, S. Svedhem, and I. O. Wallinder. Cell membrane damage and protein interaction induced by copper containing nanoparticles-Importance of the metal release process. *Toxicology*, 313(1):59–69, 2013.

90. M. Kaur and N. K. Verma. Structural and optical properties of Eu2O3 coated TiO2 nanoparticles and their application for dye sensitized solar cell. *Journal of Materials Science: Materials in Electronics*, 24(4):1121–1127, 2013.

91. H. Kawasaki, Y. Takeda, and R. Arakawa. Mass spectrometric analysis for high molecular weight synthetic polymers using ultrasonic degradation and the mechanism of degradation. *Analytical Chemistry*, 79(11):4182–4187, 2007.

92. A. A. Keller, S. McFerran, A. Lazareva, and S. Suh. Global life cycle releases of engineered nanomaterials. *Journal of Nanoparticle Research*, 15(6), 2013.

93. A. A. Keller, H. Wang, D. Zhou, H. S. Lenihan, G. Cheer, B. J. Cardinale, R. Miller, Z. Ji, G. Cherr, B. J. Cardinale, R. Miller, and J. I. Zhaoxia. Stability and Aggregation of Metal Oxide Nanoparticles in Natural Aqueous Matrices. *Environ. Sci. Technol.*, 44(6):1962–1967, 2010.

94. J. Kim, S. V. Chankeshwara, F. Thielbeer, J. Jeong, K. Donaldson, M. Bradley, and W.-S. Cho. Surface charge determines the lung inflammogenicity: A study with polystyrene nanoparticles. *Nanotoxicology*, 5390(November 2017):1–8, 2015.

95. S. T. Kim, K. Saha, C. Kim, and V. M. Rotello. The role of surface functionality in determining nanoparticle cytotoxicity. *Accounts of Chemical Research*, 46(3):681–691, 2013.

96. T. Kimura, T. Sakamoto, J.-M. Leveque, H. Sohmiya, M. Fujita, S. Ikeda, and T. Ando. Standardization of ultrasonic power for sonochemical reaction. *Ultrasonics Sonochemistry*, 3(3):S157–S161, 1996.

97. S. Koda, T. Kimura, T. Kondo, and H. Mitome. A standard method to calibrate sonochemical efficiency of an individual reaction system. *Ultrasonics Sonochemistry*, 10(3):149–156, 2003.

98. M. Kosmulski. A literature survey of the differences between the reported isoelectric points and their discussion. *Colloids and Surfaces A: Physicochemical and Engineering Aspects*, 222(1-3):113–118, 2003.

99. A. Kroll, M. H. Pillukat, D. Hahn, and J. Schnekenburger. Interference of engineered nanoparticles with in vitro toxicity assays. *Archives of Toxicology*, 86(7):1123–1136, 2012.

100. G. Laban, L. F. Nies, R. F. Turco, J. W. Bickham, and M. S. Sep??lveda. The effects of silver nanoparticles on fathead minnow (Pimephales promelas) embryos. *Ecotoxicology*, 19(1):185–195, 2010.

101. E. P. Labrinea and C. A. Georgiou. Stopped-flow method for assessment of pH and timing effect on the ABTS total antioxidant capacity assay. *Analytica Chimica Acta*, 526(1):63–68, 2004.

102. T. Lammel and J. Sturve. Assessment of titanium dioxide nanoparticle toxicity in the rainbow trout (Onchorynchus mykiss) liver and gill cell lines RTL-W1 and RTgill-W1 under particular consideration of nanoparticle stability and interference with fluorometric assays. *NanoImpact*, 11(December 2017):1–19, 2018.

103. D. Langevin, E. Raspaud, S. Mariot, A. Knyazev, A. Stocco, A. Salonen, A. Luch, A. Haase, B. Trouiller, C. Relier, O. Lozano, S. Thomas, A. Salvati, and K. Dawson. NanoImpact Towards reproducible measurement of nanoparticle size using dynamic light scattering : Important controls and considerations. *NanoImpact*, 10(February):161–167, 2018.

104. C. Larue, H. Khodja, N. Herlin-Boime, F. Brisset, A. M. Flank, B. Fayard, S. Chaillou, and M. Carrière. Investigation of titanium dioxide nanoparticles toxicity and uptake by plants. *Journal of Physics: Conference Series*, 304:012057, 2011.

105. C. P. Lebel, H. Ischiropoulos, and S. C. Bondys. Evaluation of the Probe 2',7'-Dichiorofluorescin as an Indicator of Reactive Oxygen Species Formation and Oxidative Stress. *Chem. Res. Toxicol*, 5:227–231, 1992.

106. F. Li and Y. Gu. Improvement of performance of dye-sensitized solar cells by doping Er2O3 into TiO2 electrodes. *Materials Science in Semiconductor Processing*, 15(1):11–14, 2012.

107. S. Li, S. Zhai, Y. Liu, H. Zhou, J. Wu, Q. Jiao, B. Zhang, H. Zhu, and B. Yan. Experimental modulation and computational model of nanohydrophobicity. *Biomaterials*, 52(1):312–317, 2015.

108. X. Li, T. D. Scheibe, and W. P. Johnson. Apparent decreases in colloid deposition rate coefficients with distance of transport under unfavorable deposition conditions: A general phenomenon. *Environmental Science and Technology*, 38(21):5616–5625, 2004.

109. Y. Li, X. Chen, and N. Gu. Computational Investigation of Interaction between Nanoparticles and Membranes : Hydrophobic / Hydrophilic Effect. *Journal of Physical Chemistry B*, 112(51):16647–16653, 2008.

110. Y. Li, J. Niu, E. Shang, and J. C. Crittenden. Influence of dissolved organic matter on photogenerated reactive oxygen species and metal-oxide nanoparticle toxicity. *Water Research*, 98:9–18, 2016.

111. W. Lin, Y. W. Huang, X. D. Zhou, and Y. Ma. Toxicity of cerium oxide nanoparticles in human lung cancer cells. *International Journal of Toxicology*, 25(6):451–457, 2006.

112. X. Lin, J. Li, S. Ma, G. Liu, K. Yang, M. Tong, and D. Lin. Toxicity of TiO2 nanoparticles to Escherichia coli: effects of particle size, crystal phase and water chemistry. *PloS one*, 9(10):e110247, 2014.

113. J. Liu, G. Lagger, P. Tacchini, and H. H. Girault. Generation of OH radicals at palladium oxide nanoparticle modified electrodes, and scavenging by fluorescent probes and antioxidants. *Journal of Electroanalytical Chemistry*, 619-620(1-2):131–136, 2008.

114. R. Liu, L.-S. Qiang, W.-D. Yang, and H.-Y. Liu. Enhanced conversion efficiency of dye-sensitized solar cells using Sm2O3âĂŞmodified TiO2 nanotubes. *Journal of Power Sources*, 223:254–258, 2013.

115. X. Liu, Z. Jiang, J. Li, Z. Zhang, and L. Ren. Super-hydrophobic property of nano-sized cupric oxide films. *Surface and Coatings Technology*, 204(20):3200–3204, 2010.

116. Y. Liu, S. Wang, Z. Wang, N. Ye, H. Fang, and D. Wang. TiO2, SiO2 and ZrO2 Nanoparticles Synergistically Provoke Cellular Oxidative Damage in Freshwater Microalgae. *Nanomaterials*, 8(2):95, 2018.

117. S. Lopes, F. Ribeiro, J. Wojnarowicz, W. Lojkowski, K. Jurkschat, A. Crossley, A. M. V. M. Soares, and S. Loureiro. Zinc oxide nanoparticles toxicity to Daphnia magna: Size-dependent effects and dissolution. *Environmental Toxicology and Chemistry*, 33(1):190–198, 2014.

118. C. López-Alarcón and A. Denicola. Evaluating the antioxidant capacity of natural products: A review on chemical and cellular-based assays. *Analytica Chimica Acta*, 763:1–10, 2013.

119. G. V. Lowry, K. B. Gregory, S. C. Apte, and J. R. Lead. Transformations of Nanomaterials in the Environment. *Environmental Science & Technology*, 46:6893–6899, 2012.

120. G. V. Lowry, R. J. Hill, S. Harper, A. F. Rawle, C. O. Hendren, F. Klaessig, U. Nobbmann, P. Sayre, and J. Rumble. Guidance to improve the scientific value of zeta-potential measurements in nanoEHS. *Environ. Sci.: Nano*, 3(5):953–965, 2016.

121. G. V. Lowry, E. M. Hotze, E. S. Bernhardt, D. D. Dionysiou, J. A. Pedersen, M. R. Wiesner, and B. Xing. Environmental Occurrences, Behavior, Fate, and Ecological Effects of Nanomaterials: An Introduction to the Special Series. *Journal of Environment Quality*, 39(6):1867, 2010.

122. I. Lynch, C. Weiss, and E. Valsami-Jones. A strategy for grouping of nanomaterials based on key physico-chemical descriptors as a basis for safer-by-design NMs. *Nano Today*, 9:266–270, 2014.

123. J. Ma, T. S. Zhang, L. B. Kong, P. Hing, and S. H. Chan. Ce0.8Gd0.2O2-$\delta$ ceramics derived from commercial submicron-sized CeO2 and Gd2O3 powders for use as electrolytes in solid oxide fuel cells. *Journal of Power Sources*, 132(1-2):71–76, 2004.

124. A. Maestro, E. Guzmán, F. Ortega, and R. G. Rubio. Contact angle of micro- and nanoparticles at fluid interfaces. *Current Opinion in Colloid and Interface Science*, 19(4):355–367, 2014.

125. K. Mallick, M. Witcomb, and M. Scurrell. Silver nanoparticle catalysed redox reaction: An electron relay effect. *Materials Chemistry and Physics*, 97(2-3):283–287, 2006.

126. N. Mandzy, E. Grulke, and T. Druffel. Breakage of TiO2 agglomerates in electrostatically stabilized aqueous dispersions. *Powder Technology*, 160(2):121–126, 2005.

127. L. Manusadžianas, C. Caillet, L. Fachetti, B. Gylytė, R. Grigutytė, S. Jurkonienė, R. Karitonas, K. Sadauskas, F. Thomas, R. Vitkus, and J.-F. Férard. Toxicity of copper oxide nanoparticle suspensions to aquatic biota. *Environmental Toxicology and Chemistry*, 31(1):108–114, 2012.

128. R. L. Marchese Robinson, I. Lynch, W. Peijnenburg, J. Rumble, F. Klaessig, C. Marquardt, H. Rauscher, T. Puzyn, R. Purian, C. Åberg, S. Karcher, H. Vriens, P. Hoet, M. D. Hoover, C. O. Hendren, and S. L. Harper. How should the completeness and quality of curated nanomaterial data be evaluated? *Nanoscale*, 8(19):9919–9943, 2016.

129. W. I. M. M. Meylan, P. H. H. H. Oward, and R. O. S. B. Oethling. Improved Method for Estimating Water Solubility From Octanol / Water Partition Coefficient. *Environmental Toxicology and Chemistry*, 18(4):664–672, 1999.

130. K. Midander, P. Cronholm, H. L. Karlsson, K. Elihn, L. Möller, C. Leygraf, and I. O. Wallinder. Surface characteristics, copper release, and toxicity of nano- and micrometer-sized copper and copper(ll) oxide particles: A cross-disciplinary study. *Small*, 5(3):389–399, 2009.

131. B. Miljevic, F. Hedayat, S. Stevanovic, K. E. Fairfull-Smith, S. E. Bottle, and Z. D. Ristovski. To sonicate or not to sonicate PM filters: Reactive oxygen species generation upon ultrasonic irradiation. *Aerosol Science and Technology*, 48(12):1276–1284, 2014.

132. Y. Min, M. Akbulut, K. Kristiansen, Y. Golan, and J. Israelachvili. The role of interparticle and external forces in nanoparticle assembly. *Nature Materials*, 7(7):527–538, 2008.

133. X. J. L. M. R. D. E. H. Minghua Li, S. Pokhrel. Stability, Bioavailability, and Bacterial Toxicity of ZnO and Iron-Doped ZnO Nanoparticles in Aquatic Media. *Environ. Sci. Technol*, 45(2):755, 2011.

134. M. R. Mohammadi and D. J. Fray. Development of nanocrystalline TiO2-Er2O3 and TiO2-Ta2O5 thin film gas sensors: Controlling the physical and sensing properties. *Sensors and Actuators, B: Chemical*, 141(1):76–84, 2009.

135. M. Mortimer, K. Kasemets, and A. Kahru. Toxicity of ZnO and CuO nanoparticles to ciliated protozoa Tetrahymena thermophila. *Toxicology*, 269(2-3):182–189, 2010.

136. D. F. Moyano, K. Saha, G. Prakash, B. Yan, H. Kong, M. Yazdani, and V. M. Rotello. Fabrication of corona-free nanoparticles with tunable hydrophobicity. *ACS Nano*, 8(7):6748–6755, 2014.

137. Y. Mu, F. Wu, Q. Zhao, R. Ji, Y. Qie, Y. Zhou, Y. Hu, C. Pang, D. Hristozov, J. P. Giesy, and B. Xing. Predicting toxic potencies of metal oxide nanoparticles by means of nano-QSARs. *Nanotoxicology*, 10(9):1207–1214, 2016.

138. I. A. Mudunkotuwa, J. M. Pettibone, and V. H. Grassian. Environmental implications of nanoparticle aging in the processing and fate of copper-based nanomaterials. *Environmental Science and Technology*, 46(13):7001–7010, 2012.

139. R. H. Muller, D. Ruhl, M. Luck, and B.-R. Paulke. Influence of Fluorescent Labelling of Polystyrene Particles on Phagocytic Uptake, Surface Hydrophobicity, and Plasma Protein Adsorption. *Pharmaceutical Research*, 14(1):18–24, 1997.

140. A. Nel. Toxic Potential of Materials at the Nanolevel. *Science*, 311(5761):622–627, 2006.

141. B. Nelson, M. Johnson, M. Walker, K. Riley, and C. Sims. Antioxidant Cerium Oxide Nanoparticles in Biology and Medicine. *Antioxidants*, 5(2):15, 2016.

142. N. Neubauer, J. Palomaeki, P. Karisola, H. Alenius, and G. Kasper. Size-dependent ROS production by palladium and nickel nanoparticles in cellular and acellular environments - An indication for the catalytic nature of their interactions. *Nanotoxicology*, 9(8):1059–1066, 2015.

143. X. Niu, H. Zhong, X. Wang, and K. Jiang. Sensing properties of rare earth oxide doped In2O3 by a sol-gel method. *Sensors and Actuators, B: Chemical*, 115(1):434–438, 2006.

144. S. Noventa, C. Hacker, D. Rowe, C. Elgy, and T. Galloway. Dissolution and bandgap paradigms for predicting the toxicity of metal oxide nanoparticles in the marine environment: an in vivo study with oyster embryos. *Nanotoxicology*, 12(1):63–78, 2018.

145. OECD. OECD guideline for the testing of chemicals: partition coefficient (n-octanol/water): shake flask method. *Giudance*, 107(July):1–4, 1995.

146. OECD. Guidance on Sample Preparation and Dosimetry for the Safety Testing of Manufactured Nanomaterials Environment. *Series on the Safety of Manufactured Nanomaterials, No. 36*, 2012.

147. OECD. Dispersion stability of nanomaterials in simulated environmental media. *OECD Guideline for the Testing of Chemicals*, (January):1–4, 2017.

148. OECD-WPMN. Physical-Chemical Properties of Nanomaterials: Evaluation of Methods Applied in the OECD–WPMN Test Programme. Technical report, Environmental Directorate, Organization for Economic Cooperation and Development, Paris, 2016.

149. A. Opez-Serrano, R. M. noz Olivas, J. Sanz Landaluze, and C. Amara. Nanoparticles: a global vision. Characterization, separation, and quantification methods. Potential environmental and health impact. *Analytical Methods*, 2013.

150. A. Oukarroum, S. Bras, F. Perreault, and R. Popovic. Inhibitory effects of silver nanoparticles in two green algae, Chlorella vulgaris and Dunaliella tertiolecta. *Ecotoxicology and Environmental Safety*, 78:80–85, 2012.

151. A. K. Pal, D. Bello, B. Budhlall, E. Rogers, and D. K. Milton. Screening for oxidative stress elicited by engineered nanomaterials: Evaluation of acellular DCFH assay. *Dose-Response*, 10(3):308–330, 2012.

152. J. P. Pantina and E. M. Furst. Colloidal aggregate micromechanics in the presence of divalent ions. *Langmuir*, 22(12):5282–5288, 2006.

153. S. Park. Direct Oxidation of Hydrocarbons in a Solid Oxide Fuel Cell: I. Methane Oxidation. *Journal of The Electrochemical Society*, 146(10):3603, 1999.

154. I. Passagne, M. Morille, M. Rousset, I. Pujalt??, and B. L'Azou. Implication of oxidative stress in size-dependent toxicity of silica nanoparticles in kidney cells. *Toxicology*, 299(2-3):112–124, 2012.

155. A. C. Patel, S. Li, C. Wang, W. Zhang, and Y. Wei. Electrospinning of porous silica nanofibers containing silver nanoparticles for catalytic applications. *Chemistry of Materials*, 19(6):1231–1238, 2007.

156. E. J. Petersen, Q. Huang, and W. J. Weber. Relevance of octanol-water distribution measurements to the potential ecological uptake of multi-walled carbon nanotubes. *Environmental Toxicology and Chemistry*, 29(5):1106–1112, 2010.

157. V. Polshettiwar and R. S. Varma. Green chemistry by nano-catalysis. *Green Chemistry*, 12(5):743, 2010.

158. W. L. Poon, H. Alenius, J. Ndika, V. Fortino, V. Kolhinen, A. Meščeriakovas, M. Wang, D. Greco, A. Lähde, J. Jokiniemi, J. C. Y. Lee, H. El-Nezami, and P. Karisola. Nano-sized zinc oxide and silver, but not titanium dioxide, induce innate and adaptive immunity and antiviral response in differentiated THP-1 cells. *Nanotoxicology*, 0(0):1–16, 2017.

159. S. Pradhan, J. Hedberg, E. Blomberg, S. Wold, and I. Odnevall Wallinder. Effect of sonication on particle dispersion, administered dose and metal release of non-functionalized, non-inert metal nanoparticles. *Journal of Nanoparticle Research*, 18(9):1–14, 2016.

160. A. Praetorius, J. J. Labille, M. Scheringer, A. Thill, K. Hungerbühler, J. Y. Bottero, K. Hungerb??hler, and J. Y. Bottero. Heteroaggregation of titanium dioxide nanoparticles with model natural colloids under environmentally relevant conditions. *Environmental Science and Technology*, 48(18):10690–10698, 2014.

161. A. Praetorius, M. Scheringer, and K. Hungerbühler. Development of environmental fate models for engineered nanoparticles - A case study of TiO 2 nanoparticles in the rhine river. *Environmental Science and Technology*, 46(12):6705–6713, 2012.

162. A. Praetorius, N. Tufenkji, K.-U. Goss, M. Scheringer, F. von der Kammer, and M. Elimelech. The road to nowhere: equilibrium partition coefficients for nanoparticles. *Environmental Science: Nano*, 1(4), 2014.

163. Prospect. Protocol for Nanoparticle Dispersion. Technical Report May, 2010.

164. T. Puzyn, B. Rasulev, A. Gajewicz, X. Hu, T. P. Dasari, A. Michalkova, H.-M. Hwang, A. Toropov, D. Leszczynska, and J. Leszczynski. Using nano-QSAR to predict the cytotoxicity of metal oxide nanoparticles. *Nature nanotechnology*, 6(3):175–8, 2011.

165. J. Queiroz, C. Tomaz, and J. Cabral. Hydrophobic interaction chromatography of proteins. *Journal of Biotechnology*, 87(2):143–159, 2001.

166. K. Rasmussen, M. González, P. Kearns, J. R. Sintes, F. Rossi, and P. Sayre. Review of achievements of the OECD Working Party on Manufactured Nanomaterials' Testing and Assessment Programme. From exploratory testing to test guidelines. *Regulatory Toxicology and Pharmacology*, 2016.

167. K. Rasmussen, H. Rauscher, A. Mech, J. Riego Sintes, D. Gilliland, M. González, P. Kearns, K. Moss, M. Visser, M. Groenewold, and E. A. Bleeker. Physico-chemical properties of manufactured nanomaterials - Characterisation and relevant methods. An outlook based on the OECD Testing Programme. *Regulatory Toxicology and Pharmacology*, 92(October 2017):8–28, 2018.

168. J. Raso, P. Mañas, R. Pagán, and F. J. Sala. Influence of different factors on the output power transferred into medium by ultrasound. *Ultrasonics Sonochemistry*, 5(4):157–162, 1999.

169. P. Riello, S. Bucella, R. Krsmanovi̇ĉ, S. Meneghetti, S. Pietrantoni, and R. Francini. Synthesis, X-ray diffraction characterization, and radiative properties of Er2O3-ZrO2 nanocrystals embedded in LAS glass ceramic. *Journal of Physical Chemistry B*, 109(28):13424–13430, 2005.

170. A. D. Rieux, E. G. E. Ragnarsson, E. Gullberg, V. Préat, Y. J. Schneider, and P. Artursson. Transport of nanoparticles across an in vitro model of the human intestinal follicle associated epithelium. *European Journal of Pharmaceutical Sciences*, 2005.

171. I. Rodea-Palomares, K. Boltes, F. Fernández-Piñas, F. Leganés, E. García-Calvo, J. Santiago, and R. Rosal. Physicochemical characterization and ecotoxicological assessment of CeO2 nanoparticles using two aquatic microorganisms. *Toxicological Sciences*, 119(1):135–145, 2011.

172. E. Roduner. Size matters: why nanomaterials are different. *Chemical Society Reviews*, 35(7):583, 2006.

173. G. Roebben, S. Ramirez-Garcia, V. A. Hackley, M. Roesslein, F. Klaessig, V. Kestens, I. Lynch, C. M. Garner, A. Rawle, A. Elder, V. L. Colvin, W. Kreyling, H. F. Krug, Z. A. Lewicka, S. McNeil, A. Nel, A. Patri, P. Wick, M. Wiesner, T. Xia, G. Oberdörster, and K. A. Dawson. Interlaboratory comparison of size and surface charge measurements on nanoparticles prior to biological impact assessment. *Journal of Nanoparticle Research*, 13(7):2675–2687, 2011.

174. J. Y. Roh, Y. K. Park, K. Park, and J. Choi. Ecotoxicological investigation of CeO2 and TiO2 nanoparticles on the soil nematode Caenorhabditis elegans using gene expression, growth, fertility, and survival as endpoints. *Environmental Toxicology and Pharmacology*, 29(2):167–172, 2010.

175. M. P. Rosynek. Catalytic Properties of Rare Earth Oxides. *Catalysis Reviews*, 16(1):111–154, 1977.

176. I. M. Sadiq, S. Pakrashi, N. Chandrasekaran, and A. Mukherjee. Studies on toxicity of aluminum oxide (Al2O3) nanoparticles to microalgae species: Scenedesmus sp. and Chlorella sp. *Journal of Nanoparticle Research*, 13(8):3287–3299, 2011.

177. T. Sager, M. Wolfarth, M. Keane, D. Porter, V. Castranova, and A. Holian. Effects of nickel-oxide nanoparticle pre-exposure dispersion status on bioactivity in the mouse lung. *Nanotoxicology*, 5390(October 2017):1–11, 2015.

178. T. Sato, T. Katakura, S. Yin, T. Fujimoto, and S. Yabe. Synthesis and UV-shielding properties of calcia-doped ceria nanoparticles coated with amorphous silica. *Solid State Ionics*, 172(1-4 SPEC. ISS.):377–382, 2004.

179. J.-J. Sauvain, S. Deslarzes, and M. Riediker. Nanoparticle reactivity toward dithiothreitol. *Nanotoxicology*, 2(3):121–129, 2008.

180. M. Schieber and N. S. Chandel. ROS function in redoz signaling and oxidative stress. *Current Biology*, 24(10):1–25, 2014.

181. H. I. Schlesinger, H. C. Brown, A. E. Finholt, J. R. Gilbreath, H. R. Hoekstra, and E. K. Hyde. Sodium Borohydride, Its Hydrolysis and its Use as a Reducing Agent and in the Generation of Hydrogen. *J. Am. Chem. Soc.*, 75(3):215–219, 1953.

182. M. Shaaban, a. Ali, and M. El-Nimr. The AC conductivity of tellurite glasses doped with Ho2O3. *Materials Chemistry and Physics*, 96(2-3):433–438, 2006.

183. S. Sharifi, S. Behzadi, S. Laurent, F. Ml, P. Stroeve, and M. Mahmoudi. Toxicity of nanomaterials. *Chemical Society reviews*, 41:2323–2343, 2012.

184. J. A. Shatkin and K. J. Ong. Alternative Testing Strategies for Nanomaterials: State of the Science and Considerations for Risk Analysis. *Risk Analysis*, 36(8):1564–1580, 2016.

185. H. K. Shin, M. Seo, S. E. Shin, K.-Y. Kim, J.-W. Park, and K. T. No. Meta-analysis of Daphnia magna nanotoxicity experiments in accordance with test guidelines. *Environmental Science: Nano*, 5(3):765–775, 2018.

186. T. Smith. The hydrophilic nature of a clean gold surface. *Journal of Colloid And Interface Science*, 75(1):51–55, 1980.

187. S. K. Sohaebuddin, P. T. Thevenot, D. Baker, J. W. Eaton, and L. Tang. Nanomaterial cytotoxicity is composition, size, and cell type dependent. *Particle and Fibre Toxicology*, 7(1):22, 2010.

188. J. E. Song, T. Phenrat, S. Marinakos, Y. Xiao, J. Liu, M. R. Wiesner, R. D. Tilton, and G. V. Lowry. Hydrophobic interactions increase attachment of gum arabic- and PVP-coated Ag nanoparticles to hydrophobic surfaces. *Environmental Science and Technology*, 45:5988–5995, 2011.

189. L. Song, M. Connolly, M. L. Fernández-Cruz, M. G. Vijver, M. Fernández, E. Conde, G. R. de Snoo, W. J. Peijnenburg, and J. M. Navas. Species-specific toxicity of copper nanoparticles among mammalian and piscine cell lines. *Nanotoxicology*, 8(4):383–393, 2014.

190. W. J. Stark, P. R. Stoessel, W. Wohlleben, and A. Hafner. Industrial applications of nanoparticles. *Chem. Soc. Rev.*, 44(16):5793–5805, 2015.

191. M. M. Sthijns, W. Thongkam, C. Albrecht, B. Hellack, A. Bast, G. R. Haenen, and R. P. Schins. Silver nanoparticles induce hormesis in A549 human epithelial cells. *Toxicology in Vitro*, 40:223–233, 2017.

192. T. Y. Suman, S. R. Radhika Rajasree, and R. Kirubagaran. Evaluation of zinc oxide nanoparticles toxicity on marine algae chlorella vulgaris through flow cytometric, cytotoxicity and oxidative stress analysis. *Ecotoxicology and Environmental Safety*, 113:23–30, 2015.

193. H. Sun, K. Hu, H. Lou, and X. Zheng. Biodiesel Production from Transesterification of Rapeseed Oil Using KF/Eu 2O 3 as a Catalyst. *Energy & Fuels*, 22(4):2756–2760, 2008.

194. K. S. Suslick, D. A. Hammerton, and R. E. Cline. The Sonochemical Hot Spot. *Journal of the American Chemical Society*, 108(18):5641–5642, 1986.

195. K. Suttiponparnit, J. Jiang, M. Sahu, S. Suvachittanont, T. Charinpanitkul, and P. Biswas. Role of Surface Area, Primary Particle Size, and Crystal Phase on Titanium Dioxide Nanoparticle Dispersion Properties. *Nanoscale Research Letters*, 6(1):1–8, 2011.

196. R. Tantra, A. Cackett, R. Peck, D. Gohil, and J. Snowden. Measurement of redox potential in nanoecotoxicological investigations. *Journal of Toxicology*, 2012.

197. R. Tantra, C. Oksel, T. Puzyn, J. Wang, K. N. Robinson, X. Z. Wang, C. Y. Ma, and T. Wilkins. Nano(Q)SAR: Challenges, pitfalls and perspectives. *Nanotoxicology*, 9(5):636–642, 2015.

198. R. Tassinari, F. Cubadda, G. Moracci, F. Aureli, M. DâĂŹAmato, M. Valeri, B. De Berardis, A. Raggi, A. Mantovani, D. Passeri, M. Rossi, and F. Maranghi. Oral, short-term exposure to titanium dioxide nanoparticles in Sprague-Dawley rat: focus on reproductive and endocrine systems and spleen. *Nanotoxicology*, 8(6):654–662, 2014.

199. J. Taurozzi, V. A. Hackley, and M. R. Wiesner. Protocol for Preparation of Nanoparticle Dispersions From Powdered Material Using Ultrasonic Disruption. *CEINT, National Institute of Standars and Technology*, pages 1–10, 2012.

200. J. S. Taurozzi, V. A. Hackley, and M. R. Wiesner. Ultrasonic dispersion of nanoparticles for environmental, health and safety assessment issues and recommendations. *Nanotoxicology*, 5(4):711–729, 2011.

201. J. S. Taurozzi, V. a. Hackley, and M. R. Wiesner. Preparation of a nanoscale TiO2 aqueous dispersion for toxicological or environmental testing. *NIST Special Publication*, 1200:3, 2012.

202. D. N. Thomas, S. J. Judd, and N. Fawcett. Flocculation modelling: A review. *Water Research*, 33(7):1579–1592, 1999.

203. T. B. Tilly, L. L. Kerr, L. K. Braydich-Stolle, J. J. Schlager, and S. M. Hussain. Dispersions of geometric TiO2nanomaterials and their toxicity to RPMI 2650 nasal epithelial cells. *Journal of Nanoparticle Research*, 16(11), 2014.

204. E. Topuz, L. Sigg, and I. Talinli. A systematic evaluation of agglomeration of Ag and TiO 2 nanoparticles under freshwater relevant conditions. *Environmental Pollution*, 193:37–44, 2014.

205. J. Tournebize, A. Sapin-Minet, G. Bartosz, P. Leroy, and A. Boudier. Pitfalls of assays devoted to evaluation of oxidative stress induced by inorganic nanoparticles. *Talanta*, 116:753–763, 2013.

206. J. Tschirch, R. Dillert, D. Bahnemann, B. Proft, A. Biedermann, and B. Goer. Photodegradation of methylene blue in water, a standard method to determine the activity of photocatalytic coatings? *Research on Chemical Intermediates*, 34(4):381–392, 2008.

207. N. Tufenkji and M. Elimelech. Breakdown of colloid filtration theory: Role of the secondary energy minimum and surface charge heterogeneities. *Langmuir*, 21(3):841–852, 2005.

208. X. Valentini, L. Absil, G. Laurent, A. Robbe, S. Laurent, R. Muller, A. Legrand, and D. Nonclercq. Toxicity of TiO2 nanoparticles on the NRK52E renal cell line. *Molecular & Cellular Toxicology*, 13(4):419–431, 2017.

209. M. E. Vance, T. Kuiken, E. P. Vejerano, S. P. McGinnis, M. F. Hochella, D. Rejeski, and M. S. Hull. Nanotechnology in the real world: Redeveloping the nanomaterial consumer products inventory. *Beilstein Journal of Nanotechnology*, 2015.

210. O. Vasylkiv and Y. Sakka. Synthesis and Colloidal Processing of Zirconia Nanopowder. *Journal of the American Ceramic Society*, 84(11):2489–2494, 2001.

211. P. Velmurugan, J. Shim, and B. T. Oh. Removal of anionic dye using amine-functionalized mesoporous hollow shells prepared from corn cob silica. *Research on Chemical Intermediates*, 42(6):5937–5950, 2016.

212. B. E. Vencalek, S. N. Laughton, E. Spielman-Sun, S. M. Rodrigues, J. M. Unrine, G. V. Lowry, and K. B. Gregory. In Situ Measurement of CuO and Cu(OH)2 Nanoparticle Dissolution Rates in Quiescent Freshwater Mesocosms. *Environmental Science and Technology Letters*, 3(10):375–380, 2016.

213. V. K. Vidhu and D. Philip. Catalytic degradation of organic dyes using biosynthesized silver nanoparticles. *Micron*, 56:54–62, 2014.

214. N. von Moos and V. Slaveykova. Oxidative stress induced by inorganic nanoparticles in bacteria and aquatic microalgae–state of the art and knowledge gaps. *Nanotoxicology*, 8(6):605–630, 2014.

215. G. Wagner, V. Korenkov, J. Judy, and P. Bertsch. Nanoparticles Composed of Zn and ZnO Inhibit Peronospora tabacina Spore Germination in vitro and P. tabacina Infectivity on Tobacco Leaves. *Nanomaterials*, 6(3):50, 2016.

216. C. Walkey, S. Das, S. Seal, J. Erlichman, K. Heckman, L. Ghibelli, E. Traversa, J. F. McGinnis, and W. T. Self. Catalytic properties and biomedical applications of cerium oxide nanoparticles. *Environ. Sci.: Nano*, 2(1):33–53, 2015.

217. L.-S. Wang, L. Wang, L. Wang, G. Wang, Z.-H. Li, and J.-J. Wang. Effect of 1-butyl-3-methylimidazolium tetrafluoroborate on the wheat (Triticum aestivum L.) seedlings. *Environmental toxicology*, 24(3):296–303, 2009.

218. R. Wang, T. Hughes, S. Beck, S. Vakil, S. Li, P. Pantano, and R. K. Draper. Generation of toxic degradation products by sonication of Pluronic® dispersants: implications for nanotoxicity testing. *Nanotoxicology*, 7(7):1272–1281, 2012.

219. R. Wang, C. Mikoryak, S. Li, D. Bushdiecker, I. H. Musselman, P. Pantano, and R. K. Draper. Cytotoxicity screening of single-walled carbon nanotubes: Detection and removal of cytotoxic contaminants from carboxylated carbon nanotubes. *Molecular Pharmaceutics*, 8(4):1351–1361, 2011.

220. X. Z. Wang, Y. Yang, R. Li, C. Mcguinnes, J. Adamson, I. L. Megson, and K. Donaldson. Principal component and causal analysis of structural and acute in vitro toxicity data for nanoparticles. *Nanotoxicology*, 8(5):465–476, 2014.

221. L. C. Wehmas, C. Anders, J. Chess, A. Punnoose, C. B. Pereira, J. A. Greenwood, and R. L. Tanguay. Comparative metal oxide nanoparticle toxicity using embryonic zebrafish. *Toxicology Reports*, 2:702–715, 2015.

222. T. Xia, Y. Zhao, T. Sager, S. George, S. Pokhrel, N. Li, D. Schoenfeld, H. Meng, S. Lin, X. Wang, M. Wang, Z. Ji, J. I. Zink, L. M??dler, V. Castranova, S. Lin, and A. E. Nel. Decreased dissolution of ZnO by iron doping yields nanoparticles with reduced toxicity in the rodent lung and zebrafish embryos. *ACS Nano*, 5(2):1223–1235, 2011.

223. Y. Xiao and M. R. Wiesner. Characterization of surface hydrophobicity of engineered nanoparticles. *Journal of Hazardous Materials*, 215-216(216):146–151, 2012.

224. X. Yang, H. Pan, P. Wang, and F. J. Zhao. Particle-specific toxicity and bioavailability of cerium oxide (CeO2) nanoparticles to Arabidopsis thaliana. *Journal of Hazardous Materials*, 322:292–300, 2017.

225. H. Zhang, Z. Ji, T. Xia, H. Meng, C. Low-Kam, R. Liu, S. Pokhrel, S. Lin, X. Wang, Y. P. Liao, M. Wang, L. Li, R. Rallo, R. Damoiseaux, D. Telesca, L. Mädler, Y. Cohen, J. I. Zink, A. E. Nel, L. M??dler, Y. Cohen, J. I. Zink, and A. E. Nel. Use of metal oxide nanoparticle band gap to develop a predictive paradigm for oxidative stress and acute pulmonary inflammation. *ACS Nano*, 6(5):4349–4368, 2012.

226. M. Zhang, M. Yang, T. Morimoto, N. Tajima, K. Ichiraku, K. Fujita, S. Iijima, M. Yudasaka, and T. Okazaki. Size-dependent cell uptake of carbon nanotubes by macrophages: A comparative and quantitative study. *Carbon*, 127:93–101, 2018.

227. Y. Zhang, Y. Chen, P. Westerhoff, K. Hristovski, and J. C. Crittenden. Stability of commercial metal oxide nanoparticles in water. *Water Research*, 42(8-9):2204–2212, 2008.

228. J. Zhao and M. Riediker. Detecting the oxidative reactivity of nanoparticles: A new protocol for reducing artifacts. *Journal of Nanoparticle Research*, 16(7):2493, 2014.

229. Y. Zhao, J. L. C. Howe, Z. Yu, D. T. Leong, J. J. H. Chu, J. S. C. Loo, and K. W. Ng. Exposure to titanium dioxide nanoparticles induces autophagy in primary human keratinocytes. *Small*, 9(3):387–392, 2013.

230. X. Zheng, X. Zhang, X. Wang, S. Wang, and S. Wu. Preparation and characterization of CuO/CeO2 catalysts and their applications in low-temperature CO oxidation. *Applied Catalysis A: General*, 295(2):142–149, 2005.

231. Y. Zheng and A. Wang. Ag nanoparticle-entrapped hydrogel as promising material for catalytic reduction of organic dyes. *Journal of Materials Chemistry*, 22(32):16552, 2012.

232. T. Zhou, W. Fan, Y. Liu, and X. Wang. Comparative assessment of the chronic effects of five nano-perovskites on Daphnia magna: a structure-based toxicity mechanism. *Environmental Science: Nano*, 2018.

233. Y. Zhou, Z. Zhang, C. Yuan, J. Li, C. Xia, Z. Zhan, and S. Wang. Metal-supported solid oxide fuel cells with in-situ sintered (Bi 2O3)0.7(Er2O3) 0.3-Ag composite cathode. *International Journal of Hydrogen Energy*, 38(36):16579–16583, 2013.

234. Z. Zhou, J. Son, B. Harper, Z. Zhou, and S. Harper. Influence of surface chemical properties on the toxicity of engineered zinc oxide nanoparticles to embryonic zebrafish. *Beilstein Journal of Nanotechnology*, 6(1):1568–1579, 2015.

235. L. Zhu, G. Tang, Q. Shi, C. Cai, and J. Yin. Neodymium oxide-assisted melt free-radical grafting of maleic anhydride on isotactic-polypropylene by reactive extrusion. *Journal of Polymer Science, Part B: Polymer Physics*, 44(1):134–142, 2006.

236. M. Zhu, G. Nie, H. Meng, T. Xia, A. Nel, and Y. Zhao. Physicochemical properties determine nanomaterial cellular uptake, transport, and fate. *Accounts of Chemical Research*, 46(3):622–631, 2013.

237. X. Zhu, Y. Chang, and Y. Chen. Toxicity and bioaccumulation of TiO2 nanoparticle aggregates in Daphnia magna. *Chemosphere*, 78(3):209–215, 2010.

# APPENDICES

# A Supporting Information for Chapter 2

TABLE A.1: Review of of sonication practices in recent nanotoxicology studies

| **NP** | **Sonicator** | **Time** | **Power** | **Energy (J)** | **Conc ($\mu$g mL)** | **DLS?** | **Media** | **Ref** |
|---|---|---|---|---|---|---|---|---|
| ZnO, $TiO_2$ | bath | | 400 W/40 kHz | | 1.56 to 50 | Yes | serum free DMEME | [76] |
| Carbon black | bath | 2h, again 10 min before exposure | | | 10 to 30 | no | NaCl, BSA, DPPC, or cell culture RPMI 1640 medium | [62] |
| $TiO_2$ (Aeroxide P25) | bath | 6h (again 30 min before dosing) | 35 kHz | | 10000 | TEM | MQ | [59] |
| $TiO_2$ (P25, Degussa) and $CeO_2$ | cup horn | 30 min | 50% (100W) | | 1000 | Yes | 1 mM KCl | [10] |
| $TiO_2$ | bath | 10 min + 10 min before exposure | | | 10 | yes | 1x PBS | [229] |
| Zn | bath | 5 min | 22 W | 6600 | | Yes | DI | [215] |
| TiO2 (P25 Degussa) | probe | 1 min | 60000 Hz | | 500 | Yes | DI | [203] |
| CuO | bath | 30 min. | | | 50 | Yes | ISO daphnia medium | [1] |
| $SiO_2$ | probe | 120 s | 50% (10 W) | 1200 | 2000 | no | DI | [38] |
| | bath | 15 min | 50Hz-150 W | 135000 | 3000 | | DI | |
| ZnO | bath | 30 min | | | 50-300 | | sea water | [192] |
| Cu | bath | 10 min. | 140 W, 37 kHz | | 200 | Yes | culture media | [189] |

| | | | | | | | | |
|---|---|---|---|---|---|---|---|---|
| polystyrene | bath | 10 min. | | | 18-24 | Yes | DW | [94] |
| ZnO | | approx 30 min. | | | 50 | Yes | MQ | [117] |
| $TiO_2$ (anatase, Sigma Aldrich) | probe | 15 min. | | | | SEM | ultrapure water | [198] |
| Ag | bath | 6 hrs + 15 min before dosing | | | 400 | TEM | DI | [13] |
| Ag and CuO | bath | 1 or 2 h | 40 kHz | | 100-500 | Yes | moderately hard water | [84] |
| $TiO_2$ (Degussa P25) | not reported | 10 min. + 10 min before dosing | 50 W/L, 40 kHz | 450 | 1000 | Yes | MQ | [237] |
| $Al_2O_3$ | not reported | 30 min. | 750 W (20 kHz) | 1350000 | 3-192 | Yes | algal medium | [176] |
| Ni | bath | 15 min | 40 W | 36000 | 1000 | Yes | DI | [4] |
| CuO | bath | 15 min | 300W, 35 kHz | 270000 | 10000 | | DI | [127] |
| Ag | not reported | 2 min | | | 100 | yes | nanopure, BG-11, and McLachlan | [150] |
| $SiO_2$ | bath | 15 min | 40 W | 36000 | 200 | yes | Water and cell culture medium | [5] |
| $NiFe_2O_4$ | bath | 10 min | 40 W | 24000 | | YES | Cell culture medium | [3] |
| Ag | not reported | 15 min. | | | | Yes | moderately hard reconstituted water | [8] |
| $SiO_2$ | probe | 20 s | 60 W (130W, 56-60Hz) | 3600 | | YES | DI | [154] |
| Cu and Cu-Zn | probe | 2x20 s | | | 2000 | yes | PBS | [89] |

| | | | | | | | | |
|---|---|---|---|---|---|---|---|---|
| $SiO_2$ | bath | 5 min. | 160 W, 20 kHz | 48000 | | Yes | | [53] |
| $TiO_2$, $SiO_2$, MWCNT | bath | 60 s 40 W | 2400 | 10-1000 | Yes | PBS and culture medium | [187] | |
| $TiO_2$ (P25, Aeroxide) | probe | 30 min (pulsed mode, 1 s on, 1 s off) | | | 10000 | Yes | ultrapure water | [104] |
| Ag | probe | 2x20 s | 14 W | 560 | 1000 | Yes | serum-containing medium | [42] |
| ZnO and CuO | not reported | 30 min, then stored | | | 40000 | SEM | MQ | [135] |
| Ag | bath | 1.5 h | 15 kHz | | 1000 | TEM | MQ | [100] |
| $CeO_2$ and $TiO_2$ | bath | 20 min. | | | | TEM | K-medium | [174] |
| $TiO_2$ (5 types) | not reported | 30min | 100W, 40 kHz | 180000 | 500 | Yes | ultrapure water | [112] |
| Ag | bath | 10 min. | | | 2 | Yes | DI | [31] |
| SWNT | bath | 4 h | 120W, 40 kHz | 1728000 | 1000 | no | HEPES + BSA | [219] |
| carbon black, $C_{60}$, $TiO_2$, $SiO_2$ | probe | 15 min | 100W, 50% on/off cycle | 45000 | 100 | | artificial sea water | [27] |
| ZnO, Ag, $TiO_2$ | bath | 20 min. stock, then 20 min diluted | 37 kHz, effective power 25 W, max peak performance 280 W | 30000 | 1000 | Yes | cRPMI | [158] |
| $SiO_2$, $Ag/SiO_2$, $CeO_2$, $Fe_2O_3$, $TiO_2$ | probe | varies | 400 W 60 Hz: actually delivered = 3.14 W | 2000 | 1000 | Yes | DI | [36] |

| | | | | | | | | |
|---|---|---|---|---|---|---|---|---|
| ZnO | not reported | | 30 W | | 5000 | Yes | DI | [222] |
| ZnO | bath | 30 min | 100 W | 180000 | 1000 | | DI | [133] |
| CNTs (single and multi, 8 types) | probe? | 5 h | | | 1400 | Yes | 10 mg/mL BSA | [226] |
| perovskite nanomaterials (PNMs) ($LaFeO_3$, $YFeO_3$, $BiFeO_3$, $LaMnO_3$, $LaCoO_3$) | not reported | 30 min | | | 100 | Yes | SM7 media with and w/o 200 mg/L GA | [232] |
| graphene oxide | probe | 0.5-85 min (depending on GO) | 10 W | 300–5e5 | 2000 | Yes | sterile water | [66] |
| $TiO_2$ | probe | 15 min | 20 W | 18000 | 1000 | Yes | MQ | [102] |
| CeO2 | bath | 30 min | 100 W, 40 kHz | 180000 | 3000 | TEM | MQ | [224] |
| ZnO, CuO, $TiO_2$, $Cr_2O_3$, $Fe_2O_3$, | bath | 30 min. | 250 W, 50 Hz | | 1000 | Yes | distilled water | [86] |
| CoO, $Ni_2O_3$, CuO, $Co_3O_4$, $TiO_2$ | bath | 15 min. 100 W, 42 kHz | 90000 | 5000 | | no | DI water | [26] |
| $TiO_2$ | bath | 15 min. | 40 kHz, 600 W | 540000 | 2000 | Yes | PBS | [208] |
| Ag | cup horn | 10 min | power of 5.71 (200W) and 20% duty cycle | 120000 | 1000 | | sterile RNase free water with 2% Adult Bovine Serum (ABS) | [191] |

| | | | | | | |
|---|---|---|---|---|---|---|
| $TiO_2$, $SiO_2$, and $ZrO_2$ | bath | 30 min. | | Yes | ultrapure water | [116] |

TABLE A.2: Average PDI Values

| | | Ultrapure water | | KCl | | FW | |
|---|---|---|---|---|---|---|---|
| | | **CeO2** | **TiO2** | **CeO2** | **TiO2** | **CeO2** | **TiO2** |
| | No Sonication | 0.71 | 0.76 | 0.75 | 0.91 | 0.81 | 0.89 |
| probe | 20% | 0.36 | 0.8 | 0.38 | 0.8 | | |
| | 30% | 0.36 | 0.73 | 0.36 | 0.73 | | |
| | 40% | 0.35 | 0.79 | 0.4 | 0.7 | | |
| cup horn | 20% | 0.29 | 0.59 | 0.35 | 0.67 | 0.34 | 0.73 |
| | 30% | 0.42 | 0.58 | 0.39 | 0.65 | 0.39 | 0.66 |
| | 40% | 0.45 | 0.73 | 0.38 | 0.68 | 0.5 | 0.68 |
| | Bath | 0.43 | 0.74 | 0.49 | 0.71 | 0.41 | 0.65 |

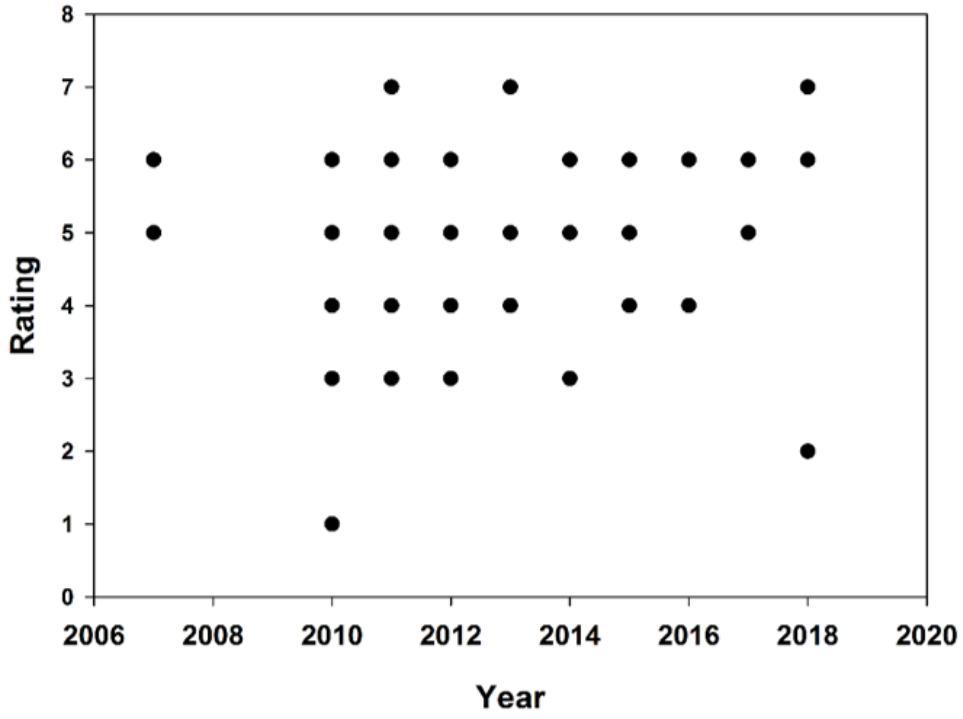


FIGURE A.1: Rating of quality of reported metadata (1-7) by publication year (n=56 studies).

# B Supporting Information for Chapter 3

TABLE B.1: Standardized information for determining the zeta potential in 0.5x PBS

| | |
|---|---|
| **Shape** | spherical |
| **Model used to compute zeta potential** | Henry's Equation (Smoluchowski approximation) |
| **Applied voltage** | 148 V |
| **Replicate measurements** | 3 |
| **Equilibration time** | 120 s |
| **Concentration NPs** | 10 mg/L (Au) 50 mg/L (CuO) 100 mg/L (SiO2 and Ami-SiO2) |
| **0.5x PBS** | |
| **pH** | 7.8 ± 0.2 |
| **Temperature** | 25°C |
| **Ionic strength** | 83 mM |
| **Viscosity** | 0.8508 cP |
| **Macromolecules/NOM present** | none |

FIGURE B.1: The shake flask method for octanol water partitioning performed using Au NPs. Particles were visually observed to partition to the aqueous phase.

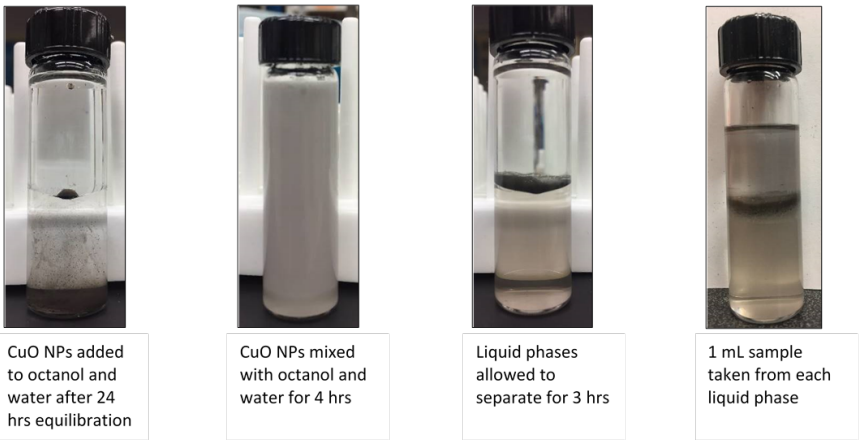


FIGURE B.2: The shake flask octanol-water partitioning method performed with CuO NPs. NPs are visually observed to sit at the octanol-water interface.

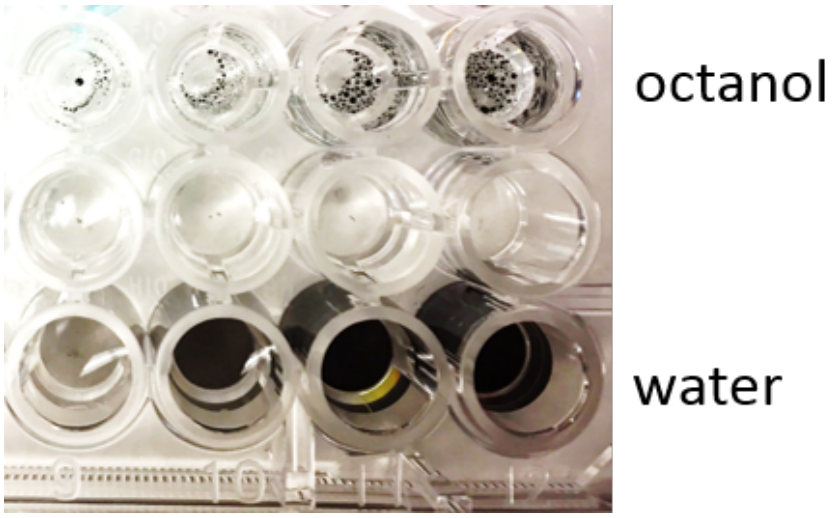


FIGURE B.3: CuO NPs suspended in octanol and water. A standard curve could not be performed to quantify CuO concentration in octanol because NPs could not be uniformly dispersed.

The dye adsorption assay was performed using $H_2O_2$ as a positive control. The $H_2O_2$ concentrations used were higher than have been observed to be generated by CuO NPs [48].

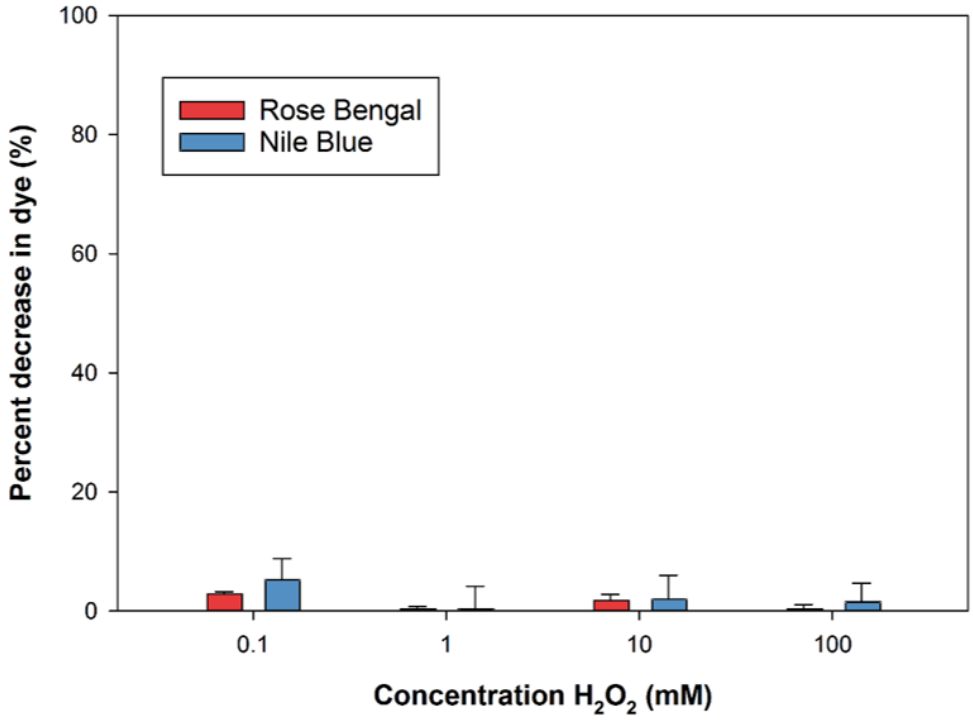


FIGURE B.4: Percent decrease in dye concentration as a function of hydrogen peroxide concentration.

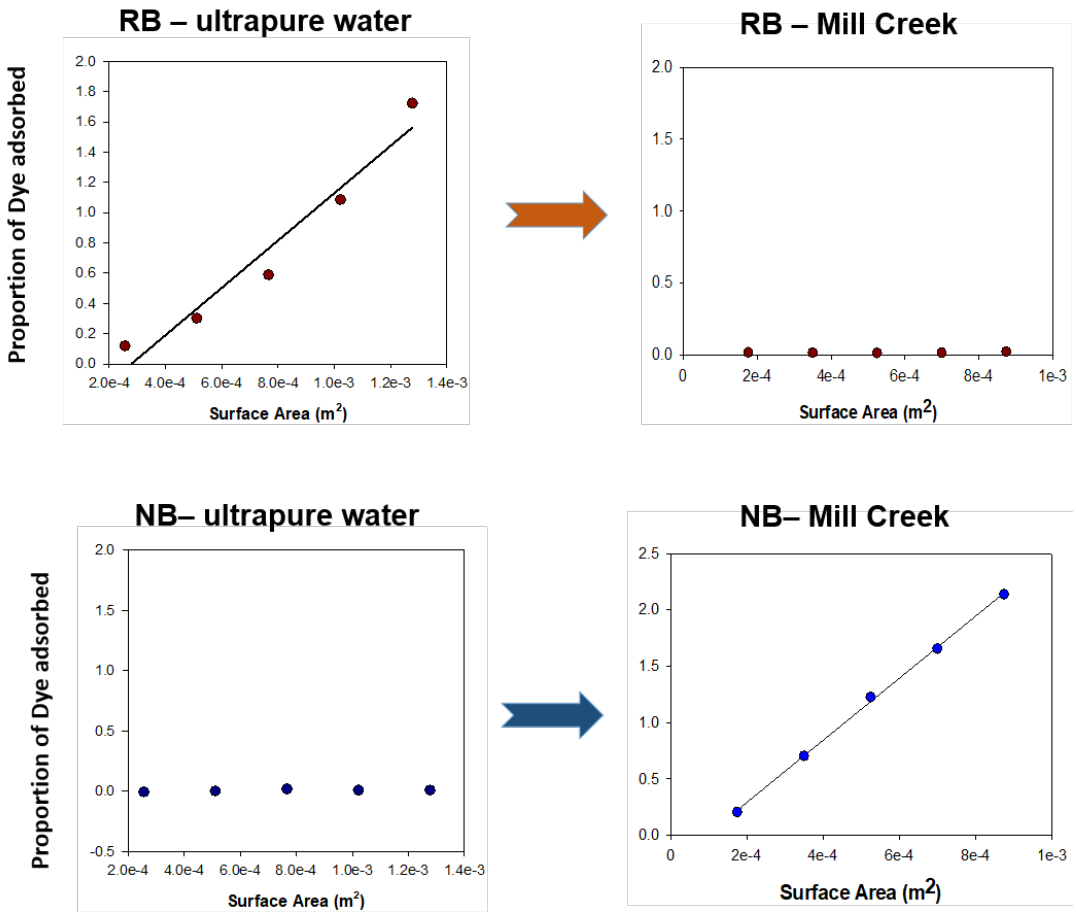


FIGURE B.5: Change in dye adsorption after incubation in natural fresh water. $TiO_2$ NPs had high adsorption of RB in ultrapure water and low adsorption of NB, but after incubation with fresh water NPs adsorbed NB. NP surface area was approximated using the measured HDD.

| Mill Creek properties | |
|---|---|
| pH | 8.53 |
| Conductivity ($\mu$S/cm) | 100 |
| Alkalinity (mg/L) | 37.6 |
| Hardness (mg/L) | 25 |

# C Supporting Information for Chapter 4

TABLE C.1: Properties of lanthanide and lanthanide oxides

| **Property** | **$CeO_2$** | **$Nd_2O_3$** | **$Sm_2O_3$** | **$Eu_2O_3$** | **$Gd_2O_3$** | **$Ho_2O_3$** | **$Er_2O_3$** | **Me/MeOx?** |
|---|---|---|---|---|---|---|---|---|
| Standard enthalpy of formation of gaseous RE atoms (298 K) | 420.1 | 326.9 | 206.7 | 177.4 | 397.5 | 300.6 | 361.4 | Me |
| Freezing Point (° C) | 2210 | 2233 | 2269 | 2291 | 2339 | 2330 | 2344 | MeOx |
| Boiling Point (° C) | 3730 | 3760 | 3780 | 3790 | 3900 | 3900 | 3920 | MeOx |
| Band Gap (eV) | 2.4 | 4.7 | 5 | 4.4 | 5.4 | 5.13 | 5.3 | MeOx |
| Standard enthalpy of formation of RE sesquioxides (kJ/mol, 298 K) | 1796 | 1808 | 1828 | 1652 | 1816 | 1881 | 1898 | MeOx |
| Lattice Energy of sesquioxides (kJ/mol) | -12901 | -13008 | -13181 | -13271 | -13330 | -13588 | -13665 | MeOx |
| BertzCT (topological index meant to quantify "complexity" of molecules | 23.77 | 34.16 | 4.85 | 34.16 | 4.85 | 34.16 | 34.16 | MeOx |
| ExactMolWt (g/mol) | 171.89 | 331.8 | 351.82 | 353.82 | 363.833 | 377.84 | 379.84 | MeOx |
| MolLogP | -0.2376 | -0.306 | -0.3564 | -0.306 | -0.3564 | -0.306 | -0.306 | MeOx |
| Valence Electrons | 12 | 26 | 30 | 32 | 34 | 40 | 42 | MeOx |
| Unpaired e's | 1 | 3 | 5 | 6 | 7 | 4 | 3 | Me |
| Ionization Energy (eV) | 36.76 | 40.41 | 41.4 | 42.7 | 44 | 42.5 | 42.7 | Me |
| electrons in 4f | 1 | 3 | 5 | 6 | 7 | 10 | 11 | Me |
| HDD (nm) | 2934.33 | 866.47 | 1875.33 | 971.13 | 1875.33 | 1507.67 | 1728 | MeOx |
| Ln-O Bond length (A) | 2.27 | 2.35 | 2.31 | 2.3 | 2.29 | 2.25 | 2.24 | MeOx |
| Ionic Radius (A) | 1.15 | 1.12 | 1.1 | 1.09 | 1.08 | 1.04 | 1.03 | Me |
| Electronegativity | 2.79 | 2.81 | 2.82 | 2.83 | 2.81 | 2.83 | 2.83 | MeOx |
| Density (g/cm3) | 6.77 | 7.01 | 7.52 | 5.24 | 7.9 | 8.79 | 9.07 | MeOx |
| Contact Angle | 103 | 101 | 107 | 104 | 109 | 115 | 108 | MeOx |
| Boiling Point (°C) | 3468 | 3027 | 1900 | 1429 | 3000 | 2600 | 2900 | |
| Oxidation State | 4 | 3 | 3 | 3 | 3 | 3 | 3 | Me |
| Lattice Energy (kJ/mol) | -12901 | -13008 | -13181 | -13271 | -13330 | -13588 | -13665 | MeOx |
| Reduction potential to neutral (3) | -2.34 | -2.32 | -1.55 | -1.99 | -2.28 | -2.33 | -2.33 | Me |
| Atomic Number | 58 | 60 | 62 | 63 | 64 | 67 | 68 | |
| Polarizability (Angstroms$\hat{3}$) | 7.53 | 14.78 | 15.13 | 15.31 | 15.49 | 16.02 | 16.2 | MeOx |
| Log S | 0.08 | 0.39 | 0.46 | 0.48 | 0.54 | 0.63 | 0.65 | MeOx |
| Van der Waals volume (âĎń3) | 53.03 | 92.48 | 92.48 | 92.48 | 92.48 | 92.48 | 92.48 | MeOx |
| Van der Waals Surface Area ($^2$) | 91.51 | 143.54 | 143.54 | 143.54 | 143.54 | 143.54 | 143.54 | MeOx |
| Solvent accessible surface area ($^2$) | 235.61 | 339.64 | 339.64 | 339.64 | 339.64 | 339.64 | 339.64 | MeOx |

| | | | | | | | | |
|---|---|---|---|---|---|---|---|---|
| Topological polar surface area ($^2$) | 34.14 | 43.37 | 43.37 | 43.37 | 43.37 | 43.37 | 43.37 | MeOx |

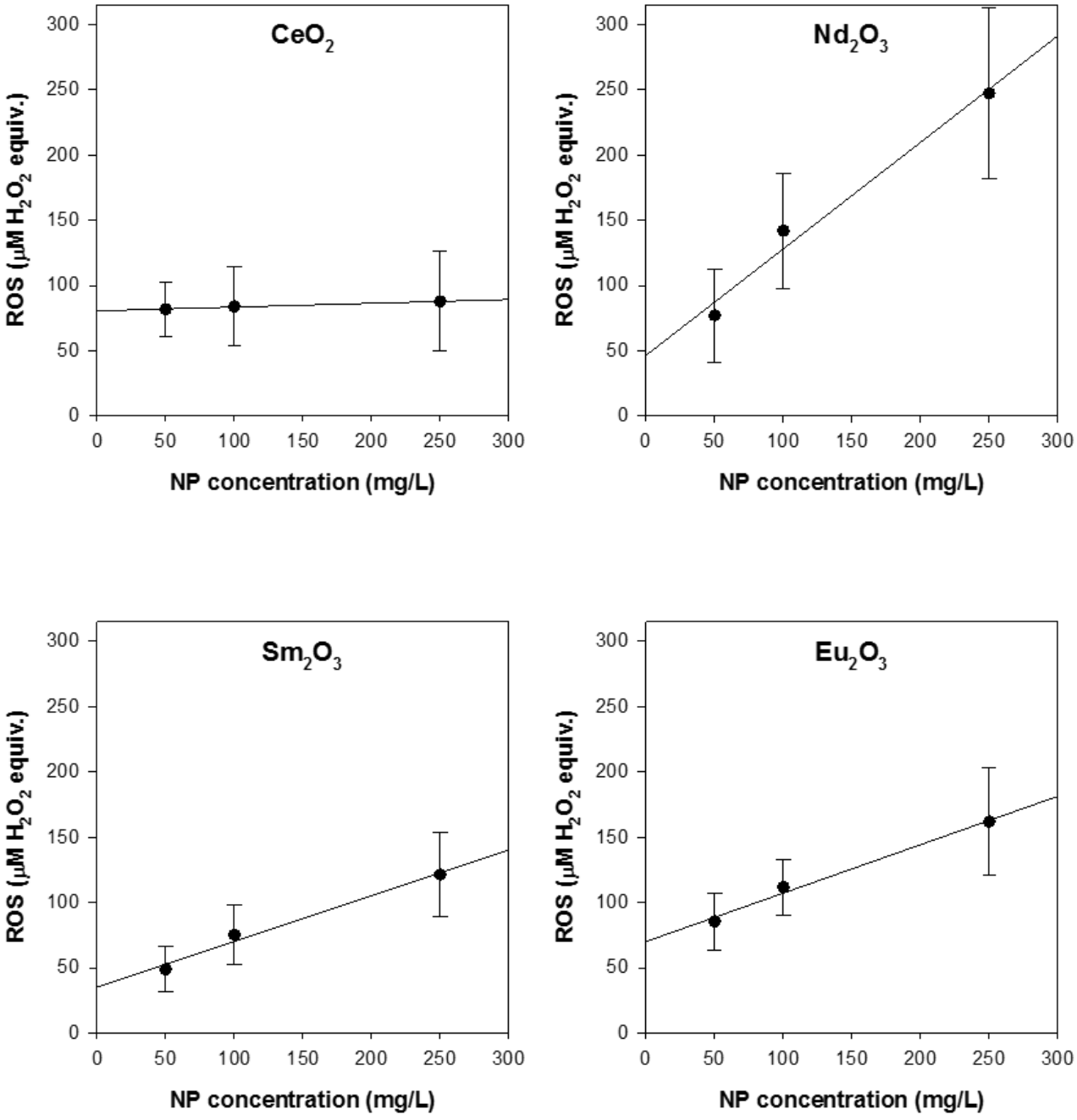


FIGURE C.1: Reactive oxygen species (ROS), reported in units of $\mu$M $H_2O_2$ equivalent, generated by 50, 100, and 250 mg/L LnOx NPs. Error bars represent standard error (n=3).

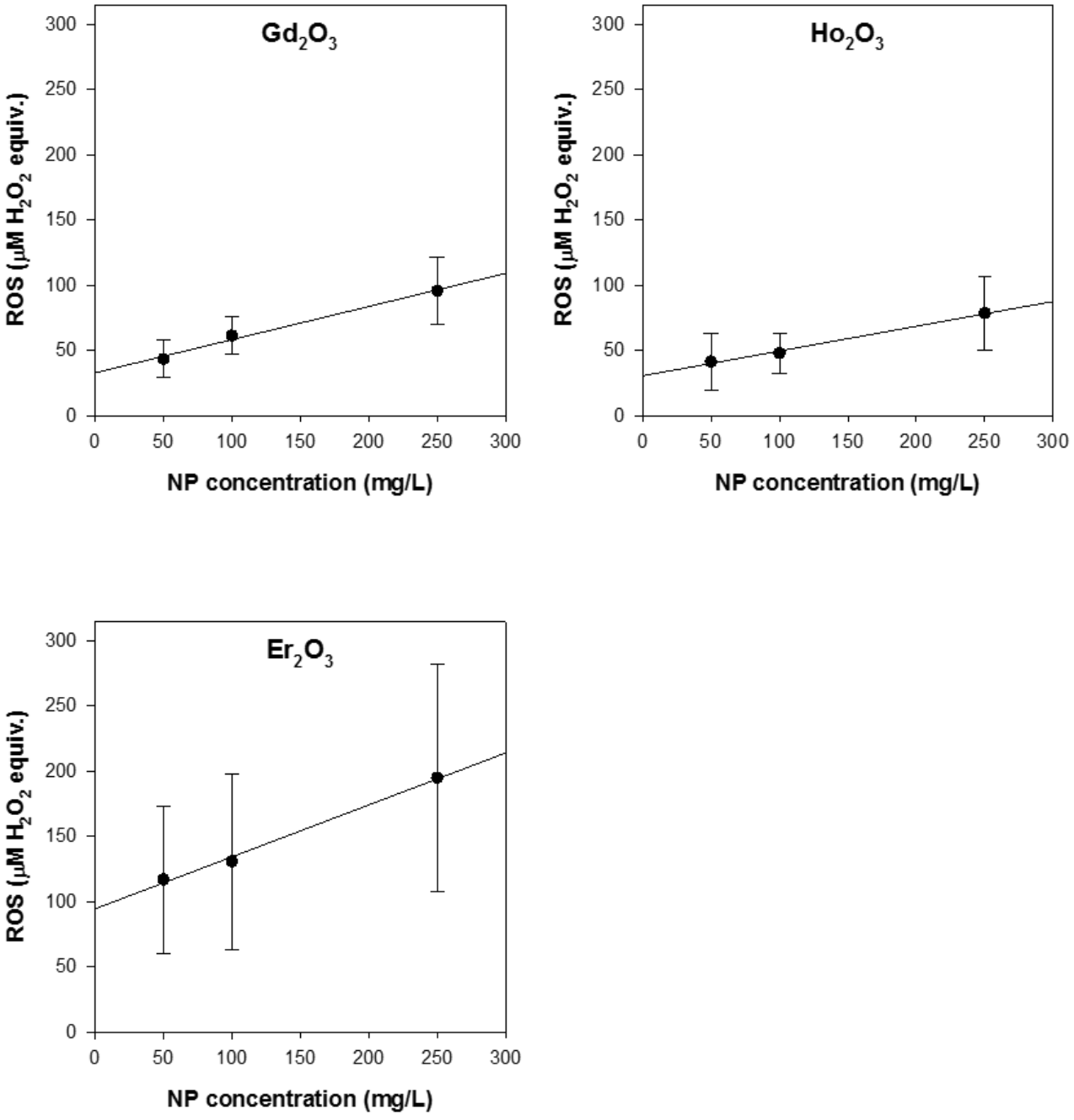


FIGURE C.2: Reactive oxygen species (ROS), reported in units of $\mu$M $H_2O_2$ equivalent, generated by 50, 100, and 250 mg/L LnOx NPs. Error bars represent standard error (n=3).

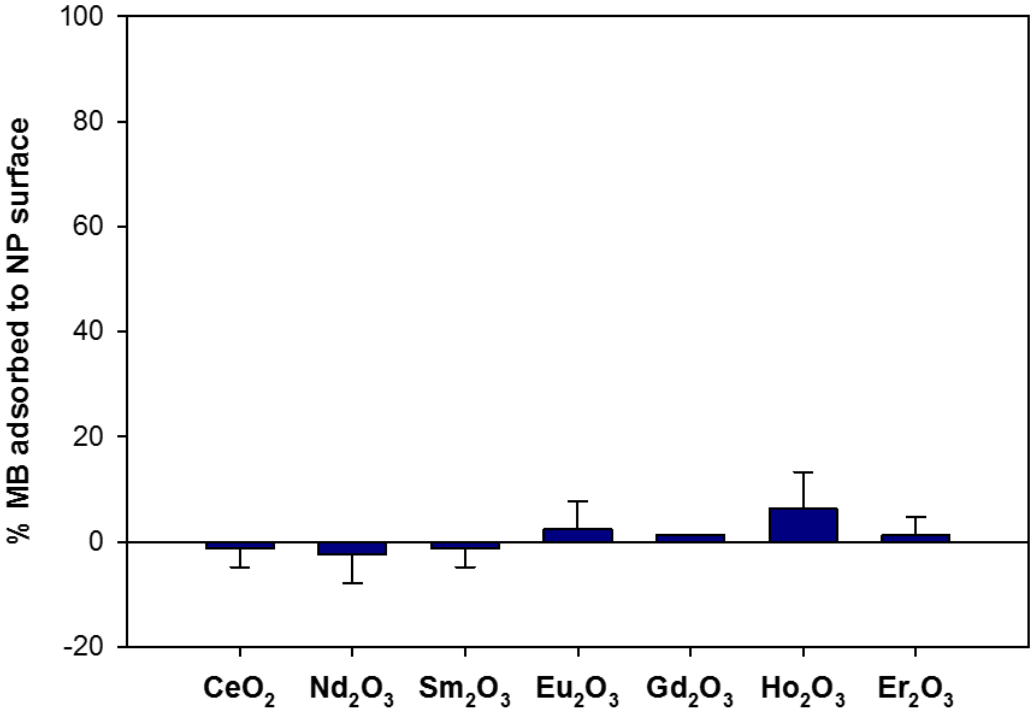


FIGURE C.3: Percent methylene blue (concentration = 0.04 mM) adsorbed to the surface of 250 mg/L LnOx NPs. Error bars represent standard error.